

Loughborough University Institutional Repository

Determining the shape of a liquid droplet: from microscopic theory to coarse grained models

This item was submitted to Loughborough University's Institutional Repository by the/an author.

Additional Information:

- A Doctoral Thesis. Submitted in partial fulfilment of the requirements for the award of Doctor of Philosophy of Loughborough University.

Metadata Record: <https://dspace.lboro.ac.uk/2134/19985>

Publisher: © Adam Hughes

Rights: This work is made available according to the conditions of the Creative Commons Attribution-NonCommercial-NoDerivatives 4.0 International (CC BY-NC-ND 4.0) licence. Full details of this licence are available at: <https://creativecommons.org/licenses/by-nc-nd/4.0/>

Please cite the published version.

Determining the Shape of a Liquid Droplet: From Microscopic Theory to Coarse Grained Models

Adam Hughes

Submitted in partial fulfilment of the requirements for the award of
Doctor of Philosophy of Loughborough University

September 2015

©Adam Hughes 2015

Certificate of Originality

This is to certify that I am responsible for the work submitted in this thesis, that the original work is my own except as specified in acknowledgements or in footnotes, and that neither the thesis nor the original work contained therein has been submitted to this or any other institution for a degree.

Abstract

This thesis investigates the wetting of simple liquids using two density functional theory (DFT) models. The first model is a discrete lattice-gas model and the second a continuum DFT model of a hard-sphere reference system with an additional attractive perturbation. The wetting properties of liquids are principally investigated by studying the binding, or interface, potential of the fluid and this thesis presents a method by which a binding potential can be fully calculated from the microscopic DFT.

The binding potentials are used to investigate the behaviour of the model fluid depending on the range to which particle interactions are truncated. Long ranged particle interactions are commonly truncated to increase computational efficiency but the work in this thesis shows that in making this truncation some important aspects of the interfacial phase behaviour are changed. It is demonstrated that in some instances by reducing the interaction range of fluid particles a shift in phase behaviour from wetting to non wetting occurs.

The binding potential is an input to larger scale coarse grained models and this is traditionally given as an asymptotic approximation of the binding potential. By using the full binding potential, calculated from the DFT model, as an input, excellent agreement can be found between the results from the microscopic DFT model and the larger scale models. This is first verified with the discrete lattice-gas model where the discrete nature of the model causes some non-physical behaviour in the binding potentials. The continuum DFT model is then applied which corrects this behaviour.

An adaptation to this continuum model is used to study short ranged systems at high liquid densities at state points below the ‘Fisher-Widom’ line. The form of the decay of the density profiles and binding potentials now switches from monotonic to oscillatory. This model leads to highly structured liquid droplets exhibiting a step-like structure.

For Gemma

Acknowledgements

I would like to thank Andrew Archer for his supervision throughout my PhD, I have only made it this far thanks to his support. Andy is always happy to help and his enthusiasm for the subject has been a constant source of motivation for me throughout. I also would like to thank Uwe Thiele for his supervision, his input is always insightful and helps me to see problems from a different angle.

I have spent a lot of time in the office over the past three years and I need to thank all my colleagues for making it such an enjoyable experience.

Finally I would like to thank my family, my mum and dad for all their support and encouragement over the years, and Gemma, my wife, for making every day that little bit better.

Contents

1	Introduction	1
1.1	Mesoscopic Modelling Techniques	3
1.2	Microscopic Interactions	5
2	Background Information	7
2.1	Density Functional Theory	7
2.1.1	Thermodynamics and Statistical Mechanics	7
2.1.2	A Functional of the Grand Free Energy	11
2.2	Approximations of the Free Energy	15
2.3	Fundamental Measure Theory	17
2.3.1	Reduced Dimensions	20
2.4	Liquid-Gas Coexistence and Wetting	21
2.5	Surface Tension	25
2.6	The Binding Potential	27
3	A Discrete DFT Model	33
3.1	The Lattice Gas Model	33
3.1.1	A Derivation via the Gibbs-Bogoliubov Inequality	36
3.1.2	Defining the Potentials	40
3.1.3	The Model in Lower Dimensions	41
3.1.4	Bulk Fluid Phase Diagram	42
3.2	Solutions to the Model	44
3.3	Adsorption Isotherms	45
3.4	Calculating the Binding Potential	50
3.4.1	The Sharp-Kink Approximation	51
3.4.2	Fixing the Adsorption	54
3.4.3	The Range of Pair Interactions	58
3.5	Liquid Droplets and the Interface Hamiltonian Model	59
3.6	Conclusions	63

4 A Continuum DFT Model	66
4.1 The DFT Model	66
4.1.1 Density Profiles and Adsorption Constraints	70
4.1.2 Binding Potentials	72
4.2 A Model Fluid with Oscillatory Binding Potentials	85
4.2.1 Density Profiles with Oscillations at the Liquid-Gas Interface . . .	87
4.2.2 Oscillatory Binding Potentials and Highly Structured Droplets . .	87
4.3 Conclusions	92
5 Final Remarks	94
A A Simpler Lattice Pair Interaction	97
B Parameters for the binding potential fit functions	99

List of Figures

1.1	Charcterisation of wetting from the contact angle	3
1.2	Droplet profile from IH model	6
2.1	Hard-sphere density profiles	20
2.2	Phase diagram of a fluid	23
2.3	Adsorption isotherms	26
2.4	liquid-gas interface	28
2.5	Schematic of the system	29
2.6	Binding potentials	31
2.7	Binding potential off coexistence	32
3.1	Discretisation of a fluid	34
3.2	Reduction of model dimensionality	41
3.3	Phase diagram of the lattice fluid	44
3.4	Adsorption isotherms	47
3.5	Adsorption curves from continuation techniques	48
3.6	Energetics of the pre-wetting line	49
3.7	LG model binding potentials	52
3.8	Deformation of the lattice interface	53
3.9	Sharp-kink binding potential	55
3.10	Discrete stabilising fictitious potentials	57
3.11	Interaction ranges - decay rate	59
3.12	Interaction ranges - phase shift	60
3.13	Discrete 2D density profiles	61
3.14	Comparison of droplet profiles	62
3.15	Comparison of contact angles	64
4.1	Phase diagram of LJ fluid	69
4.2	Continuum 1D density profiles	71
4.3	Stabilising fictitious potentials	73
4.4	Continuum 2D density profiles	74
4.5	Continuum binding potentials	76

4.6	Change in minimum value of the binding potential	77
4.7	Effect of truncating interaction ranges	78
4.8	Accuracy of fit function	80
4.9	Comparison for different dimensionality	81
4.10	Comparison of droplet profiles	82
4.11	Alternative film height profiles	83
4.12	Comparison of contact angles	84
4.13	Increasing droplet size	85
4.14	AO potential	86
4.15	Oscillatory density profiles	88
4.16	Onset of oscillations in the binding potentials	88
4.17	Oscillatory binding potentials	89
4.18	Film height profiles from oscillatory binding potentials	91
4.19	Highly structured droplet density profiles	92
A.1	Nearest and next nearest neighbours	97
A.2	Dimensional reduction	98

Chapter 1

Introduction

Wetting is a very important process both biologically and industrially with a huge field of application. As an example, consider how water behaves when it is in contact with the leaf of the lotus plant. The water is repelled by the leaf and forms spheres, it does not ‘wet’ the leaf. This is beneficial for the plant as the water easily rolls off the leaves, collecting small bits of debris as it goes and so helps the leaf to remain clean, improving its ability to photosynthesise. When thinking of lubrication however, this would be a very undesirable property. A lubricating oil must wet the surface, maintaining a constant film to ensure good lubrication.

On macroscopic length scales, wetting manifests itself in how a droplet of liquid behaves in contact with a substrate [1, 2]. The substrate is usually a solid boundary but the following discussion could also apply to a liquid in contact with a different, immiscible liquid, water and oil, say. When a liquid droplet is placed on a substrate, the edge of the droplet meets the substrate at a specific angle θ as shown in Fig. 1.1. This contact angle measures the degree to which a liquid wets the substrate. Three different wetting regimes are identified for a liquid droplet surrounded by a gas which are shown in Fig. 1.1. These are described as complete wetting for $\theta = 0^\circ$, partial wetting for $0^\circ < \theta < 180^\circ$ and non-wetting for $\theta = 180^\circ$. Only the case of partial wetting has the traditional droplet shape (Fig. 1.1a). The complete wetting ‘droplet’ is really a liquid film and the non-wetting case is a perfect sphere. The observed wetting behaviour is driven by the thermodynamic principle that a system will evolve towards a state of least free energy. For the system as shown in Fig. 1.1, there are three interfaces present, each coloured differently in the figure, a liquid-gas (blue), wall-liquid (red) and wall-gas (green) interface and for every interface there is an associated surface tension which has the dimensions of energy per unit area. For these three interfaces, the associated surface tensions are denoted γ_{lg} , γ_{wl} and γ_{wg} for the liquid-gas, wall-liquid and wall-gas interfaces respectively. Naively, one could then consider that for such a system of a fixed volume of liquid on a substrate, that it is only the relative areas of the interfaces and the magnitude of their surface tensions which determine the free energy of the system.

The surface tension is the energetic cost of increasing the area of an interface by one unit and arises as follows [3]: Attractive bonds between fluid particles serve to lower the free energy of the system. A fluid particle in the bulk of the liquid has more neighbouring fluid particles to form a bond with than a similar fluid particle positioned at the interface. This interfacial particle can not form as many bonds with other particles which raises the free energy and so a liquid-gas interface has a positive surface tension as it raises the free energy of the system. A liquid-gas interface must have a positive surface tension, otherwise, complete mixing would occur to maximise the interfacial area between the two fluids which would lower the energy. For a solid and a liquid, where the solid can not be deformed, this is not the case and the interface between them could have either a positive or negative surface tension. The particles in a solid are often packed together more densely than in a liquid and so an interface formed between a solid and a liquid can result in more attractive bonds than for the liquid phase alone. This leads to a lower free energy meaning that in this case the wall-liquid interface has a negative surface tension.

If a system is made up of only a suspended liquid droplet then this liquid must form a sphere as this minimises the surface area of the interface for a fixed volume of liquid, resulting in the least possible total energy of the system. If this liquid droplet is brought into contact with a substrate then it is no longer sufficient to simply minimise the liquid-gas interfacial area to minimise the free energy of the system. The areas of the wall-liquid and wall-gas interfaces must also be optimised in order to find the configuration of lowest energy. The droplet, while not forming a complete sphere will still hold the shape of a spherical cap (as in Fig. 1.1a) as this is the most efficient shape to reduce the liquid-gas interfacial area for a fixed area of the wall-liquid interface. A droplet with a contact angle of $\theta = 90^\circ$ will be a half-sphere which gives the least liquid-gas interfacial area for a fixed volume of liquid on a substrate. This ignores the case of $\theta = 0^\circ$ when the liquid forms a film over the substrate rather than a droplet. If the droplet begins to spread out over the surface then the contact angle decreases, the wall-liquid interfacial area increases and so does the liquid-gas interfacial area. If the drop contracts from the half-sphere then the contact angle increases above $\theta = 90^\circ$, the wall-liquid area then decreases leading to a corresponding increase in the wall-gas area, the liquid-gas area must also increase. This trade off between the different interfacial areas and their relation to the contact angle is encapsulated in Young's equation:

$$\cos(\theta) = \frac{\gamma_{wg} - \gamma_{wl}}{\gamma_{lg}}. \quad (1.1)$$

Complete wetting is characterised by a contact angle of $\theta = 0^\circ$, inserting this into Young's equation leads to $\gamma_{wg} = \gamma_{lg} + \gamma_{wl}$, if the liquid does not completely wet the substrate then $\theta > 0^\circ$ and from Young's equation $\gamma_{wg} < \gamma_{lg} + \gamma_{wl}$. From this it is given that wetting only occurs if the wall-liquid and liquid-gas surface tensions are equal to or less than the the surface tension for the wall-gas interface. Physically, this means that

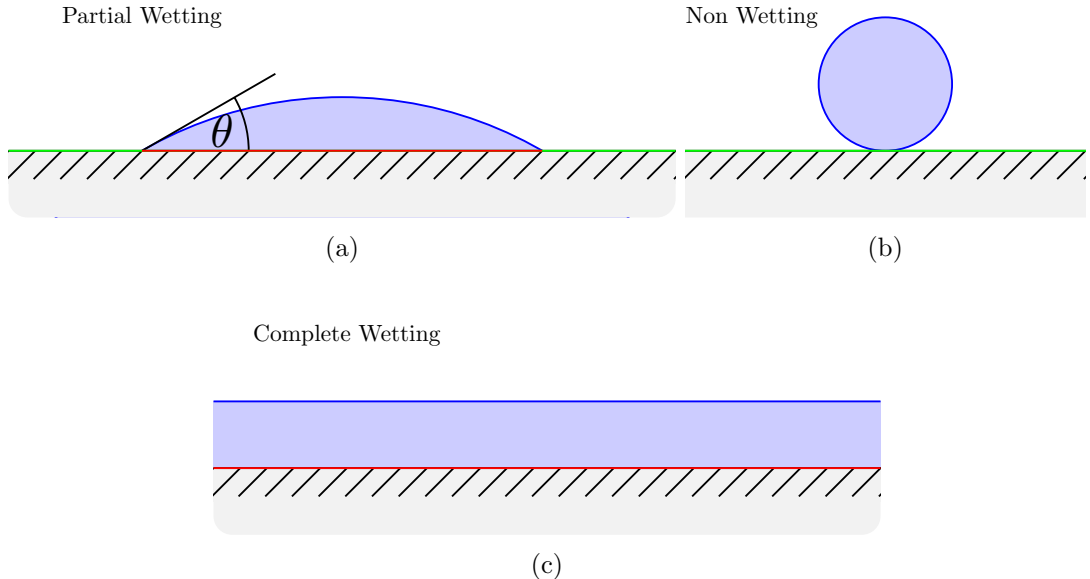


Figure 1.1: Different characterisations of the wetting of a liquid droplet on a solid substrate. The degree to which the liquid wets the solid can be measured by a contact angle θ that the droplet makes with the substrate. Complete wetting is characterised by $\theta = 0^\circ$, completely non-wetting by $\theta = 180^\circ$ and intermediary states are characterised as partially wetting for $0^\circ < \theta < 180^\circ$. A non-wetting droplet of $\theta = 180^\circ$ is a perfect sphere, more wetting droplets are spherical caps to minimise the liquid-gas interface as much as possible. There are three different interfaces each coloured differently, liquid-gas (blue), wall-liquid (red) and wall-gas (green).

wetting will occur if it is energetically favourable to replace the single wall-gas interface with the wall-liquid and liquid-gas interfaces.

1.1 Mesoscopic Modelling Techniques

The above arguments are valid in the mesoscopic regime, when liquid droplets are small enough that gravity can be neglected. For such small droplets, a popular model for calculating the shape of a droplet is the interface Hamiltonian (IH) model [4, 5]. The free energy of a liquid film is expressed as a function of the local film height above a solid interface:

$$F[h(\mathbf{x})] = \int \left[g(h) + \gamma_{lg} \sqrt{1 + (\nabla h)^2} \right] d\mathbf{x}, \quad (1.2)$$

where h is the thickness of the liquid film above a position \mathbf{x} on the interface. Finding the function h which minimises this free energy gives the equilibrium film height profile. A typical droplet profile found via a minimisation of Eq. (1.2) is displayed in Fig. 1.2. The function g in the above functional is called the binding, or interface, potential [4, 5, 6, 7] and is related to the disjoining pressure, $\Pi = -\partial g/\partial h$ [8, 9]. The binding potential

arises from an effective interaction between two interfaces.

This interaction is the result of interactions between fluid particles and can be seen as arising in a similar manner to the surface tension. The surface tension is the additional energy that arises due to a particle interacting with another particle across an interface. If this particle also has a pairwise interaction with a third particle across a different interface then the total energetic change is not simply the sum of the two separate surface tensions. The binding potential measures this change beyond that of the sum of the two surface tensions, this idea is made clearer in Chapter 2 when the binding potential is properly defined. The binding potential is often approximated by a simple form, typically some asymptotic expansion depending on the specific fluid under consideration. The exact form is determined by the range of the particle interactions within the liquid and solid. If all interactions are short ranged then the binding potential will have an asymptotic expansion of the form [4]

$$g(h) = a \exp(-h/\xi) + b \exp(-2h/\xi) + \dots, \quad (1.3)$$

where ξ is the bulk correlation length. In this case the binding potential quickly decays to zero since a particle does not have to be well separated from an interface to not interact with it. If there are long ranged (dispersion) interactions the asymptotic form will be

$$g(h) = \frac{a}{h^2} + \frac{b}{h^3} + \dots. \quad (1.4)$$

The decay rate is now much slower as particles can still ‘feel’ an interface even when well separated from it. It will also be shown later how the form of Eq. (1.4) arises based on the nature of the particle interactions. Combinations of these two forms are also possible.

A particularly important aspect of the IH model is its application in the thin film equation where the dynamics of thin liquid films may be studied. Under the long wavelength approximation [10], where surface gradients and contact angles must be small the gradient term in Eq. (1.2) can be approximated $\sqrt{1 + (\nabla h)^2} \approx 1 + (\nabla h)^2/2$ and then the free energy functional reduces to

$$F[h] = \int \left[g(h) + \frac{\gamma_l g}{2} (\nabla h)^2 \right] d\mathbf{x}, \quad (1.5)$$

where a constant term is omitted. This is now in a suitable form that can be used in the thin film evolution equation [10, 11], which, in gradient dynamics form, is given by [12]

$$\frac{\partial h}{\partial t} = \nabla \cdot \left[Q(h) \nabla \frac{\delta F[h]}{\delta h} \right], \quad (1.6)$$

where $Q(h)$ is a mobility factor depending on h and $\delta F/\delta h$ is the functional derivative of the free energy with respect to the film height profile.

1.2 Microscopic Interactions

For mesoscopic size liquid droplets and films, an asymptotic form of the binding potential is usually adequate. However, the small h behaviour of the binding potential is not accurately described. As such this reduces the range of applicability of fluids modelled in this way, for example, the IH model, with the asymptotic result of Eq. (1.4), truncated after a few terms, used as input will not accurately describe droplets at sizes approaching the microscopic regime. This thesis aims to address this problem by making a full calculation of the binding potential to improve on the asymptotic results. The binding potential connects the microscopic and mesoscopic length scales, it represents all of the atomistic interactions between fluid particles, taking place on a scale of Angstroms, as a single effective potential with a range up to hundreds of nanometres. Any calculation of the binding potential should be made on the basis of these microscopic interactions.

The forces between atoms and molecules arise in a number of different ways including; dipole-dipole, dipole-induced dipole and dispersion forces [13]. The first two mechanisms, also known as Keesom and Debye forces, only occur with polarised particles, dispersion forces occur between all particles. The random fluctuations of electron clouds can temporarily induce a dipole in a particle, these induced dipoles can then interact with other particles, inducing dipoles and attracting them. These dispersion forces are non-additive but the effect of this non-additivity is much stronger in solids and can often be ignored in liquids. Fluid particles can also repel each other. This could occur as a result of polarised particles at longer ranges or, more usually, there is a short ranged repulsive force from overlapping electron clouds of the particles. The Lennard-Jones potential [13, 14, 15] is often used to model these van der Waals forces and fits well with experimental measurements [13, 15]. The binding potential coarse grains all of these microscopic effects into a single potential.

This thesis presents a method by which the binding potential can be calculated from a starting point based on these microscopic particle interactions. This idea has previously been applied using numerical simulations[6, 16] where, for example, Tretyakov *et al.* [17] describe a method of parameter passing based on molecular dynamics simulations to match up between the microscopic and mesoscopic regimes. In this thesis, a density functional theory (DFT) based method of calculating the binding potential is presented. With this method, the binding potential can be calculated fully, including in the small h regime. The method will be verified by calculating the shape of liquid droplets using only the DFT model and comparing these results with droplets found by using the binding potential, calculated from the same DFT model, as an input to the IH model.

This thesis is arranged as follows: Chapter 2 outlines some necessary background material for the study of fluids on a microscopic scale. From a starting point of statistical mechanics and thermodynamics a general overview of DFT is presented. Chapter 3 is based on the publications [18] and [19] and describes a discrete DFT, the lattice-gas (LG)

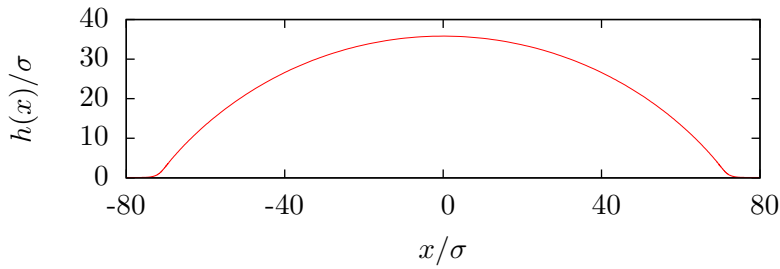


Figure 1.2: A droplet profile found via the IH model, Eq. (1.2). The droplet is a spherical cap with a very thin precursor film present.

model, and uses it to outline a method by which the binding potential may be calculated. In chapter 4, based on [20], a continuum DFT model is used to reproduce many of the results found with the LG model, this then goes further to investigate conditions for when oscillatory binding potentials occur.

Chapter 2

Background Information

This chapter sets out the necessary background information that is required to formulate a general density functional theory (DFT) model. This proceeds so far as to introduce fundamental measure theory (FMT) which gives a good approximation for hard-sphere systems and provides a starting point for the model introduced in chapter 4. Several other important concepts such as the binding potential are also discussed.

2.1 Density Functional Theory

DFT gives a theoretical framework within which macroscopic thermodynamic quantities of a fluid, such as the Helmholtz free energy [14, 21], can be calculated, taking as input the potentials for how the particles interact with each other. DFT is particularly suited to describing inhomogeneous fluids such as at interfaces or within some confining geometry. The thermodynamic quantities are given as functionals of a microscopic density profile. One considers a fluid of particles of a particular bulk density. A gas is a very low density fluid and a liquid is a higher density one. Crystals, which are not considered here, have an even higher average density but while, in the absence of an external field, liquids and gases have a uniform density, crystals do not and exhibit long ranged order. The ‘particles’ of the fluid could be the atoms or molecules that make up a fluid or even colloids in a suspension, in the latter case one then considers colloidal gases or liquids immersed in a liquid solvent. The interface between two phases is not sharp on the microscopic scale. There is a smooth transition from one phase of a particular fluid density to the other. The next sections give a general overview, starting from statistical mechanics, of how this formalism arises. The section draws on the presentations of DFT given in Refs. [14], [22] and [23].

2.1.1 Thermodynamics and Statistical Mechanics

Consider a fluid system made up of N identical, spherical particles of mass m where each particle can be described by three dimensional (3D) position and momenta variables,

$\mathbf{r} = (r_x, r_y, r_z)$ and $\mathbf{p} = (p_x, p_y, p_z)$ respectively. The Hamiltonian of such a system is a function of the $6N$ variables of positions $\mathbf{r}^N = \{\mathbf{r}_1, \dots, \mathbf{r}_N\}$, and momenta, $\mathbf{p}^N = \{\mathbf{p}_1, \dots, \mathbf{p}_N\}$ of the particles given by

$$\mathcal{H} = K(\mathbf{p}^N) + \Phi(\mathbf{r}^N) + \hat{V}(\mathbf{r}^N), \quad (2.1)$$

where

$$K(\mathbf{p}^N) = \sum_{i=1}^N \frac{|\mathbf{p}_i|^2}{2m}, \quad (2.2)$$

is the kinetic energy contribution, $\Phi(\mathbf{r}^N)$ is the potential energy contribution arising from inter-particle interactions and $\hat{V}(\mathbf{r}^N)$ is the energy arising from an external field. Each particle is assumed to couple independently with the external field so the energetic contribution may be expressed as

$$\hat{V}(\mathbf{r}^N) = \sum_{i=1}^N V(\mathbf{r}_i), \quad (2.3)$$

where $V(\mathbf{r})$ is the external potential felt by a particle at position \mathbf{r} . The motion of all of these fluid particles could be tracked by solving the set of $3N$ coupled Newton's equations of motion subject to $6N$ initial conditions. Computationally, this is an impossible undertaking as, for example, a cubic centimetre of water contains approximately 3×10^{22} water molecules. This is also unnecessarily detailed since, while the motion of individual fluid particles is highly fluctuating and chaotic, average quantities are very stable [21]. It is from these average quantities that the macroscopic thermodynamic variables arise, i.e. the internal energy of the fluid is the average of the Hamiltonian

$$U = \langle \mathcal{H} \rangle. \quad (2.4)$$

Rather than finding a time average, it is often easier to calculate ensemble averages.

A statistical ensemble is a collection of identically prepared systems each giving a 'snapshot' of the fluid. Averaging over all of these snapshots gives the ensemble average. The first law of thermodynamics states that the internal energy of a fluid can only change as a result of heat being added to the system, work being done on the system or particles being added to the system. The first law can be expressed as

$$dU = TdS - pdV + \mu dN, \quad (2.5)$$

where T , S , p , V , μ are the temperature, entropy, pressure, volume and chemical potential respectively. These variables appear in three conjugate pairs, each pair containing one intrinsic variable, such as the temperature, which does not increase with the system size, and one extrinsic variable, such as the entropy, which does change with the system

size. The change in the internal energy is then governed by the changes in the extrinsic variables of entropy, volume and particle number. An assumption is made here that the system is quasi-static [21], without this assumption definitions of temperature, pressure and chemical potential don't make sense. Of the seven variables given in Eq. (2.5), three are held constant to define a particular ensemble. If T , V and N are held constant then this defines the canonical ensemble. This should be considered as a non-insulated, closed system where its temperature is fixed by some, much larger, external reservoir. It can not exchange particles with its surroundings. Later the grand canonical ensemble will be discussed, this is similar to the canonical ensemble but the system is no longer constrained to have a fixed number of particles (e.g. the container has porous walls) and instead the chemical potential is fixed by the external reservoir. As the system size is increased, the thermodynamic limit [24] is approached where all ensembles become equivalent. With this in mind, whichever ensemble makes the problem the most tractable should be chosen.

In the canonical ensemble, the ensemble average of a quantity $x = x(\mathbf{r}^N, \mathbf{p}^N)$ is defined as

$$\langle x \rangle = \iint x(\mathbf{r}^N, \mathbf{p}^N) f(\mathbf{r}^N, \mathbf{p}^N) d\mathbf{r} d\mathbf{p}, \quad (2.6)$$

where f is a probability density function normalised such that

$$\iint f(\mathbf{r}^N, \mathbf{p}^N) d\mathbf{r} d\mathbf{p} = 1, \quad (2.7)$$

and $d\mathbf{r} d\mathbf{p}$ refers to the coordinates of all of the particles. For this particular ensemble the probability density function is given by

$$f(\mathbf{r}^N, \mathbf{p}^N) = \frac{1}{h^{3N} N!} \frac{\exp(-\beta \mathcal{H})}{Q_N}, \quad (2.8)$$

where h is Planck's constant, $\beta = 1/k_B T$, with k_B being Boltzmann's constant, and the normalisation factor Q_N is an important quantity known as the partition function and is defined as

$$Q_N = \frac{1}{h^{3N} N!} \iint \exp(-\beta \mathcal{H}) d\mathbf{r} d\mathbf{p}. \quad (2.9)$$

The probability that the system is in a particular state is proportional to $\exp(-\beta \mathcal{H})$, see Eq. (2.8). The partition function Q_N is used to normalise the probability density function and the $h^{3N} N!$ term in both the partition function and the probability density function ensure that they are dimensionless and also correspond with the equivalent results from quantum statistical mechanics. Since the particle momenta only occur in the Hamiltonian in the kinetic energy term, the partition function can be simplified by (analytically) performing the momenta integrals. This integration leads to [14]

$$Q_N = \frac{Z_N}{N! \Lambda^{3N}} = \frac{1}{N! \Lambda^{3N}} \int \exp(-\beta(\Phi(\mathbf{r}^N) + \hat{V}(\mathbf{r}^N))) d\mathbf{r}, \quad (2.10)$$

where $\Lambda = \sqrt{\beta h^2/2m\pi}$ is the thermal de-Broglie wavelength [14]. When working with a particular ensemble it is often useful to define a particular free energy, the energy of the system which is available to perform work [25]. For example, when stretching a spring not all of the energy expended is stored as a restoring potential, some is lost through friction, etc, the increase in the free energy of stretching the spring is that energy which is then available to restore the spring. Since N and V are fixed in the canonical ensemble then the first law of thermodynamics, Eq. (2.5), can rearranged to give

$$dU - TdS = dF = 0, \quad (2.11)$$

where the Helmholtz free energy has been defined

$$F = U - TS, \quad (2.12)$$

and is the appropriate free energy to work with in the canonical ensemble. Note that $dF = 0$ in Eq. (2.11) because Eq. (2.5) was made under the assumption that the system should be at equilibrium. The second law of thermodynamics states that

$$dS \geq 0, \quad (2.13)$$

i.e. globally, entropy increases over time. From the second law it follows that for canonical ensemble system out of equilibrium, $dF \leq 0$. To restate this: the Helmholtz free energy of a system decreases as it approaches equilibrium and is at a minimum when equilibrium is reached. This important result underpins much of the work presented here and it is this necessity to evolve towards a state of least free energy that drives the behaviour of liquid droplets discussed in the previous chapter and illustrated in Fig. 1.1.

The importance of the partition function is the link it provides between the microscopic properties of the system to the macroscopic thermodynamic quantities. If the partition function is known, then all macroscopic variables can be calculated [25]. In particular, in the canonical ensemble the free energy is given

$$F = -k_B T \ln(Q_N). \quad (2.14)$$

The derivation of this link is as follows [21]: Revisiting Eq. (2.4), the internal energy is

given

$$\begin{aligned}
U = \langle \mathcal{H} \rangle &= \frac{1}{h^{3N} N! Q_N} \iint \mathcal{H}_N \exp(-\beta \mathcal{H}_N) d\mathbf{r} d\mathbf{p}, \\
&= -\frac{1}{Q_N} \frac{\partial}{\partial \beta} \frac{1}{h^{3N} N!} \iint \exp(-\beta \mathcal{H}_N) d\mathbf{r} d\mathbf{p}, \\
&= -\frac{1}{Q_N} \frac{\partial Q_N}{\partial \beta} = -\frac{\partial}{\partial \beta} \ln(Q_N), \\
&= k_B T^2 \frac{\partial}{\partial T} \ln(Q_N).
\end{aligned} \tag{2.15}$$

The entropy can be found as a derivative of the Helmholtz free energy

$$S = - \left(\frac{\partial F}{\partial T} \right)_{V,N}, \tag{2.16}$$

which, when inserted into Eq. (2.12), gives the differential equation

$$F - T \frac{\partial F}{\partial T} = U. \tag{2.17}$$

Using the result found in Eq. (2.15) this differential equation has the solution

$$F = -k_B T \ln(Q_N), \tag{2.18}$$

where a term linear in T is set to zero to satisfy the demand that entropy is zero at $T = 0$.

2.1.2 A Functional of the Grand Free Energy

Suppose now that the condition of a fixed number of particles in the canonical ensemble is relaxed and particles are free to enter and leave the system. The number of particles in the system is now dependent on the chemical potential which is determined by the coupling of the system to a large external reservoir of particles. The condition of fixed μ , V and T defines the grand canonical ensemble. The grand canonical ensemble could be visualised as a small subsystem of the canonical ensemble, where everything outside of this sub-system now makes up a reservoir. This reservoir is sufficiently large that it fixes the chemical potential and the temperature of the subsystem. With the particle number free to fluctuate, but with fixed volume, the first law can be expressed as

$$dU - TdS - \mu dN = dF - \mu dN = d\Omega = 0, \tag{2.19}$$

where the grand free energy is defined

$$\Omega = F - \mu N. \tag{2.20}$$

The grand free energy, Ω , is the appropriate free energy to consider in the grand canonical ensemble. It is a Legendre transform of the Helmholtz free energy and as equilibrium is approached the grand free energy decreases and reaches a minimum at equilibrium, the partition function of this ensemble is defined

$$\Xi = \sum_{N=0}^{\infty} \frac{1}{h^{3N} N!} \iint \exp -\beta(\mathcal{H} - \mu N) d\mathbf{r} d\mathbf{p}. \quad (2.21)$$

The classical trace is defined

$$\text{Tr } x = \sum_{N=0}^{\infty} \frac{1}{h^{3N} N!} \iint x d\mathbf{r} d\mathbf{p}, \quad (2.22)$$

and so the grand canonical partition function can be expressed as $\Xi = \text{Tr } \exp(-\beta(\mathcal{H} - \mu N))$. The partition function now not only integrates over all positions and momenta of the particles but also sums over all the possible numbers of particles in the system. There are close links between the canonical and grand canonical ensembles and the partition functions can be related by

$$\Xi = \sum_{N=0}^{\infty} e^{\beta \mu N} Q_N. \quad (2.23)$$

One should also expect that the partition function Ξ can be related to the grand free energy in a similar fashion to Eq. (2.18), this indeed the case and the grand free energy is given

$$\Omega = -k_B T \ln(\Xi). \quad (2.24)$$

This result can be found in several ways. One such way is to consider the grand canonical ensemble as the system size increases and it approaches the thermodynamic limit. As this limit is approached the fluctuations about the average particle number decrease to zero [24] and so the grand partition function can be written

$$\Xi \approx e^{\beta \mu \langle N \rangle} Q_{\langle N \rangle}. \quad (2.25)$$

Taking the logarithm of this partition function gives

$$-k_B T \ln(\Xi) = -k_B T \ln(Q_{\langle N \rangle}) - k_B T \ln(e^{\beta \mu \langle N \rangle}) = F - \mu N = \Omega, \quad (2.26)$$

which links the grand partition function to the grand free energy. This is perhaps the simplest way to arrive at this result but it can also be found without taking the thermodynamic limit [25].

In order to calculate averages in this ensemble a probability density function is defined

$$f_0(\mathbf{r}^N, \mathbf{p}^N) = \frac{\exp(-\beta(\mathcal{H} - \mu N))}{\Xi}, \quad (2.27)$$

where f_0 has been given the subscript to make explicit that it is an equilibrium probability density function. A probability density function is an equilibrium one if it does not change in time and is a function of the Hamiltonian \mathcal{H} , the probability density in Eq. (2.8) also satisfies this criteria. The ensemble average of a quantity in the grand canonical ensemble is then defined

$$\langle x \rangle = \text{Tr } xf_0(\mathbf{r}^N, \mathbf{p}^N). \quad (2.28)$$

The purpose of this present section is to establish the grand free energy as a functional of the density profile and to this end the one body particle density is defined

$$\rho(\mathbf{r}) = \langle \hat{\rho}(\mathbf{r}) \rangle, \quad (2.29)$$

where $\hat{\rho}(\mathbf{r}) = \sum_{i=1}^N \delta(\mathbf{r} - \mathbf{r}_i)$ is the density operator. The density operator is also used to rewrite Eq. (2.3) as

$$\hat{V}(\mathbf{r}^N) = \int \hat{\rho}(\mathbf{r}) V(\mathbf{r}) \, d\mathbf{r}, \quad (2.30)$$

where the form of $V(\mathbf{r})$ remains to be specified. It is worth pointing out here that for a fixed interatomic potential $\Phi(\mathbf{r}^N)$, the particular choice of external field $V(\mathbf{r})$ specifies the Hamiltonian, Eq. (2.1), and therefore defines the probability density function. As such, the probability density function, which is a function of the particle positions and momenta, is also a functional of the external field.

The above is all that is required to find the grand free energy as a functional of the density profile. First, with no particular justification for the particular form, the grand free energy is defined as a functional of a probability density function

$$\Omega[f] = \text{Tr } [f(\mathcal{H} - \mu N + k_B T \ln f)]. \quad (2.31)$$

The probability density function f here, is not necessarily an equilibrium one, but does satisfy the normalisation condition $\text{Tr } f = 1$. If the equilibrium probability density, Eq. (2.27), is inserted into this functional then

$$\Omega[f_0] = -k_B T \ln(\Xi) = \Omega, \quad (2.32)$$

which verifies that this functional returns exactly the grand potential of the system for the equilibrium probability density. One can then prove [22] that for any f such that $\text{Tr } f = 1$,

$$\Omega[f] > \Omega[f_0] = \Omega, \quad (2.33)$$

i.e. that the grand free energy for a non-equilibrium state with distribution f has a higher value of $\Omega[f]$ than the equilibrium state. As the system evolves towards equilibrium $\Omega[f]$

decreases towards to the equilibrium value, Ω , which is the minimum. Secondly, it can also be proved that the density profile $\rho(\mathbf{r})$ is uniquely defined by the choice of external field [22]. This equivalently shows that a particular choice of $\rho(\mathbf{r})$ fixes an external field $V(\mathbf{r})$ which in turn defines the equilibrium probability density function f_0 . It then follows from Eq. (2.33) that

$$\Omega[\rho(\mathbf{r})] > \Omega[\rho_0(\mathbf{r})] = \Omega, \quad (2.34)$$

where ρ_0 is the equilibrium density profile. The results from Eqs. (2.31) to (2.34) form the basis of DFT. They show that the grand free energy can be expressed as a functional of the density profile and moreover, that the functional is minimised at equilibrium to give exactly the grand free energy. The density profile which minimises this functional is the unique equilibrium density profile.

From the definition of the grand potential functional in Eq. (2.31), expanding the Hamiltonian into its separate parts, the grand free energy can be rewritten as

$$\Omega[\rho(\mathbf{r})] = F[\rho(\mathbf{r})] + \int \rho(\mathbf{r}) (V(\mathbf{r}) - \mu) \, d\mathbf{r}, \quad (2.35)$$

where

$$F[\rho(\mathbf{r})] = \text{Tr} [f(K + \Phi + \ln(f))], \quad (2.36)$$

can be identified as an intrinsic Helmholtz free energy by comparison with Eq. (2.20), which does not depend on the external field. Finally, the intrinsic Helmholtz free energy can be further separated into an ‘ideal’ part and an ‘excess’ part which gives

$$\Omega[\rho(\mathbf{r})] = F_{\text{id}}[\rho(\mathbf{r})] + F_{\text{ex}}[\rho(\mathbf{r})] + \int \rho(\mathbf{r}) (V(\mathbf{r}) - \mu) \, d\mathbf{r}, \quad (2.37)$$

where $F_{\text{id}}[\rho(\mathbf{r})] = \int k_B T \rho(\mathbf{r}) (\ln(\Lambda^3 \rho(\mathbf{r})) - 1) \, d\mathbf{r}$ is the exact free energy for an ideal gas. The thermal de-Broglie wavelength, Λ , can be determined for real fluids if desired although it only appears as a scaling factor, as such it does not alter phase transitions and other phenomena of interest and can safely be set to $\Lambda = 1$. All contributions from the fluid-fluid particle interactions are contained within F_{ex} and this functional must almost always be approximated. It is only known exactly in a few special cases such as for a one dimensional (1D) fluid of hard rod mixtures [26]. Finding a good approximation for F_{ex} is one of the main challenges associated with DFT.

Since, from Eq. (2.34), the equilibrium probability density is the one which minimises the free energy functional then it must also satisfy the Euler-Lagrange equation

$$\frac{\delta \Omega[\rho]}{\delta \rho(\mathbf{r})} = k_B T \ln(\Lambda^3 \rho(\mathbf{r})) + \frac{\delta F_{\text{ex}}}{\delta \rho} + V(\mathbf{r}) - \mu = 0. \quad (2.38)$$

The solution to this equation gives the equilibrium density profile. It is usually appro-

priate to solve such an equation numerically and it is common practice to implement a simple Picard iteration scheme to this end. Picard iteration proceeds by rearranging Eq. (2.38) into a form where the density profile is given as an expression which itself depends on the density profile like so

$$\rho(\mathbf{r}) = \Lambda^{-3} \exp \left[\beta \left(-\frac{\delta F_{\text{ex}}}{\delta \rho} - V(\mathbf{r}) + \mu \right) \right]. \quad (2.39)$$

Successive iterations of the above, with a suitable initial approximation for $\rho(\mathbf{r})$, lead to the equilibrium density profile. There are many possible forms in which one may express Eq. (2.39), one particularly useful form is

$$\rho(\mathbf{r}) = \rho_b \exp(c^{(1)}(\mathbf{r}) - \beta V(\mathbf{r}) - c^\infty), \quad (2.40)$$

where $c^{(1)} = -\beta \delta F_{\text{ex}} / \delta \rho$ is the one-body direct correlation function and ρ_b is the uniform bulk fluid density. The constant c^∞ , which depends on the choice of μ and T , is the value of the one-body direct correlation function in the bulk fluid. It is found by requiring that as $\mathbf{r} \rightarrow \infty$ then $V(\mathbf{r}) \rightarrow 0$ and $\rho(\mathbf{r}) \rightarrow \rho_b$, to satisfy this, the term in the exponent in Eq. (2.40) must be zero as $\mathbf{r} \rightarrow \infty$. This is ensured by c^∞ which is defined $c(\mathbf{r}) \rightarrow c^\infty$ as $r \rightarrow \infty$. The exact form of Eq. (2.40) arises from separating the chemical potential in Eq. (2.39) into ideal and excess parts, $\mu = \mu_{\text{id}} + \mu_{\text{ex}}$. Considering only an ideal gas, in the bulk one finds that

$$\mu_{\text{id}} = k_B T \ln(\Lambda^3 \rho_b), \quad (2.41)$$

and then inserting this into Eq. (2.39) leads to Eq. (2.40) where $\mu_{\text{ex}} = -c^\infty$. Obviously in Eq. (2.40) the value of the bulk fluid density must be known, and the chemical potential can be found from this. The reverse is true of Eq. (2.39). The algorithm for performing this minimisation procedure is given in Chapter 3.

2.2 Approximations of the Free Energy

A great number of different approximations for the excess Helmholtz free energy F_{ex} have been developed, some having a fairly wide range of applicability and others being more specialised, see Ref. [23] for a review of different approaches. The excess Helmholtz free energy needs to account for the interactions taking place between the fluid particles. It is usually a reasonable assumption in liquids to consider only pair interactions and neglect all three-body and higher interactions. Numerous different models for pair interactions have been proposed, perhaps the most simple is that of hard-spheres where the pair interaction is defined

$$v_{hs}(r) = \begin{cases} \infty & \text{for } 0 < r \leq \sigma \\ 0 & \text{for } r > \sigma, \end{cases} \quad (2.42)$$

where σ is the diameter of a hard sphere. The hard sphere potential contains only a repulsive term which models the impenetrability of the spheres, this is what makes the spheres ‘hard’. Other than this the particles do not interact with each other. The hard sphere potential is not a very realistic model for the interactions between atoms and molecules as there is no attempt made to model the attractive forces between particles. However, despite the potential not being too representative of the true physics of the fluid, it remains a very useful model potential as will be discussed shortly. More realistic model potentials exhibit a longer ranged attractive component as well as a short ranged repulsion and include the square-well and Lennard-Jones 12-6 potentials. A very simple approximation for the Helmholtz free energy is to make a gradient expansion in F_{ex} [22, 27, 28], which is applicable for fluids with short ranged interactions and only valid for slowly varying density profiles. Another approximation is to make a functional Taylor expansion about some reference density [22].

If one considers a fluid where the particles interact only via pair interactions, then differentiating the grand free energy with respect to the pair potential $v(\mathbf{r}_1, \mathbf{r}_2)$ leads to

$$\frac{\delta\Omega}{\delta v(\mathbf{r}_1, \mathbf{r}_2)} = \frac{\delta F_{\text{ex}}}{\delta v(\mathbf{r}_1, \mathbf{r}_2)} = \frac{1}{2}\rho^{(2)}(\mathbf{r}_1, \mathbf{r}_2), \quad (2.43)$$

where $\rho^{(2)}(\mathbf{r}_1, \mathbf{r}_2)$ is the two body density distribution. An expression for F_{ex} can now be found in principle by performing a functional integration of Eq. (2.43). This integration must be performed using a “charging” parameter α [23]:

$$v_\alpha(\mathbf{r}_1, \mathbf{r}_2) = v_r(\mathbf{r}_1, \mathbf{r}_2) + \alpha v_p(\mathbf{r}_1, \mathbf{r}_2). \quad (2.44)$$

This separates $v(\mathbf{r}_1, \mathbf{r}_2)$ into a reference potential v_r and a perturbation v_p where the reference potential is often the repulsive part of the pair interaction and the perturbation is the attractive part. The parameter α acts to “turn on” the attraction, this charging goes from $\alpha = 0$, corresponding to purely repulsive interactions, to $\alpha = 1$ which corresponds to the full pair potential. Performing this integration gives

$$F_{\text{ex}}[\rho(\mathbf{r})] = F_r[\rho(\mathbf{r})] + \frac{1}{2} \int_0^1 \iint \rho(\mathbf{r}_1, \mathbf{r}_2; v_\alpha) v_p^{(2)}(\mathbf{r}_1, \mathbf{r}_2) d\mathbf{r}_1 d\mathbf{r}_2 d\alpha, \quad (2.45)$$

where $\rho^{(2)}(\mathbf{r}_1, \mathbf{r}_2; v_\alpha)$ is the two body density distribution that depends on the “charged” pair potential v_α . The one body density profile $\rho(\mathbf{r})$ must not change with α and so an additional, fictitious, external potential, which changes with α , is required to enforce this. This additional potential vanishes for $\alpha = 1$ leaving only the true external potential.

The above result in Eq. (2.45) forms the basis of so-called “perturbation theories” where some specification for $\rho(\mathbf{r}_1, \mathbf{r}_2; v_\alpha)$ must be found. A simple approximation is to

take $\rho^{(2)}(\mathbf{r}_1, \mathbf{r}_2; v_\alpha) = \rho(\mathbf{r}_1)\rho(\mathbf{r}_2)$, independent of the choice of α . This leads to

$$F_{\text{ex}}[\rho(\mathbf{r})] = F_r[\rho(\mathbf{r})] + \frac{1}{2} \iint \rho(\mathbf{r}_1)\rho(\mathbf{r}_2)v(|\mathbf{r}_1 - \mathbf{r}_2|) d\mathbf{r}_1 d\mathbf{r}_2, \quad (2.46)$$

where F_r is the free energy of the reference fluid. Hard-sphere systems make an ideal candidate for that reference fluid and so it is important to be able to accurately model the hard-sphere system in order to obtain reasonable results for the full system. The most basic representation of hard-spheres is to make a local density approximation (LDA),

$$F_r[\rho] = F_{\text{hs}}[\rho] = \int f_{\text{hs}}(\rho(\mathbf{r})) d\mathbf{r}, \quad (2.47)$$

where f is a purely local function of the density profile [29]. The next step beyond a LDA is to introduce a weighted density approximation (WDA) whereby a weighted (averaged) density is constructed from the true density profile

$$n(\mathbf{r}) = \int \rho(\mathbf{r}')w(\mathbf{r} - \mathbf{r}') d\mathbf{r}', \quad (2.48)$$

which is then used to give the hard sphere free energy as a functional of a local function of this weighted density

$$F_{\text{hs}} = \int f(n(\mathbf{r})) d\mathbf{r}. \quad (2.49)$$

An early example of a WDA [30] uses the weight function

$$w(r) = \frac{3}{4\pi\sigma^3}\Theta(\sigma - r), \quad (2.50)$$

where Θ is the Heaviside step function. Many WDA models have been developed, but perhaps the most successful is fundamental measure theory developed by Rosenfeld and described in the next section. All WDA schemes also satisfy the contact density theorem [31], which, for purely hard systems (where there is no attraction between fluid particles or with an external boundary) is

$$\beta p = \rho_c, \quad (2.51)$$

where ρ_c is the fluid density at the point of contact with an external boundary. This sum rule relates the pressure of the fluid with the density at contact, it also provides a useful consistency check when solving such problems.

2.3 Fundamental Measure Theory

Fundamental measure theory (FMT) provides a very good approximation for the functional $F_{\text{hs}}[\rho]$ for a hard sphere system [14, 32, 33, 34, 35]. This makes FMT ideal for calculating the properties of the reference fluid for perturbation methods of the form

of Eq. (2.46). FMT is a class of WDA first formulated by Rosenfeld [32] with various subsequent adjustments made by others [33, 36, 37, 38]. Variations of FMT have even gone so far as to address hard polyhedra as well as hard spheres [39]. Of primary focus here is the ‘White Bear’ version of FMT for hard-spheres formulated by Roth *et al.* in Ref. [33] and independently derived by Wu *et al.* in Ref. [40]. This updated version uses a different equation of state to the original Rosenfeld derivation and is slightly more accurate close to the contact region when compared with simulation data.

The main idea of FMT is similar to that of WDAs, that the excess Helmholtz free energy can be expressed with weighted densities. Here though, the free energy is expressed as an integral over a function of a set of weighted densities, rather than just a single weighted density, i.e.

$$F_{\text{ex}} = \int \Phi(\{n_\alpha\}) d\mathbf{r}, \quad (2.52)$$

where the set of weighted densities $\{n_\alpha(\mathbf{r})\}$ are found, as before, as convolutions between the one-body density profile $\rho(\mathbf{r})$ and a set of weight functions $\{w_\alpha(\mathbf{r})\}$,

$$n_\alpha(\mathbf{r}) = \int \rho(\mathbf{r}') w_\alpha(\mathbf{r} - \mathbf{r}') d\mathbf{r}'. \quad (2.53)$$

The set of weight functions consists of four scalar weights and two vector weights defined by

$$\begin{aligned} w_3(\mathbf{r}) &= \Theta(R - r), \\ w_2(\mathbf{r}) &= \delta(R - r), \\ w_1(\mathbf{r}) &= \frac{w_2(\mathbf{r})}{4\pi R}, \\ w_0(\mathbf{r}) &= \frac{w_2(\mathbf{r})}{4\pi R^2}, \\ \mathbf{w}_2(\mathbf{r}) &= \frac{\mathbf{r}}{r} \Theta(R - r), \\ \mathbf{w}_1(\mathbf{r}) &= \frac{\mathbf{w}_2(\mathbf{r})}{4\pi R}, \end{aligned} \quad (2.54)$$

where Θ is the Heaviside step function, δ is the Dirac delta function, R is the radius of a hard sphere and $r = |\mathbf{r}|$. Integrating over the w_3 , w_2 and w_1 gives the volume, surface area and radius of a sphere. Depending upon the manner in which Φ is derived it can take various forms, the White-Bear version is [33]

$$\Phi(\{n_\alpha\}) = -n_0 \ln(1 - n_3) + \frac{n_1 n_2 - \mathbf{n}_1 \cdot \mathbf{n}_2}{1 - n_3} + (n_2^3 - 3n_2 \mathbf{n}_2 \cdot \mathbf{n}_2) \frac{n_3 + (1 - n_3)^2 \ln(1 - n_3)}{36\pi n_3^2 (1 - n_3)^2}. \quad (2.55)$$

For a uniform bulk fluid this gives the Carnahan-Starling equation of state [14].

In order to solve the Euler-Lagrange equation, Eq. (2.38), the one body direct corre-

lation function must be calculated. This is found to be

$$c^{(1)}(\mathbf{r}) = - \sum_{\alpha} \left(\int \frac{\delta\Phi}{\delta n_{\alpha}}(\mathbf{r}') w_{\alpha}(\mathbf{r}' - \mathbf{r}) d\mathbf{r}' \right). \quad (2.56)$$

Further details can be found in Ref. [34]. Note also the change in sign in the argument of the weight function which affects the vector weights. If the system under study is periodic, all of the required convolutions, both for the weighted densities and the one body direct correlation function, can be performed in Fourier space which is very useful for larger systems. Non-periodic systems can usually be made periodic; they must just be large enough to avoid unwanted effects such as wrap around effects from structures interacting with their own periodic image. When numerically solving Eq. (2.38), the numerical routine will break down if $n_3(\mathbf{r}) > 1$ at any value of \mathbf{r} at any iteration as Eq. (2.55) becomes undefined. Simply iterating Eq. (2.40) can cause very large changes in the density profile between each iteration, particularly when the density profile is far from its equilibrium value. The size of these changes can be restricted and this in turn prevents Eq. (2.55) becoming undefined. To restrict the step size, one first calculates the updated density profile via Eq. (2.40). This updated profile is denoted ρ_{up} , then a small proportion of this profile is mixed with the density profile from the previous iteration step to find the new density profile:

$$\rho_{\text{new}} = \alpha \rho_{\text{up}} + (1 - \alpha) \rho_{\text{prev}}, \quad (2.57)$$

where α is the proportion of the trial density profile, ρ_{up} , that is mixed with the previous profile, ρ_{prev} . In Ref. [34], Roth also sets out a method by which the choice of α is optimised at each step to be as large as possible using a rudimentary line search. Following the Picard iteration scheme until it converges gives the equilibrium density profiles shown in Fig. 2.1.

The density profiles in Fig. 2.1 are for a hard-sphere fluid against a hard planar wall. Higher density fluids show a greater amount of structuring in the contact region close to the wall. This structuring is caused by layers of particles stacking against the substrate. The density at the point at which the fluid makes contact with the wall is the contact density, on the figure this is at $z = \sigma/2$, and as previously discussed, this satisfies the contact theorem [23, 31, 34]

$$\rho(z = \sigma/2) = \beta p. \quad (2.58)$$

The present FMT model as described is not sufficient to describe the freezing of hard spheres but with a suitable modification, where a tensor weight is added, this deficiency can be corrected [38, 41, 42]. The focus of this thesis does not concern any crystalline structure and so this tensor modification is not implemented here.

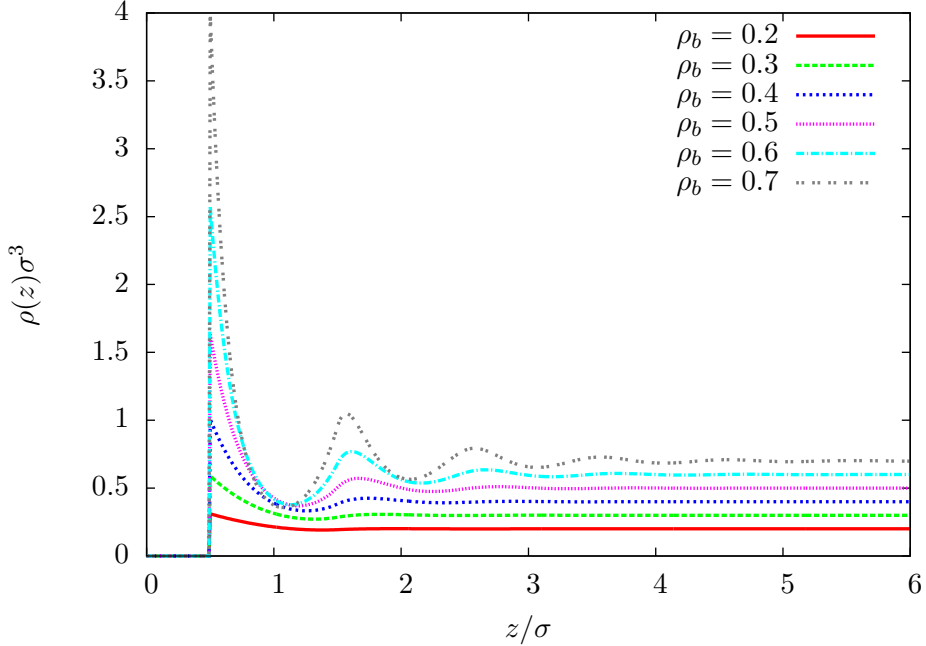


Figure 2.1: Density profiles of a hard-sphere fluid against a hard planar wall for a range of bulk fluid densities. The fluid is modelled using the continuum DFT model introduced in this chapter. As the density is increased, more structure is seen in the profiles in the region close to the wall. The density profiles then decay to their bulk values.

2.3.1 Reduced Dimensions

It is often the case that a system of interest has an external field that does not vary in all three spatial dimensions. This is the case in Fig. 2.1, where the potential only depends on the perpendicular distance of a fluid particle from the hard planar wall surface and not on its position in either of the other two dimensions tangent to the wall. In such a situation it is useful to take advantage of the symmetry of the equilibrium density profile which always mirrors that of the external field [22, 43]. Thus, if

$$V(\mathbf{r}) = V(x, y), \quad (2.59)$$

say, then

$$\rho(\mathbf{r}) \rightarrow \rho(x, y), \quad (2.60)$$

at equilibrium. The computational effort required to find the equilibrium density profile in such a situation is greatly reduced by analytically integrating over the invariant dimensions in the convolutions. For example, as in Fig. 2.1, if the external field only varies in one direction (usually taken to be the z direction) then $\rho(x, y, z) = \rho(z)$, and

the weighted density convolution becomes

$$\begin{aligned} n_\alpha &= \iiint \rho(x', y', z') w_\alpha(x - x', y - y', z - z') dx dy dz, \\ &= \int \rho(z') w_\alpha^{1D}(z - z') dz, \end{aligned} \quad (2.61)$$

where

$$w_\alpha^{1D}(z) = \iint w_\alpha(x, y, z) dx dy. \quad (2.62)$$

When reducing the model to an effective 1D version, the corresponding weight functions are

$$\begin{aligned} w_3^{1D}(z) &= \pi(R^2 - z^2) \Theta(R - |z|), \\ w_2^{1D}(z) &= 2\pi R \Theta(R - |z|), \\ \mathbf{w}_2^{1D}(z) &= 2\pi z \mathbf{e}_z \Theta(R - |z|), \end{aligned} \quad (2.63)$$

where w_1 , w_0 and \mathbf{w}_1 are related as in Eq. (2.54) and \mathbf{e}_z is the unit vector in the z direction. The weight functions for an effective two dimensional (2D) model can similarly be found:

$$\begin{aligned} w_3^{2D}(\mathbf{r}_0) &= 2\sqrt{R^2 - r_0^2} \Theta(R - r_0), \\ w_2^{2D}(\mathbf{r}_0) &= \frac{2R}{\sqrt{R^2 - r_0^2}} \Theta(R - r_0), \\ \mathbf{w}_2^{2D}(\mathbf{r}_0) &= \frac{2\mathbf{r}_0}{\sqrt{R^2 - r_0^2}} \Theta(R - r_0), \end{aligned} \quad (2.64)$$

where $\mathbf{r}_0 = (x, y)$ and $r_0 = |\mathbf{r}_0|$ is the length of this vector, as before, the remaining three weight functions have the same relation as in Eq. (2.54). Note that both $w_2^{2D}(\mathbf{r}_0)$ and $\mathbf{w}_2^{2D}(\mathbf{r}_0)$ diverge as $r_0 \rightarrow R$. These singularities mean that it is difficult to represent the weight functions numerically in real space. However, despite this, the Fourier transforms of the weight functions remain well behaved and can be found analytically. The weight functions only ever appear as part of the convolutions in Eqs. (2.53) and (2.56) which means that, this problem is resolved if the convolutions are performed in Fourier space via the convolution theorem. The Fourier transforms of the weight functions are then used directly and the real-space functions never need to be represented numerically.

At this point, a fundamental measure DFT model has been set up and given in a form of reduced dimensionality. Before proceeding to the next chapters some additional ideas are discussed that have a bearing on the main content of this thesis.

2.4 Liquid-Gas Coexistence and Wetting

In the absence of any external field the equilibrium density profile of a fluid takes a uniform value. This value is the bulk fluid density and must satisfy the Euler-Lagrange equation, Eq. (2.38). If for a particular choice of temperature, pressure and chemical

potential (T , P and μ), there exists two densities, ρ_1 and ρ_2 , both of which satisfy the condition

$$\frac{\delta\Omega}{\delta\rho}\Big|_{\rho=\rho_1} = \frac{\delta\Omega}{\delta\rho}\Big|_{\rho=\rho_2} = 0, \quad (2.65)$$

and also satisfy $\Omega[\rho_1] = \Omega[\rho_2]$ then the two densities represent two distinct phases that are said to coexist. The two states, with densities ρ_1 and ρ_2 , have the same chemical potential, pressure and temperature and, energetically, it is equally favourable to be at either fluid density. Usually these two densities will correspond to a dense liquid phase of the fluid and a sparse gas phase, denoted ρ_l and ρ_g respectively. The coexisting liquid and gas densities over a range of temperatures are displayed in a phase diagram such as that shown in Fig. 2.2 for a fluid where the free energy is approximated by Eq. (2.46). The calculation of a phase diagram is demonstrated in Chapter 3. Two curves are shown in Fig. 2.2, the binodal (red curve) displays the coexisting liquid and gas densities for particular choices of temperatures where it is also assumed that $\mu = \mu_c$, the chemical potential at liquid-gas coexistence. The spinodal (blue curve) is the locus where the compressibility is predicted to go to zero and is also the point where in a dynamical theory for the liquid, such as dynamical density functional theory (DDFT), the fluid becomes linearly unstable [54]. A uniform fluid at a state point inside this curve will spontaneously separate into its liquid and gas phases. As the temperature is increased the coexisting densities of the two phases come closer together until they merge at the critical point, above which there is only one fluid phase.

The hard-sphere model described in §2.3 can not describe liquid-gas phase separation since there is no attraction between particles. As discussed previously, it is possible to construct a FMT functional that can model the crystal phase. In this case the model can exhibit a fluid-crystal phase transition which leads to a different phase diagram. The attraction between particles is necessary to describe liquid-gas phase separation as there must be an energetic gain from having densely packed particles to offset the energetic cost, governed by the chemical potential, of increasing the number of particles in the system. One can then tune a system at a fixed temperature towards liquid-gas coexistence by adjusting the chemical potential. For a given temperature there is one value of the chemical potential that will allow coexisting liquid and gas.

In the bulk, a fluid at the point of liquid-gas coexistence is equally likely to be in either phase as both have the same value of the grand free energy. In the presence of an external field, i.e. at a surface, this is not the case and wetting phenomena can occur. In a microscopic model, formulated in the grand canonical ensemble, such as DFT, particles are free to enter and leave the system, governed by the chemical potential. Consider the implications of this for a liquid droplet on a substrate, at coexistence with its vapour. If the contact angle of the droplet is $\theta > 0^\circ$ (see Fig. 1.1), then from Young's equation,

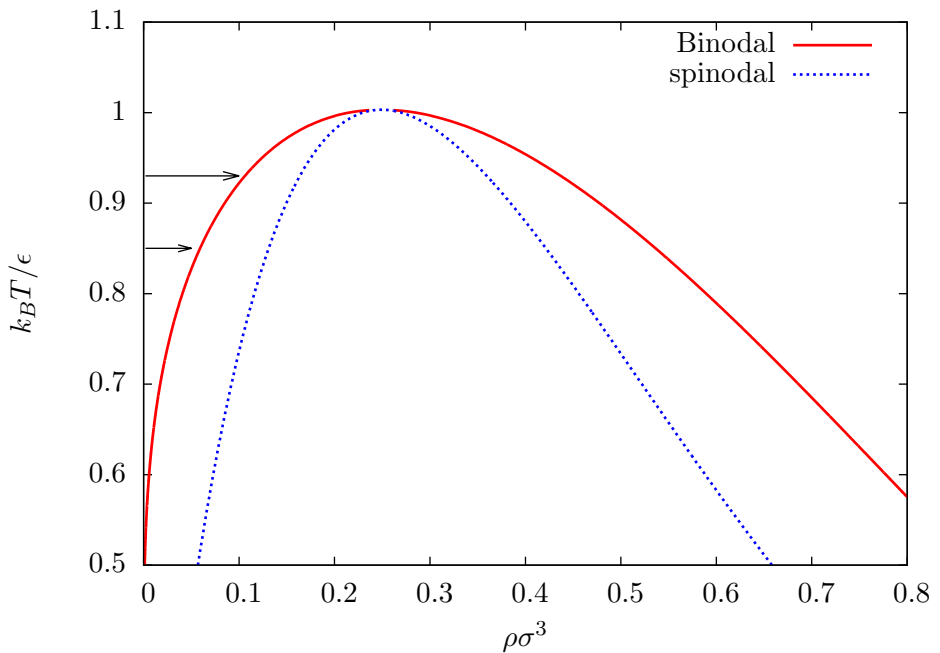


Figure 2.2: The binodal curve (solid red) for the model fluid described in Chapter 4. The curve shows the two coexisting fluid densities for various temperatures. Above the critical temperature T_c phase separation no longer occurs. The spinodal curve (blue dashed) shows the point of linear instability of the fluid. The black arrows show the density increasing on approaching liquid-gas coexistence as the chemical potential is increased.

Eq. (1.1), the surface tensions are related

$$\gamma_{wg} < \gamma_{wl} + \gamma_{lg}. \quad (2.66)$$

Fluid particles will leave the system to eliminate the liquid phase, thereby eliminating the wall-liquid and liquid-gas interfaces and replacing them with the single wall-gas interface. As such it is not possible for a droplet to be an equilibrium structure in the grand canonical ensemble, since the single wall-gas interface is always more energetically favourable, i.e. the droplet evaporates.

Consider case (c) of Fig. 1.1, where $\theta = 0^\circ$ and the ‘droplet’ is really a liquid film. In this case the substrate must be attractive and so, in a grand canonical system, more particles enter the system to lower the free energy and so the liquid film grows until the entire domain is filled with liquid. Therefore, at a planar substrate when $\mu < \mu_c$, the value at coexistence, there are only two possible equilibrium structures in the grand canonical ensemble: either the low density gas fills the system, or the higher density liquid does. This could also be inferred from noting that the liquid-gas interface always has an energetic cost associated with it. The two possible equilibrium structures both exclude this interface. Wetting is identified as the liquid filling the system and non-wetting when the gas fills the system. Note that in Chapter 1 a ‘partially wetting’ case was discussed, microscopically, this is subsumed into the non-wetting class. The phenomena described here rely on the fluid being at a point of liquid-gas coexistence, $\mu = \mu_c$. If instead, the chemical potential is lower than its coexistence value, then the bulk phase far from the wall is the gas phase regardless of the substrate. Similarly, for $\mu > \mu_c$ the liquid phase always forms far from the wall. However, for a wall that is say, wet at $\mu = \mu_c$, when $\mu < \mu_c$ one can find a thick but finite film of the liquid on the wall. As $\mu \rightarrow \mu_c$, the thickness of this film then diverges.

This description of wetting holds for planar substrates. On a curved substrate, the curvature of the interfaces can restrict the size of the liquid film [44, 45]. A liquid film of a finite thickness then forms instead of the infinitely thick film that forms for a planar interface. To find an equilibrium state consisting of a droplet resting on a substrate one must treat the system in the canonical ensemble with a fixed number of particles. It is demonstrated in later chapters that it is possible to describe such a droplet structure with DFT by constraining the average density of the system. The droplet is then a constrained equilibrium structure.

The excess fluid density at an interface, known as the adsorption, is calculated as

$$\Gamma = \frac{1}{A} \int (\rho(\mathbf{r}) - \rho_b) d\mathbf{r}, \quad (2.67)$$

where A is the area of the surface. This gives a convenient measure of wetting for microscopic systems. At equilibrium, if Γ is small and finite then the fluid is non-wetting.

If $\Gamma \rightarrow \infty$ then the fluid wets the interface. The wetting phase transition can be observed (or not) by adjusting certain parameters and observing the change in the adsorption. Consider a fluid at a fixed temperature T where $\mu < \mu_c$ in contact with a substrate. The adsorption at the substrate-fluid interface is small and finite. On increasing μ towards μ_c the adsorption increases because the liquid film adsorbed at the wall grows in thickness. When the chemical potential reaches the point of coexistence the adsorption either diverges towards infinity or remains small and finite, as shown in Fig. 2.3. If the adsorption diverges then this corresponds to the formation of a macroscopically thick liquid film and the fluid ‘wets’ the substrate [4]. Choosing T and μ defines a particular state point on the phase diagram, Fig. 2.2. For a fixed T , $\mu \rightarrow \mu_c^-$ corresponds to approaching the binodal in a direction perpendicular to the y axis, as marked on the phase diagram by the black arrows. In two of the adsorption isotherms shown in Fig. 2.3 a discontinuous jump to a higher density is observed. This occurs as a result of crossing the pre-wetting line and is discussed further in Chapter 3. For sufficiently high temperatures the pre-wetting line is no longer crossed on the approach to liquid-gas coexistence and no discontinuous jump occurs, this is the case for the fourth (pink) adsorption isotherm in Fig. 2.3. The location of pre-wetting line, and indeed any other wetting phenomena, is not purely a property of the fluid itself, it also depends on the properties of the interface that the fluid is in contact with. The location of the pre-wetting line is not displayed on the bulk fluid phase diagram of Fig. 2.2 as this displays properties that depend only on the fluid itself.

2.5 Surface Tension

The surface tension of an interface is the free energy per unit area cost of that interface. Density functional theory models can be used to calculate the surface tension. The exact method will be described with reference to the DFT model previously discussed. Consider an effective 1D DFT where the excess free energy is of the form of Eq. (2.46) and the reference system is a hard-sphere fluid. This calculation is simpler in one dimension but is equally applicable in higher dimensions. The surface tension of the liquid-gas interface must be calculated at the point of liquid-gas coexistence, for a system not at coexistence there is only one fluid phase and the liquid-gas interface does not exist. For the bulk system, the free energy can be calculated as

$$\Omega_b = -pV, \quad (2.68)$$

where p is the pressure and the volume, V , is just the length of the system in the effective 1D model. The surface tension can be calculated from an equilibrium density

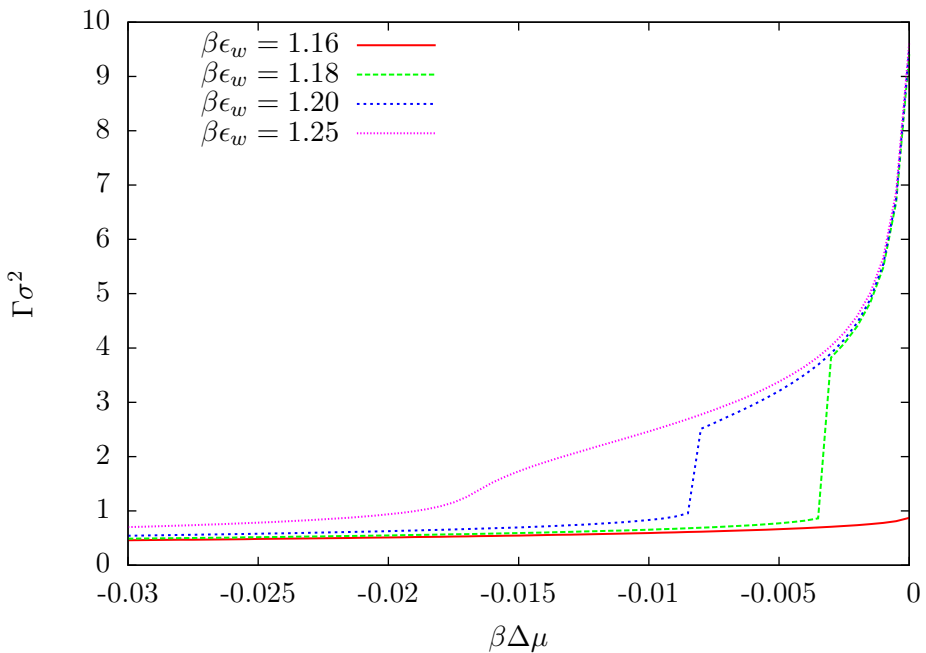


Figure 2.3: Adsorption isotherms as the chemical potential is varied towards the coexistence value. As $\Delta\mu = (\mu - \mu_c) \rightarrow 0$ the adsorption either diverges and becomes infinite if the fluid wets the interface or remains small and finite if it does not. Results for various values of the wall attraction strength parameter ϵ_w are displayed. This result is calculated using the model fluid introduced in Chapter 4.

profile sought from the initial condition

$$\rho(z) = \begin{cases} \rho_l & \text{if } L/4 < z < 3L/4 \\ \rho_g & \text{otherwise,} \end{cases} \quad (2.69)$$

where L is the length of the 1D system. The equilibrium density profile is the gas phase separated from the liquid phase by two interfaces as shown in Fig. 2.4. The system must be large enough that the bulk liquid and gas densities are attained and the two interfaces are well separated. Recall also that the equilibrium solution is calculated with periodic boundary conditions to employ the convolution theorem which necessitates two interfaces. The liquid-gas surface tension is calculated from

$$\gamma_{lg} = \frac{\Omega - \Omega_b}{2}, \quad (2.70)$$

where Ω is the grand free energy of the density profile given in Fig. 2.4. Since both the liquid and gas density have the same free energy per unit volume then the only contribution to the free energy of the system, beyond that of the bulk energy, is that from the two interfaces, i.e. the surface tension. The division by 2 in Eq. (2.70) is to account for the presence of two interfaces. In this 1D system the interface has unit area, in higher dimensions the excess free energy of the system would also need to be divided by the area of the interface to find the surface tension. The ‘equilibrium’ solution presented in Fig. 2.4 is not the true equilibrium solution (it is not a global minimum of the free energy), this is just a meta-stable equilibrium point at which the minimisation routine stalls. The true equilibrium solution is simply the bulk fluid.

A wall fluid interface is calculated in a similar manner. The equilibrium density profile is found from an initial condition of the bulk fluid against the wall. The wall-fluid surface tension is found as the excess free energy. In this instance there is only a single interface so there is no need to divide the result by two, as in Eq. (2.70). Both the wall-liquid, γ_{wl} , and the wall-gas, γ_{wg} , surface tensions are found in this manner, only one of these results will be a true equilibrium, the other will be a local minimum of the free energy depending on if the fluid wets the wall or not.

2.6 The Binding Potential

The binding potential, $g(h)$, was introduced in Chapter 1 and asymptotic forms (e.g. Eq. (1.4)) were presented for it. Further details of its properties are now given. A fluid, at the point of liquid-gas coexistence with a fixed average density will phase separate into its two distinct phases and, in the absence of gravity, one phase will form a sphere surrounded by the other phase. This is the equilibrium configuration for the fluid. Since the free energy per unit volume of the gas phase is equal to that of the liquid phase,

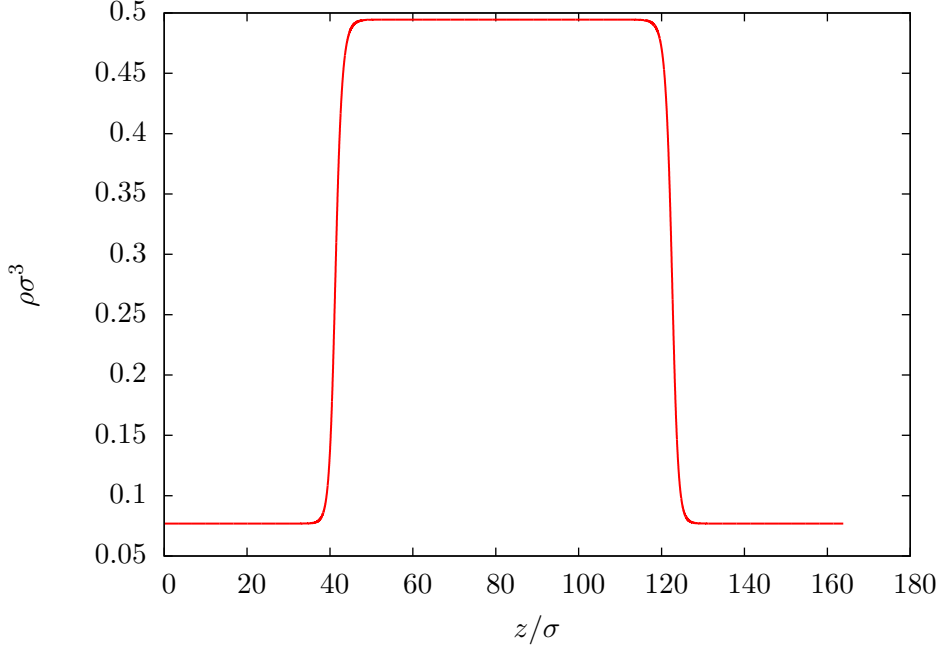


Figure 2.4: The equilibrium density profile used to calculate the surface tension from the model fluid described in Chapter 4. Two interfaces are necessary due to the periodicity of the system, the surface tension is half the excess (above bulk) free energy of the system.

the free energy of the entire system is simply be the bulk free energy of the system for that volume plus an additional contribution from the surface tension of the liquid-gas interface, i.e.

$$\Omega = V\omega_b + A\gamma_{lg}, \quad (2.71)$$

where ω_b is bulk free energy per unit volume of the fluid and the volume and interfacial area are given by V and A respectively. It is assumed here that the contribution to Ω in the above due to the curvature of the liquid-gas interface is negligible. Curvature introduces a correction of $O(\sigma/R)$ to Eq. (2.71) where R is the radius of curvature. The situation becomes more complex in the presence of a planar wall where the liquid forms a film of thickness h on the wall as depicted schematically in Fig. 2.5. Before describing the free energy of this system it is useful to relate the thickness, h , of the liquid film to the adsorption of the system

$$\Gamma \approx h(\rho_l - \rho_g). \quad (2.72)$$

The adsorption is a much more appropriate measure of the thickness of the film at microscopic length scales. In particular, this is because for very weakly attractive or repulsive walls, the contact density of the fluid could be less than the bulk value which would give a negative adsorption. A negative film height does not make conceptual sense but would clearly be required to describe such a situation. Secondly, a film height is

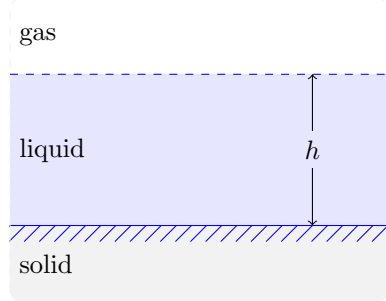


Figure 2.5: A schematic of the system from which the binding potential is calculated. A liquid film separates a semi-finite slab of gas from a solid planar wall.

harder to define microscopically as the interfaces are diffuse so some specification must be made on what exactly a film height is; where does the liquid film end and the gas begin?

Using the adsorption as the measure of film thickness the grand free energy of this system can now be given as

$$\Omega(\Gamma) = V\omega_b + A(\gamma_{wl} + \gamma_{lg} + g(\Gamma)). \quad (2.73)$$

The binding potential $g(\Gamma)$ can then be identified as the excess energetic contribution to the grand free energy beyond that of the surface tensions and, since everything else in the system is accounted for, it must describe an effective interaction between the two interfaces.

A selection of binding potentials are displayed in Fig. 2.6. These binding potentials are calculated using the method presented below in Chapter 4 for a model Lennard-Jones (LJ) fluid at a planar wall with varying attractive strength. The parameter f denotes the attractive strength of the wall. For the most attractive case of $f = 1.4$ the binding potential has a single energetic minimum occurring as $\Gamma \rightarrow \infty$, the adsorption becoming infinite at equilibrium is precisely the definition of wetting. As f decreases a second minimum appears at a low value of the adsorption. This represents a meta-stable non-wetting state but the true equilibrium is still a thick wetting film. Eventually, as f is further decreased, this local minimum at low adsorption becomes the global minimum. This first happens in the figure for $f = 1.0$. The equilibrium state of the system is now corresponding to a small value of the adsorption, it is non-wetting. The contact angle that a liquid droplet makes with a substrate can also be found from the binding potential:

$$\theta = \cos^{-1} \left(1 + \frac{g(h_0)}{\gamma_{lg}} \right), \quad (2.74)$$

where h_0 is the equilibrium film thickness. Note also in Fig. 2.6 that there is an energetic barrier separating one state from the other. When seeking equilibrium solutions to the

grand free energy it is important to bear this in mind when selecting an initial condition as the solution could become stuck at what is only a local minimum of the free energy.

If the system is not at coexistence then an additional term of $A\Gamma(\mu_c - \mu)$ needs to be added to Eq. (2.73) to account for the energetic cost of forming a liquid instead of a gas. For $\mu < \mu_c$ this additional term causes the tail of the binding potential to rise and then $\Gamma \rightarrow \infty$ ceases to be a minimum of the free energy as shown in Fig. 2.7. Two different finite adsorptions can then be minima of the free energy and, for a particular choice of μ these could both be the global energetic minimum. Note that in Fig. 2.7, for $\Delta\mu \neq 0$ the minimum of the free energy is found at a small finite adsorption. When the chemical potential reaches its coexistence value ($\Delta\mu = 0$), the global minimum now occurs at an infinite adsorption. There exists a value of μ as $\Delta\mu \rightarrow 0$ where the global minimum of the free energy shifts to a higher value of the adsorption (this higher value of the adsorption tends to infinity as coexistence is approached). This particular point corresponds to the crossing of the pre-wetting line discussed in §2.4. Choosing a chemical potential off coexistence will constrain a particular average density and gives one method by which the particle number may be constrained in a system. A different constraint, not requiring a global change in the chemical potential will be introduced in Chapter 3 which will be required when calculated a binding potential. Chapters 3 and 4 now set up a DFT for the purpose of demonstrating a method by which the binding potential may be calculated from a microscopic viewpoint which can then be used in larger scale models.

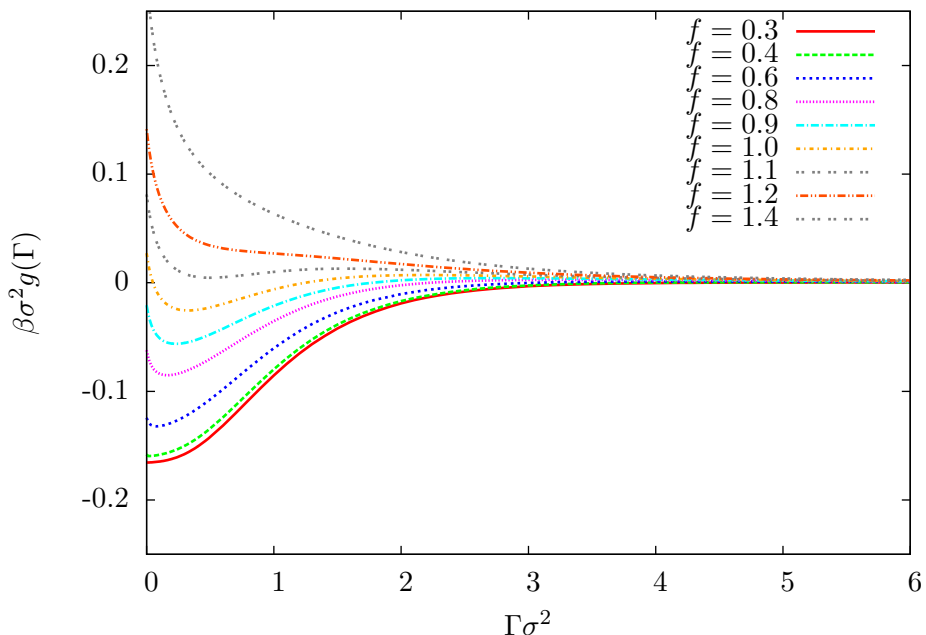


Figure 2.6: Binding potentials for the model fluid described in Chapter 4 against substrates of varying attractive strength, f . Wetting behaviour is determined from the binding potentials. Low adsorption global minima indicate non-wetting fluids while global energetic minima occurring as $\Gamma \rightarrow \infty$ indicate a wetting fluid.

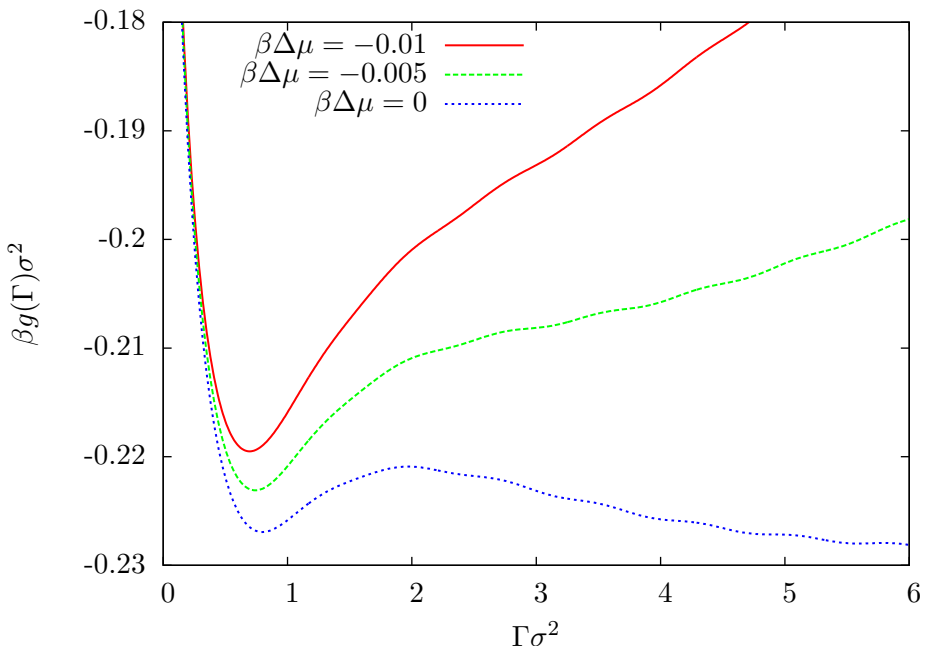


Figure 2.7: The excess free energy calculated for the discrete model described in Chapter 3, parametrised by $\beta\epsilon = 0.9$ and $\beta\epsilon_w = 0.74$. As the chemical potential moves away from the value at liquid-gas coexistence the free energy of the thick liquid film increases. The free energy increases with increasing Γ .

Chapter 3

A Discrete DFT Model

This chapter, based on the work published in Refs. [18] and [19], introduces a discrete DFT, the lattice-gas (LG) model, and it is used to demonstrate the calculation of binding potentials. This simple DFT model provides a rather crude description of a fluid but despite this it is still able to display much of the physics one would expect to see in the full system. Even though there are some aspects of the model that are not as accurate as would be desired this is offset by the ease and speed by which results can be calculated. Due to the simplicity of this model, one can very quickly develop intuition and understanding about the real system. In addition to this, it is also possible to tackle more complex systems [46] that would be difficult to tackle with more accurate, but computationally expensive, continuum models. One final advantage is that, since this is a discrete model, all of the integrals that occur in the continuum model now appear as summations which can be calculated much faster. Much larger systems can be handled as a result of this extra computational efficiency. In this chapter the LG model is derived and then used to demonstrate some basic properties of the model. The derivation can be compared with that of a general continuum DFT model from Chapter 2. A method is then described where the average adsorption can be constrained and this is then used to calculate droplet density profiles and binding potentials. Some shortcomings with the model are also discussed which necessitates the application of the continuum model that is used in the next chapter.

3.1 The Lattice Gas Model

The space of a 3D system consisting of N identical, hard spherical particles is covered by a discrete cubic lattice. The fluid particles are then constrained to each sit entirely within a single lattice site, as shown schematically in Fig. 3.1. Each lattice site is a cube with a side length equal to the diameter of a fluid particle σ . As such only a single fluid particle can occupy a lattice site at a given time and the entire space is filled by $M = M_x \times M_y \times M_z$ lattice sites where M_x , M_y and M_z are the number of lattice sites

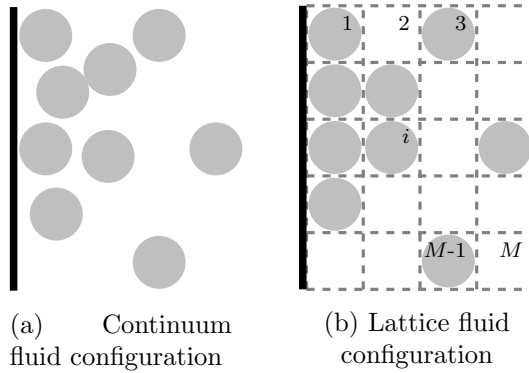


Figure 3.1: A simple continuum fluid (a) is modelled by discretising space over a lattice (b), each lattice site can be occupied by only one particle and the particles are constrained to sit wholly within one lattice site.

in the x , y and z directions respectively. Any configuration of the N particles can then be described by the set of occupation numbers $\{n_i\} = \{n_1, n_2, \dots, n_M\}$ which specify if a site is occupied by a fluid particle ($n_i = 1$) or empty ($n_i = 0$).

As discussed in Chapter 2, the kinetic energy contribution to the Hamiltonian can be integrated out, it is only the potential energy of the fluid, i.e. that arising from the fluid-fluid particle interactions and the interaction of the fluid particles with an external field, which determines the macroscopic behaviour of the fluid. Fluids consisting of particles with a different mass or kinetic energy say, would have different total energies but the appearance of any phase transitions or other phenomena would not be affected. It is only the positions of the particles that determine potential energy contribution which on the lattice is defined as

$$\Phi(\{n_i\}) = \sum_{i=1}^M n_i V_i - \frac{1}{2} \sum_{ij} \epsilon_{ij} n_i n_j, \quad (3.1)$$

where the first term is due to the external field arising from confining walls say, and the second term is the contribution from interactions between particles within the fluid. It has been assumed here that three-body and higher interactions between fluid particles can be neglected. The factor of a half included is to avoid double counting of the pair interactions. The summation notation used in the first term of Eq. (3.1) refers to a 3D sum over all of the lattice sites in the system, the indices $i = (i_x, i_y, i_z)$ and $j = (j_x, j_y, j_z)$ denote 3D coordinates. The notation for the second summation denotes a double sum over all possible pairs of lattice sites. This shorthand notation is used

frequently throughout this chapter, written out fully this is

$$\sum_{ij} \epsilon_{ij} n_i n_j = \sum_{i=1}^M \sum_{\substack{j=1 \\ j \neq i}}^M \epsilon_{ij} n_i n_j. \quad (3.2)$$

The strength of a pair interaction between two particles at \mathbf{i} and \mathbf{j} is determined by the parameter ϵ_{ij} which is fully defined later.

In analogy with Eq. (2.8) the probability of the particles being in a particular configuration is

$$P(\{n_i\}) = \frac{e^{-\beta \Phi(\{n_i\})}}{Z}, \quad (3.3)$$

where the partition function is defined as

$$Z = \sum_{\text{all states}} e^{-\beta \Phi_{\text{state}}}, \quad (3.4)$$

where Φ_{state} is a shorthand for the potential energy of a particular state, a state here simply refers to a particular configuration of particles.

The LG model is a discrete, rather than a continuous, DFT and as such the grand potential turns out to be a function of the set of lattice densities $\{\rho_i\}$ and not a functional. Such a function can be derived in the following rather intuitive manner. A more rigorous derivation follows. The Helmholtz free energy is calculated from the partition function as

$$F = -k_B T \ln Z, \quad (3.5)$$

but for a fluid defined by the Hamiltonian Eq. (3.1) this partition function is very difficult to evaluate. Making certain assumptions to simplify this Hamiltonian allows some progress to be made. Consider a totally non-interacting system, i.e. $V_i = 0$ and $\epsilon_{ij} = 0$ for all i and j . Every configuration of particles is now equally likely and so the partition function is just the total number of possible configurations for the system of M cells and N particles i.e.

$$Z = \frac{M!}{N!(M-N)!}. \quad (3.6)$$

Using this definition, along with Stirling's approximation that $\ln(N!) \approx N \ln N - N$, in Eq. (3.5) gives

$$F = -k_B T [M \ln M - N \ln N - (M-N) \ln(M-N)], \quad (3.7)$$

since Stirling's approximation is applied it is necessary that both M and N are large. The ultimate goal is to end up with a function of the density profile, with that in mind, using the definition of the bulk number density ($\rho = N/M$), the free energy function is

rewritten as

$$F = Mk_B T [\rho \ln \rho + (1 - \rho) \ln(1 - \rho)]. \quad (3.8)$$

This now leads to an expression for the free energy in terms of the fluid density, for a non-interacting system. The system has been made non-interacting by turning off the attractive fluid-fluid interactions and removing the external field. There remains a hard-sphere like interaction arising from the stipulation that only one particle can occupy a lattice site at one time. If this condition is relaxed then Eq. (3.6) no longer holds and so the final form of Eq. (3.8) must be different. The hard-core interaction can be seen in the $\ln(1 - \rho)$ term of Eq. (3.8): if $\rho > 1$ then the system is over-occupied and this term is undefined. If this is now considered a reference state then additional interactions, such as attraction between pairs of particles, can be added to this function to arrive at the version of the model which is ultimately used here. The system is then no longer at a uniform density and so the bulk number density ρ is replaced with the set of local lattice densities $\{\rho_i\}$ and the multiplication by M is replaced by a sum over all lattice sites. This is essentially the same procedure that was described by Eq. (2.46) in the previous chapter. A more rigorous derivation now follows in the grand canonical ensemble, after which it is worth looking back here to see the two derivations arriving at a similar point.

3.1.1 A Derivation via the Gibbs-Bogoliubov Inequality

This derivation tackles the problem of evaluating Eq. (3.1) by expressing the true lattice free energy as a perturbation about a simpler free energy. The Gibbs-Bogoliubov inequality is then applied to express this perturbation about the reference fluid as an upper bound on the true free energy which is then minimised to obtain a ‘best’ approximation of the full lattice fluid free energy.

Similarly to Eq. (3.3), the probability of a grand canonical system being in a particular state is

$$P(\{n_i\}) = \frac{e^{-\beta(\Phi - \mu N)}}{\Xi}, \quad (3.9)$$

where the number of particles in the system is found as

$$N = \sum_{i=1}^M n_i. \quad (3.10)$$

The grand canonical partition function is defined as

$$\Xi = \text{Tr } e^{-\beta(\Phi - \mu N)}, \quad (3.11)$$

where the trace operator is

$$\text{Tr } x = \sum_{\text{all states}} x = \sum_{n_1=0}^1 \sum_{n_2=0}^1 \cdots \sum_{n_M=0}^1 x. \quad (3.12)$$

The grand free energy is then given by

$$\Omega = -k_B T \ln \Xi, \quad (3.13)$$

and equating this with Eq. (3.11) gives

$$e^{-\beta\Omega} = \text{Tr } e^{-\beta(\Phi-\mu N)}. \quad (3.14)$$

This can be further manipulated by considering the energy for a particular state, Φ , as a perturbation to some reference state:

$$\Phi = \Phi - \Phi_0 + \Phi_0 = \Phi_0 + \Delta\Phi. \quad (3.15)$$

The currently undefined reference state here is not just the non-interacting state described in the previous section but is chosen to be a function of a set of variational parameters $\{\phi_i\}$. Separating the fluid into a perturbation about a reference system allows Eq. (3.14) to be expressed as

$$e^{-\beta\Omega} = \text{Tr } e^{-\beta(\Phi_0-\mu N)} e^{-\beta\Delta\Phi}, \quad (3.16)$$

which is precisely the definition of the statistical average of the perturbation $\Delta\Phi$ in the ensemble of particles interacting via a reference potential energy Φ_0 . The statistical average of a quantity x in the reference system is expressed as

$$\langle x \rangle_0 = \text{Tr } \left(x \frac{e^{-\beta(\Phi_0-\mu N)}}{\Xi_0} \right), \quad (3.17)$$

and so Eq. (3.16) can be rewritten as

$$e^{-\beta\Omega} = e^{-\beta\Omega_0} \langle e^{-\beta\Delta\Phi} \rangle_0, \quad (3.18)$$

where $\exp(-\beta\Omega_0) = \Xi_0$. Due to the fact that $\exp(-x)$ is a convex function of x , the relation holds that $\langle \exp(-x) \rangle \geq \exp(-\langle x \rangle)$ and so

$$e^{-\beta\Omega} \geq e^{-\beta\Omega_0} e^{-\beta\langle \Delta\Phi \rangle_0}. \quad (3.19)$$

The Gibbs-Bogoliubov inequality is then found by taking the logarithm of both sides:

$$\Omega \leq \Omega_0 + \langle \Delta\Phi \rangle_0. \quad (3.20)$$

The Gibbs-Bogoliubov inequality gives an upper bound to the true grand free energy, Ω , where this bound depends only on the reference system. The non-local terms in Eq. (3.1) mean that it is very difficult to calculate the grand free energy of the full system.

By applying Eq. (3.20) this grand free energy can be approximated by an expression depending only on the reference system. The importance of this is that the reference system can be specified by a set of local variational parameters such that the grand free energy can be found. Since this perturbation about a reference system is an upper bound to the true grand free energy, minimising it gives a ‘best’ approximation to Ω . The reference energy is specified as

$$\Phi_0 = \sum_{\mathbf{i}=1}^M (V_{\mathbf{i}} + \phi_{\mathbf{i}}) n_{\mathbf{i}}, \quad (3.21)$$

where $V_{\mathbf{i}}$ is the external field and $\{\phi_{\mathbf{i}}\}$ is the set of (as yet undetermined) mean field parameters which incorporate the effect of particle interactions. It is these parameters which are varied in order to perform the minimisation discussed above. The aim is to derive a discrete DFT model and as such the grand free energy should appear as a function of the set of lattice densities, $\{\rho_{\mathbf{i}}\}$, which can be varied instead of the set $\{\phi_{\mathbf{i}}\}$ to minimise the grand free energy. The density at a particular cell $\rho_{\mathbf{i}}$ is the statistical average of the occupation number of that cell, in the reference system, defined by Eq. (3.21), this is

$$\begin{aligned} \rho_{\mathbf{i}} &= \langle n_{\mathbf{i}} \rangle_0 = \text{Tr} \left(\frac{e^{-\beta(\Phi_0 - \mu N)}}{\Xi_0} n_{\mathbf{i}} \right), \\ &= \frac{1}{\Xi_0} \left[\sum_{n_1=0}^1 e^{-\beta(V_1 + \phi_1 - \mu)n_1} \right] \dots \left[\sum_{n_M=0}^1 e^{-\beta(V_M + \phi_M - \mu)n_M} \right], \\ &= \left[\frac{\sum_{n_1=0}^1 e^{-\beta(V_1 + \phi_1 - \mu)n_1}}{\sum_{n_1=0}^1 e^{-\beta(V_1 + \phi_1 - \mu)n_1}} \right] \dots \left[\frac{\sum_{n_M=0}^1 e^{-\beta(V_M + \phi_M - \mu)n_M}}{\sum_{n_M=0}^1 e^{-\beta(V_M + \phi_M - \mu)n_M}} \right], \\ &= \frac{\sum_{n_{\mathbf{i}}=0}^1 n_{\mathbf{i}} e^{-\beta(V_{\mathbf{i}} + \phi_{\mathbf{i}} - \mu)n_{\mathbf{i}}}}{\sum_{n_{\mathbf{i}}=0}^1 e^{-\beta(V_{\mathbf{i}} + \phi_{\mathbf{i}} - \mu)n_{\mathbf{i}}}} = \frac{e^{-\beta(V_{\mathbf{i}} + \phi_{\mathbf{i}} - \mu)}}{1 + e^{-\beta(V_{\mathbf{i}} + \phi_{\mathbf{i}} - \mu)}}. \end{aligned} \quad (3.22)$$

Note that the above manipulation is only possible due to the local nature of the variational parameters $\{\phi_{\mathbf{i}}\}$ and that a particular choice of $\phi_{\mathbf{i}}$ uniquely determines the density at that point. Also shown in Eq. (3.22) is the grand partition function of the reference state

$$\Xi_0 = \text{Tr} \exp \left(-\beta \sum_{\mathbf{i}=1}^M (V_{\mathbf{i}} + \phi_{\mathbf{i}} - \mu) n_{\mathbf{i}} \right), \quad (3.23)$$

which can then be used with Eq. (3.13) to give the grand free energy of the reference state

$$\Omega_0 = -k_B T \sum_{\mathbf{i}=1}^M \ln[1 + e^{-\beta(V_{\mathbf{i}} + \phi_{\mathbf{i}} - \mu)}]. \quad (3.24)$$

This grand free energy function can then be recast in terms of the lattice densities by inserting the result of Eq. (3.22), rearranged to $1 - \rho_{\mathbf{i}} = (1 + e^{-\beta(V_{\mathbf{i}} + \phi_{\mathbf{i}} - \mu)})^{-1}$, which now

gives the grand free energy as

$$\Omega_0 = k_B T \sum_{\mathbf{i}=1}^M \ln(1 - \rho_{\mathbf{i}}). \quad (3.25)$$

The next steps of the derivation can in part be motivated by a view to rewrite the above in a form akin to that of Eq. (3.8). More importantly though, Eq. (3.25) only depends on the external field, $V_{\mathbf{i}}$, and the variational parameters, $\phi_{\mathbf{i}}$, implicitly through $\rho_{\mathbf{i}}$, this dependence is made explicit. Firstly, Eq. (3.25) is rewritten as

$$\Omega_0 = k_B T \sum_{\mathbf{i}=1}^M [(1 + \rho_{\mathbf{i}} - \rho_{\mathbf{i}}) \ln(1 - \rho_{\mathbf{i}})]. \quad (3.26)$$

Taking the logarithm of the result in Eq. (3.22) gives $\ln(1 - \rho_{\mathbf{i}}) = \ln(\rho_{\mathbf{i}}) + \beta(V_{\mathbf{i}} + \phi_{\mathbf{i}} - \mu)$ which is then used to write Eq. (3.26) as

$$\Omega_0 = k_B T \sum_{\mathbf{i}=1}^M [\rho_{\mathbf{i}} \ln \rho_{\mathbf{i}} + (1 - \rho_{\mathbf{i}}) \ln(1 - \rho_{\mathbf{i}}) + \beta(V_{\mathbf{i}} + \phi_{\mathbf{i}} - \mu)], \quad (3.27)$$

which now has an explicit dependence on $V_{\mathbf{i}}$ and $\phi_{\mathbf{i}}$. Note that for a system in which $V_{\mathbf{i}} = \phi_{\mathbf{i}} = 0$, Eq. (3.27) reduces down to the form initially proposed in Eq. (3.8) since in the absence of an external field $\rho_{\mathbf{i}} = \rho \forall \mathbf{i}$ and recalling that $\Omega = F - \mu N$.

The perturbation to the reference state is defined from Eqs. (3.1) and (3.21):

$$\Delta\Phi = -\frac{1}{2} \sum_{\mathbf{ij}} \epsilon_{\mathbf{ij}} n_{\mathbf{i}} n_{\mathbf{j}} - \sum_{\mathbf{i}=1}^M \phi_{\mathbf{i}} n_{\mathbf{i}}. \quad (3.28)$$

The statistical average of this quantity is required and this is found to be

$$\langle \Delta\Phi \rangle_0 = -\frac{1}{2} \sum_{\mathbf{ij}} \epsilon_{\mathbf{ij}} \rho_{\mathbf{i}} \rho_{\mathbf{j}} - \sum_{\mathbf{i}=1}^M \phi_{\mathbf{i}} \rho_{\mathbf{i}}, \quad (3.29)$$

since $\rho_{\mathbf{i}} = \langle n_{\mathbf{i}} \rangle_0$ and $\langle n_{\mathbf{i}} n_{\mathbf{j}} \rangle_0 = \langle n_{\mathbf{i}} \rangle_0 \langle n_{\mathbf{j}} \rangle_0$ due to the fact that reference system is non-interacting and so the trace can be separated into individual terms in $n_{\mathbf{i}}$ following the procedure in Eq. (3.22). Finally, inserting Eqs. (3.27) and (3.29) into Eq. (3.20), gives the upper bound of the true grand free energy:

$$\begin{aligned} \Omega &\leq \hat{\Omega} = \Omega_0 + \langle \Delta\Phi \rangle_0, \\ &= k_B T \sum_{\mathbf{i}=1}^M [\rho_{\mathbf{i}} \ln \rho_{\mathbf{i}} + (1 - \rho_{\mathbf{i}}) \ln(1 - \rho_{\mathbf{i}})] - \frac{1}{2} \sum_{\mathbf{ij}} \epsilon_{\mathbf{ij}} \rho_{\mathbf{i}} \rho_{\mathbf{j}} + \sum_{\mathbf{i}=1}^M (V_{\mathbf{i}} - \mu) \rho_{\mathbf{i}}. \end{aligned} \quad (3.30)$$

This is now a discrete, mean field DFT, depending implicitly on $\{\phi_{\mathbf{i}}\}$, where since the

variational parameters uniquely determine the density profile $\{\rho_i\}$ (Eq. (3.22)), finding the set $\{\rho_i\}$ which minimises Eq. (3.30) is equivalent to choosing the set $\{\phi_i\}$ which minimises the function. Minimising this function gives a best approximation for the true lattice free energy $\Omega = -k_B T \ln \Xi$ where Ξ is the partition function of the full system defined by Eq. (3.1). For the sake of brevity, throughout the remainder of this chapter the grand free energy in the reference system $\hat{\Omega}$ is referred to simply as the grand free energy and is denoted Ω . It should be remembered that this remains only an approximation to the true lattice free energy.

3.1.2 Defining the Potentials

By specifying the Hamiltonian in Eq. (3.1), all particle interactions above two body (pair) interactions were neglected. The pair interactions are now fully defined as

$$\epsilon_{ij} = \frac{\epsilon}{|\mathbf{i} - \mathbf{j}|^6}, \quad (3.31)$$

which is inspired by the attractive component of the popular Lennard-Jones 12-6 potential and models the attractive dispersion interactions between simple fluids such as Argon [14]. Because of the specification that a lattice site may only be occupied by one particle a hard-core repulsion enters into the grand free energy function in the $\ln(1 - \rho_i)$ term. The lattice fluid itself is now fully defined and could be used to study fluid behaviour in a wide range of confining geometries. In order to calculate the binding potential, only the most simple boundary, that of a semi-infinite, planar wall is required, as shown in Fig. 2.5. The external field arising from such a confinement is

$$V_i = \begin{cases} -\epsilon_w/z^3 & \text{for } z > 0, \\ 0 & \text{for } z \leq 0, \end{cases} \quad (3.32)$$

where ϵ_w governs the strength of the interaction and z is the perpendicular distance from the wall of the particle at i . The interaction of a fluid particle with a single particle in the wall is governed by a similar interaction to that of Eq. (3.31), it is the net interaction of the fluid particle with all of the particles in the wall that brings about the form of Eq. (3.32). Note that for this external field only the dimension that is perpendicular to the wall is important and so a reduction of the effective dimensionality of the model can be undertaken.

Neglecting particle interactions beyond pairs of particles greatly reduces the computational effort required to evaluate the partition function and equivalently the grand free energy function. However, even with only pair interactions it is still very computationally expensive, requiring roughly $M^2/2$ evaluations. Since the strength of pair interactions decays fairly quickly ($\sim r^{-6}$) it seems reasonable to only consider pairs of particles within a certain truncated interaction range $L\sigma$. Later, in §3.4.3, the effect of

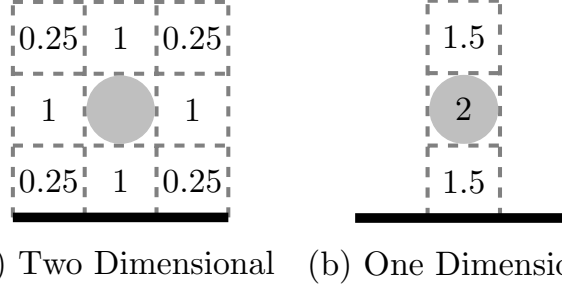


Figure 3.2: An illustration of reducing the dimensionality of the pair interaction terms. Here a reduction is made from a 2D system to an effective 1D one. The 1D interactions are weighted so that the two models coincide and a ‘self’ interaction arises to account for interactions with the fictitious particles the same horizontal distance from the wall as the reference particle.

making this truncation is investigated and it is shown that some care still needs to be taken to ensure that important physical behaviour is not lost.

3.1.3 The Model in Lower Dimensions

Since the LG model is a DFT, formulated in the grand canonical ensemble, the equilibrium density profile matches the symmetry of the external field. The only external field considered here is that of a planar wall and so, as with the FMT model in §2.3.1, the effective dimensionality of the model can be reduced. In this discrete case the particle interactions are summed over any invariant dimensions to give weights for the interactions in the reduced dimension. This is demonstrated in Fig. 3.2 which shows how a 2D system is reduced down to an effective 1D system. Reducing the dimensionality in such a way ensures that results calculated in the full 3D model exactly coincide with those results from an effective 2D or 1D model in the same confining geometry.

Even though throughout this chapter the external field is always a planar wall, where the equilibrium density profile varies in only one dimension, it is still useful to have the 2D reduction of the model. It is shown at a later point how, by fixing the average density in the system, liquid droplet profiles can be found in the effective 2D system. These droplets correspond to ridges in the full 3D system. The 2D interaction weights, truncated to a range of $L\sigma$, are given by

$$\epsilon_{ij} = \begin{cases} \epsilon \left[(i'^2 + j'^2)^{-3} + 2 \sum_{k'=1}^{k' \leq \sqrt{L^2 - i'^2 - j'^2}} (i'^2 + j'^2 + k'^2)^{-3} \right] & \text{for } |\mathbf{i} - \mathbf{j}| \leq L \\ 0 & \text{otherwise.} \end{cases} \quad (3.33)$$

In the above, i' , j' and k' give the separation in the i , j , and k dimensions of a pair of particles at positions \mathbf{i} and \mathbf{j} . The interaction weights for the 1D model can similarly be

calculated.

3.1.4 Bulk Fluid Phase Diagram

The LG model is now fully defined and a particular fluid is fully specified by the choice of β , μ , ϵ and L . The inverse temperature is set to $\beta = 1$ throughout and the chemical potential, unless explicitly stated, is $\mu = \mu_c$, the coexistence value. A particular fluid is then specified by the choice of fluid-fluid interactions strength ϵ and the truncation length of fluid interactions L . The bulk fluid phase diagram can now be calculated which shows the densities at which liquid and gas phases of the fluid can coexist. Recall that liquid-gas coexistence occurs when the pressure p , chemical potential μ and temperature T in each phase are the same. An expression can be found for p and μ in terms of the Helmholtz free energy per unit volume. For a fixed temperature the coexisting liquid and gas densities can be found as the solution to the simultaneous equations

$$\begin{aligned} p(\rho_g) &= p(\rho_l) \\ \mu(\rho_g) &= \mu(\rho_l). \end{aligned} \quad (3.34)$$

For the LG model it is even easier to calculate the phase diagram. The LG model exhibits a ‘hole-particle’ symmetry that leads to the relation $\rho_g = 1 - \rho_l$ and so one can simply solve the single equation

$$p(\rho) = p(1 - \rho), \quad (3.35)$$

to find the coexisting densities.¹ The pressure can be found from Eqs. (2.5) and (2.11) which give $dF = -pdV + \mu dN$, leading to

$$p(\rho) = -\left(\frac{\partial F}{\partial V}\right)_{N,T} = \rho \frac{\partial f}{\partial \rho} - f, \quad (3.36)$$

where $f = F/V$ is the free energy per unit volume. The chemical potential can similarly be found as

$$\mu(\rho) = \left(\frac{\partial F}{\partial N}\right)_{V,T} = \frac{\partial f}{\partial \rho}. \quad (3.37)$$

For the LG model, in the absence of an external field, the free energy per lattice site is

$$\begin{aligned} f &= F/M = k_B T [\rho \ln \rho + (1 - \rho) \ln(1 - \rho)] - \frac{1}{2} \rho^2 \sum_{ij} \epsilon_{ij}, \\ &= k_B T [\rho \ln \rho + (1 - \rho) \ln(1 - \rho)] - \frac{1}{2} \rho^2 \alpha \epsilon, \end{aligned} \quad (3.38)$$

¹This symmetry means that the LG model can also be used to study a two component fluid where $n_i = 0$ if a lattice site is occupied by fluid 1 and $n_i = 1$ for fluid 2. The formulation of the model remains the same.

and $\alpha = \sum \epsilon_{ij}/\epsilon$ is the total integrated range of the particle interactions divided by the energy of the interaction between nearest neighbours. It is the integrated strength, $\alpha\epsilon$, rather than the bare strength parameter ϵ alone that determines the location of the phase boundaries in the phase diagram. In a later section (§3.4.3) the range of particle interactions is truncated to various lengths L , this changes the value of α and so ϵ is adjusted to ensure that the product $\alpha\epsilon$ does not change. By doing this the fluid remains at the same point on the phase diagram and the bulk fluid densities do not change. With this definition for f the pressure is found to be

$$p(\rho) = -k_B T \ln(1 - \rho) - \frac{1}{2} \rho^2 \alpha \epsilon. \quad (3.39)$$

The coexisting densities are then found by solving Eq. (3.35) which yields

$$\frac{k_B T}{\epsilon} = \frac{\alpha(2\rho - 1)}{2[\ln \rho - \ln(1 - \rho)]}. \quad (3.40)$$

This relation maps out the binodal curve which is the locus of coexisting densities of the liquid and gas phases, and is plotted in Fig. 3.3, for the specific case of $\alpha = 5$. The spinodal curve is also shown which plots the point of linear instability of the fluid, i.e. where

$$\frac{\partial^2 f}{\partial \rho^2} = 0, \quad (3.41)$$

leading to

$$\frac{k_B T}{\epsilon} = \alpha \rho (1 - \rho). \quad (3.42)$$

Spontaneous phase separation into the two coexisting densities occurs within the spinodal. Note that, unlike the phase diagram for the continuum fluid in Fig. 2.2, the phase diagram for the lattice fluid is symmetric about $\rho\sigma^3 = 0.5$ which again reflects the hole-particle symmetry of the LG model. As a result of this symmetry the critical temperature must occur at $\rho\sigma^3 = 0.5$ and so the critical temperature is found to be $T = 0.25\alpha\epsilon/k_B$. Above this critical temperature phase separation no longer occurs and only a single phase can be found.

The phase diagram is also shown in the chemical potential-temperature plane in Fig. 3.3b. From Eq. (3.37)

$$\mu(\rho) = \left(\frac{\partial F}{\partial N} \right)_{T,V} = \frac{\partial f}{\partial \rho} = k_B T \ln \left(\frac{\rho}{1 - \rho} \right) - \alpha \epsilon \rho. \quad (3.43)$$

Inserting the result from Eq. (3.40) into this equation gives the chemical potential for liquid-gas coexistence as

$$\mu(\rho) = \mu = -\frac{\alpha\epsilon}{2}. \quad (3.44)$$

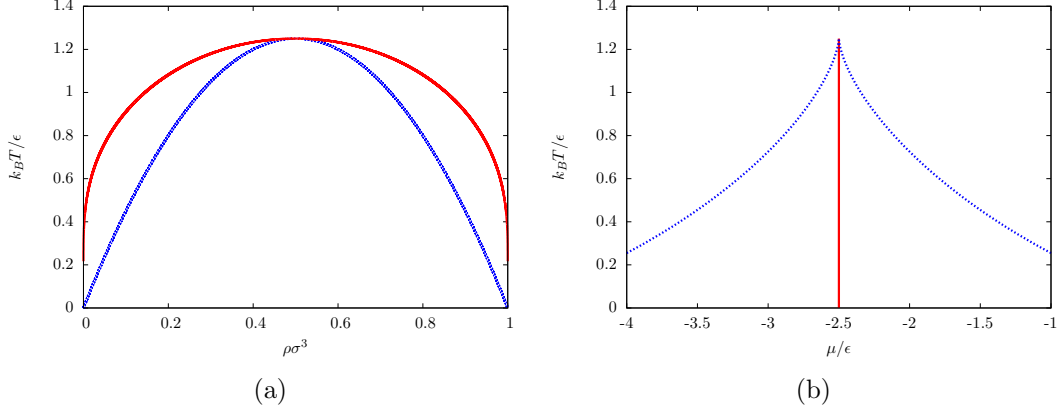


Figure 3.3: Phase diagrams of the lattice fluid for an integrated pair interaction strength $\alpha = 5$: (a) the red curve shows the binodal, the coexisting densities of the liquid and gas phases. The spinodal curve is plotted in blue, spinodal decomposition takes place within this curve. (b) The phase diagram in the chemical potential-temperature plane. The chemical potential of liquid-gas coexistence is always $\mu = -0.5\alpha\epsilon$.

3.2 Solutions to the Model

The set of lattice densities, $\{\rho_i\}$, which minimises the grand free energy function Eq. (3.30), is the equilibrium density profile and give the best approximation of the equilibrium grand free energy. This density profile is found as a solution to the set of coupled equations

$$\frac{\partial \Omega(\{\rho_i\})}{\partial \rho_i} = 0. \quad (3.45)$$

The solution to Eqs. (3.45) is sought numerically via Picard iteration as with the continuum model. Equation (3.30), together with Eq. (3.45) gives

$$\rho_i^{k+1} = (1 - \rho_i^k) \exp \left[\beta \left(\mu + \sum_{ij} \epsilon_{ij} \rho_j - V_i \right) \right], \quad (3.46)$$

where the density profile of the k^{th} iteration is used to find the density profile of the $(k + 1)^{\text{th}}$ iteration. The iteration continues until a suitable convergence criterion is satisfied. The criterion used here is that the density profile calculated at the $(k + 1)^{\text{th}}$ does not differ significantly from the density profile at the k^{th} iteration, i.e. the solution is at a stationary point. This difference between two density profiles, δ , is measured as the sum of the absolute value of the difference between each lattice site in the two profiles:

$$\delta = \sum_{i=1}^M |\rho_i^{k+1} - \rho_i^k|. \quad (3.47)$$

The convergence criterion is satisfied when δ is less than some specified value. In these calculations convergence is achieved when $\delta < 10^{-7}$. As discussed below, the system is made sufficiently large so that there are no errors induced by the constraint of system size.

An initial density profile must be supplied as a starting point for the routine, the better this approximation, the faster the method converges. Often, as is shown in § 3.3 there is a previously calculated state point that can be used as an initial approximation. A mixing procedure must also be applied when solving this discrete model as, if $0 \leq \rho \leq 1$ then the grand free energy, Eq (3.30), becomes undefined. Here, at each iterative step, the mixing procedure

$$\rho_i^{\text{new}} = \alpha \rho_i^{k+1} + (1 - \alpha) \rho_i^k, \quad (3.48)$$

is used. Even when a very small step size is chosen ($\alpha = 0.001$) this method still converges within a satisfactory amount of time so there is no need to employ the adaptive step size method here that is discussed in §2.3 and Ref. [34].

In the continuum model it is very advantageous to enforce periodic boundary conditions on the system so that convolutions can be performed in Fourier space. There is no such advantage in the LG model and so periodic boundary conditions are not necessary. If the interaction range of a particle in the system extends beyond the system boundary then it can be modelled as interacting with some fictitious lattice site of an assumed density. Usually it is assumed that the fluid is at the bulk density beyond the edge of the domain, the frequent exception is if the interaction would be with a particle inside a solid boundary, the confining wall say, in this case the assumed density is set to zero. In this manner particle interactions of any truncation range can be accommodated as long as the system is large enough that the fluid has reached its bulk value by the time the edge of the domain is reached. For the work presented in this chapter a system extending 100 lattice sites from a confining wall is sufficiently large. Solutions from systems larger than this have been calculated and shown to no appreciably change the results.

3.3 Adsorption Isotherms

In §2.4, wetting was described as the adsorption diverging as the chemical potential value at liquid gas coexistence is approached. This phenomenon is now demonstrated with the LG model. For a chemical potential below that of liquid-gas coexistence (i.e. $\mu < \mu_c$ so a low density gas is the preferred phase) the fluid adsorption is small and finite. As the chemical potential is increased towards $\mu = \mu_c$, the adsorption slowly increases. For a temperature below the wetting temperature ($T < T_w$), as $\mu \rightarrow \mu_c^-$ then the adsorption remains small and finite. For a temperature above the wetting temperature ($T > T_w$) then $\Gamma \rightarrow \infty$ as $\mu \rightarrow \mu_c^-$, corresponding to a macroscopically thick liquid film [4]. All of this behaviour is observed in Fig. 3.4 which was calculated from the LG model. For this

discrete model the adsorption is now defined

$$\Gamma = \sum_{\mathbf{i}=1}^M \frac{(\rho_{\mathbf{i}} - \rho_b)}{A}. \quad (3.49)$$

The adsorption is calculated in reference to a bulk density, if a similar procedure is carried out for $\mu > \mu_c$ then the bulk density would be the liquid density and now drying (rather than wetting) would be characterised by $\Gamma \rightarrow -\infty$ as $\mu \rightarrow \mu_c^+$. The isotherms displayed are calculated by fixing a particular fluid (the choice of ϵ and L), and a particular substrate (the choice of ϵ_w), and then calculating the equilibrium density profile for a particular value of $\mu < \mu_{coex}$. Fixing ϵ is equivalent to setting a specific temperature and so these adsorption curves are called ‘isotherms’. The adsorption can then be calculated from the equilibrium density profile via Eq. (3.49). This process is then repeated with an incremented value of μ , steadily increasing the chemical potential, calculating Γ at each point, until $\mu = \mu_{coex}$. The resulting data is then plotted as seen in Fig. 3.4. Each choice of μ and ϵ defines a particular state point. For a fixed ϵ , when seeking the equilibrium density profile for a state point defined by $\mu + \Delta\mu$, if the equilibrium density profile for the state point defined by μ is known, then this can be used as the initial condition of the numerical minimisation. The μ state point can be very close to the $\mu + \Delta\mu$ state point and so the equilibrium density profile is found very quickly. In Fig. 3.4 the attractive strength of the wall ϵ_w , not the fluid-fluid interaction strength ϵ , is varied. Increasing ϵ_w has a similar effect to raising the temperature (or decreasing ϵ). In several of the curves the discontinuous jump from crossing the pre-wetting line is observed [4]. The isotherm for $\beta\epsilon_w = 1.2$ clearly shows the fluid crossing the pre-wetting line and discontinuously jumping to a higher density. For an even more strongly attracting wall, $\beta\epsilon_w = 2.3$ say, this transition has become continuous corresponding to the fluid no longer crossing this pre-wetting line. One can observe the size of the jump getting smaller through the $\beta\epsilon_w = 1.2$ and $\beta\epsilon_w = 1.3$ curves before becoming smooth for $\beta\epsilon_w = 1.7$. After the initial discontinuous jump from crossing the pre-wetting line, similar smaller jumps in the adsorption can be observed. These smaller discontinuities are ‘layering transitions’ which result from particles packing in layers against the substrate, increasing the adsorption discontinuously as another layer is added. Because of the discrete nature of the LG model, these layering transitions are strongly amplified although are still possible to observe in continuous models, see e.g. Ref. [47].

A simple Picard iteration scheme easily finds minima of the grand free energy function as these are stable stationary points. This method can not find the unstable maxima (and saddles). By using more sophisticated numerical techniques, any stationary point can be found and the full evolution of a stationary point with respect to a particular parameter can be followed. The continuation software ‘AUTO’ is used to follow the stationary points of a 1D lattice of size $M = 40$. The fluid-fluid particle interactions are reduced

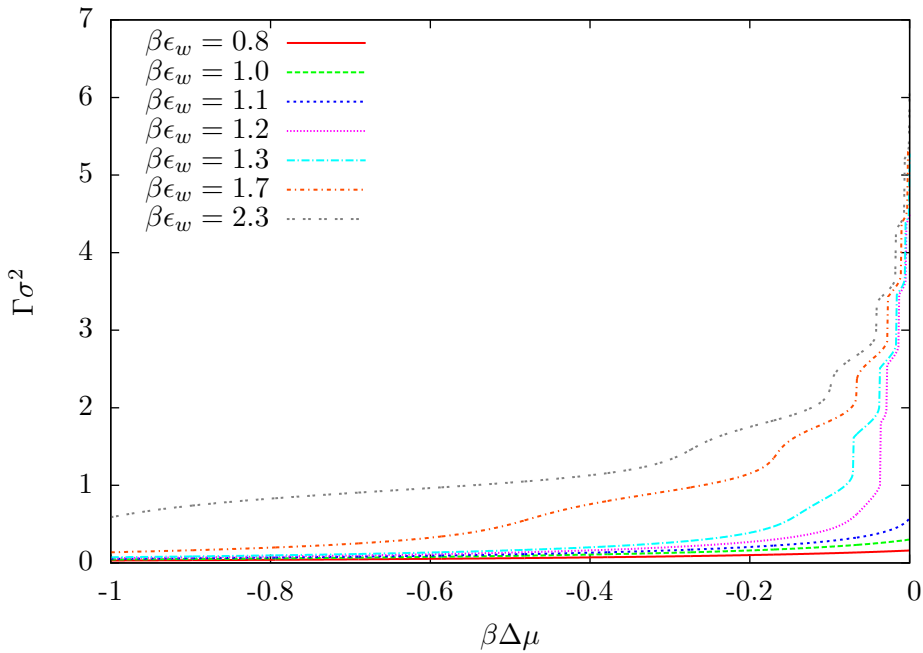


Figure 3.4: Isotherms of the adsorption of a fluid as the chemical potential approaches that of liquid-gas coexistence. The interaction strength (temperature) is fixed at $\beta\epsilon = 1$ and the strength of the wall-fluid interactions is varied. For weakly attractive walls, the fluid is non wetting and the adsorption remains small and finite. For stronger attractions the adsorption diverges as coexistence is approached. A fluid crossing the pre-wetting line can be observed as a discontinuous jump to higher densities in some isotherms. Subsequent jumps are then layering transitions. For more attractive substrates the discontinuity smooths out and the pre-wetting line is no longer crossed.

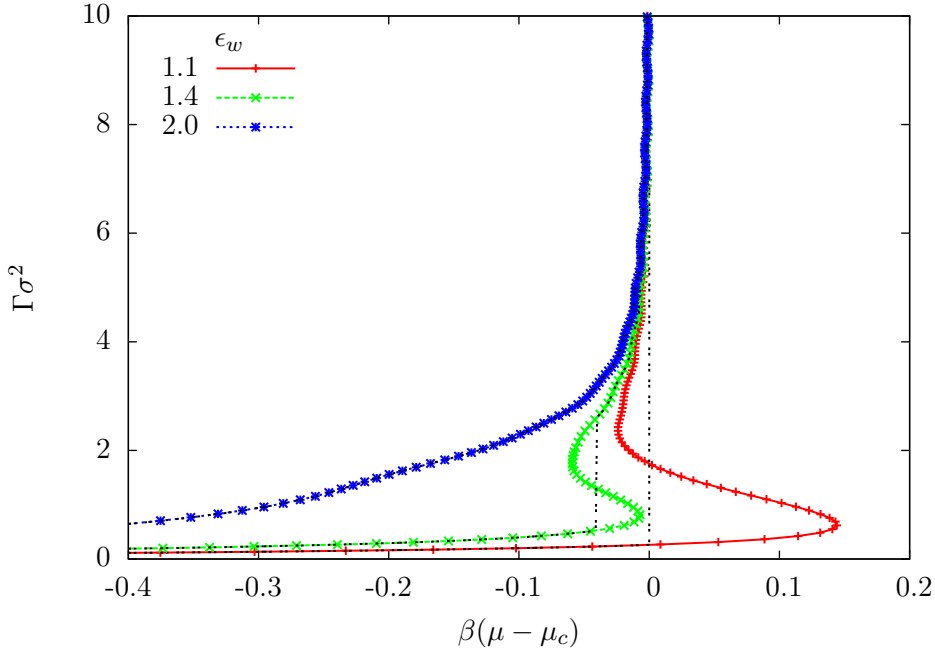


Figure 3.5: Adsorption isotherms calculated via continuation techniques, even unstable stationary points are found using these methods. Note that the model used here has only short ranged interactions up to the nearest neighbour lattice sites, as described in Ref. [18]. The black lines show the isotherms as calculated by solving the LG model with a Picard iteration method where only the stable fixed points are found.

to only up to the next-nearest neighbour interactions, using the pair potential described in Appendix A and Ref. [18]. The adsorption is then calculated for these stationary points and this is plotted against the chemical potential as shown in Fig. 3.5. The isotherms found from the Picard iteration scheme are shown overlaying these results and then jumps in the adsorption from crossing the pre-wetting line can be identified as switching from one branch of solution to the next. This simpler, shorter ranged pair potential is used with the continuation method of finding the equilibrium density profile as for larger systems, particularly with longer fluid-fluid interaction ranges, the equations quickly become unwieldy and harder to work with so this method is only used for this small, short ranged example given here. In Fig. 3.6 a single isotherm is plotted with both continuation techniques (green curve) and the LG model (red curve). On the same figure the free energy of the system (blue curve, right axis) is also plotted with the aid of continuation techniques. The Picard iteration results show that the solution branch corresponding to the least free energy is always found. The pre-wetting jump occurs exactly at the point where the free energies of the two solution branches cross. The pre-wetting line terminates where there is only one possible solution branch, this is the point where the two fold bifurcations seen in the continuation results coalesce.

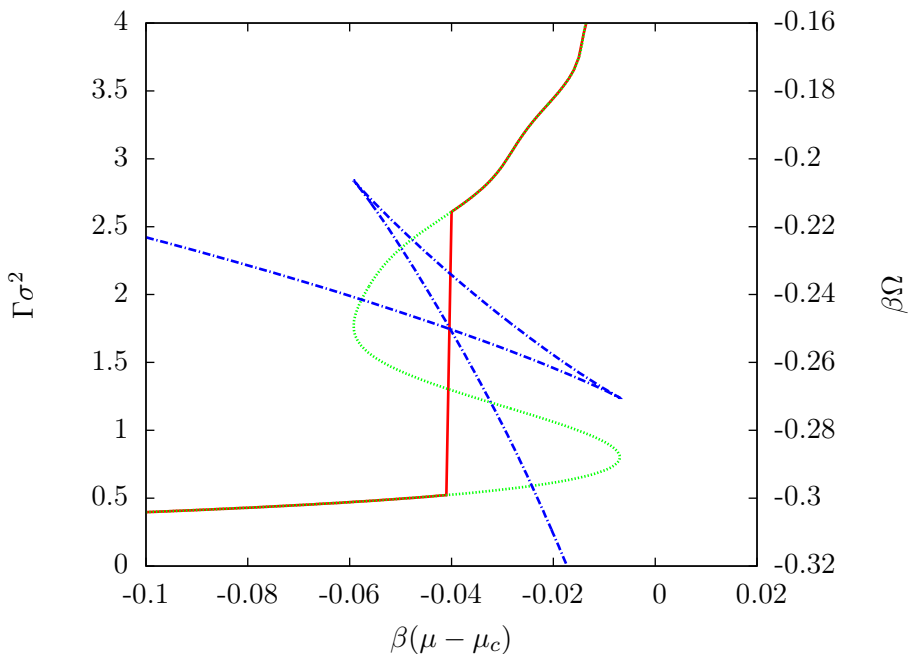


Figure 3.6: The jump of crossing the pre-wetting line occurs as a result of switch from one solution branch to the other, the point of least free energy is always found. The red curve is the adsorption isotherm calculated by minimising the free energy via Picard iteration, the green curve is the adsorption isotherm found by following all stationary points including the unstable ones. The blue curve shows the free energy calculated for each point on the green curve.

3.4 Calculating the Binding Potential

The binding potential was defined via Eq. (2.73) as the free energy per unit area that arises from the interaction between the wall-liquid and liquid-gas interfaces. A method is now outlined by which the binding potential may be fully calculated from the LG model or any other DFT model. This method correctly calculates the small Γ behaviour of the binding potential which is missed in the usual asymptotic results such as Eq. (1.4). Using only the asymptotic results for the binding potential works well for larger drops, however, as the microscopic regime is approached the results become unacceptable. If the full binding potential is used as input to the IH model, droplets should be calculated that are of the same shape as those calculated from a purely microscopic method such as DFT.

The binding potentials are calculated in a similar way to how the adsorption isotherms were found in § 3.3, however now it is the adsorption Γ , not the chemical potential which is the important variable. The problem is that while μ is a natural parameter to be varied, the adsorption is usually an output quantity, calculated from the equilibrium density profile. However, by using a method which is introduced shortly, the adsorption of a system can be constrained and used as an input parameter. With Γ now a control parameter, the binding potential can be calculated: For a particular choice of ϵ and L , with $\mu = \mu_c$, the equilibrium density profile, constrained to have the desired adsorption, is found. From this density profile the grand potential of the system can be calculated, the value of the binding potential at that particular adsorption is found from this via a rearrangement of Eq. (2.73):

$$g(\Gamma) = \frac{\Omega - \Omega_b}{A} - \gamma_{lg} - \gamma_{wl}, \quad (3.50)$$

where the binding potential is given as a function of Γ . The desired adsorption can then be incremented slightly and, using the previous state point (where a state point is now defined by the choice of Γ) as an initial approximation, the new constrained equilibrium density profile for the incremented adsorption constraint can be found. This method of incrementing the adsorption, recalculating the profile and then finding the next value of the binding potential is repeated over the desired adsorption range. Examples of the binding potentials found using this method are displayed in Fig. 3.7.

From this series of points it is necessary to give an algebraic form of the binding potential so it can be used as input to larger scale models such as the IH model. To find an algebraic form of the binding potential the data points calculated using the above method must be fitted to some appropriate ‘fit function’. The particular form of the fit function proposed here is

$$g_f(\Gamma) = \frac{A(\exp(-P(\Gamma)) - 1)}{\Gamma^2}, \quad (3.51)$$

where

$$P(\Gamma) = a_0\Gamma^2 e^{-a_1\Gamma^2} + a_2\Gamma^2 + a_3\Gamma^3 + a_4\Gamma^4 + a_5\Gamma^5 + a_6\Gamma^6, \quad (3.52)$$

and A , a_0 , a_1 , a_2, \dots are parameters to be fitted. The motivation behind the choice of this fit function is as follows: at large adsorptions $g_f(\Gamma)$ reproduces the behaviour of the asymptotic result and decays $\sim \Gamma^{-2}$ for $\Gamma \rightarrow \infty$. This asymptotic behaviour also requires that the coefficient of the highest order Γ term (a_6 in Eq. (3.52)) is positive. For small x , $\exp(x) \approx 1 + x$, and so at small adsorption g_f behaves like $-P(\Gamma)$. The choice of the second exponential term in (3.52) is motivated by the asymmetric form of the low adsorption minima of the binding potentials, as seen in Fig. 3.7. The parameter A fixes the $\sim \Gamma^{-2}$ decay rate of the binding potential and this can either be fitted from existing data or calculated directly as is shown in §3.4.1. The quality of Eq. (3.51) as a fit function can be observed in Fig. 3.9 where a comparison of the fit function is shown against the result calculated directly from the model.

From the inset of Fig. 3.7 the long ranged $\sim \Gamma^{-2}$ decay is seen, the straight black line in this inset is $0.07\Gamma^{-2}$ which is included to illustrate the decay rate. It is shown in the following section how this decay rate may be calculated analytically using the sharp kink approximation. The inset of Fig. 3.7 also shows the occurrence of oscillations in the tails of binding potentials. A zoom of the tail of a binding potential can also be seen in both Figs. 3.9 and 3.10 which highlights these oscillations. In the following chapter it is discussed how such oscillations can occur naturally as a result of physical considerations. However, the oscillations here, which do not decay with Γ , are an artefact of the discrete nature of the lattice model. These oscillations occur as a result of forcing a particular adsorption on the system. If the equilibrium density is found for a particular film thickness, the natural way to increase the thickness of the film is to add an additional layer of fluid particles. This increases the adsorption by approximately $\sigma(\rho_l - \rho_g)$. The increments of Γ are much smaller than this; the only way for the film to increase by this small increment is to either shift the entire density of the liquid film or to deform the interfaces. Whichever option is selected, the free energy of that film must be increased. The oscillations in the tails of the binding potential are the result of this raising of the free energy. The deformation of the liquid-gas interface is demonstrated in Fig. 3.8 where the two red curves show density profiles that correspond to local minima in the tails of the binding potentials. The other non-optimum density profiles have a different structure of the liquid-gas interface. As well as a deformed interface these profiles also settle to a different liquid density. The gas density for all of the curves is the same.

3.4.1 The Sharp-Kink Approximation

The large Γ decay rate can be directly calculated by making the sharp-kink (SK) approximation. The SK approximation neglects the shape of the interface between different phases in a fluid and instead assumes that the density profile transitions discontinuously,

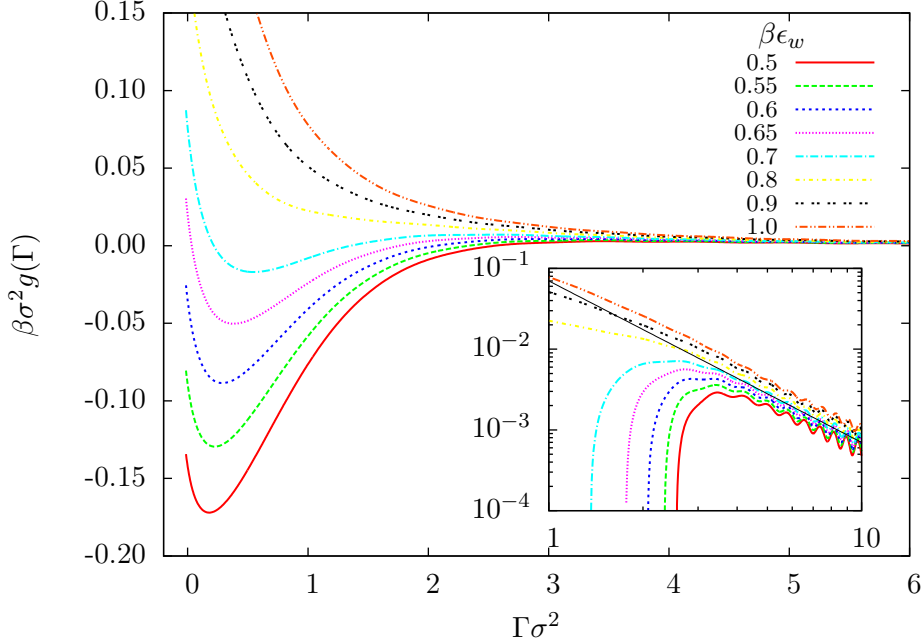


Figure 3.7: A set of binding potentials calculated via the LG model with $\beta\epsilon = 0.9$. For a weakly attracting substrate the global minimum of this potential is at a very low adsorption and corresponds to a state of non-wetting. For more attractive substrates wetting occurs and the global minimum is found as $\Gamma \rightarrow \infty$. The low adsorption minima have an asymmetric shape, increasing much more sharply to the left of the minimum than to the right. The inset shows the same curves on a log-log scale where the decay rate can be observed. The solid black line in this inset is $0.07\Gamma^{-2}$. Oscillations in the tails of the binding potentials can also be observed in the figure inset.

as a step function, from the density of one phase to that of another. It is a useful tool to study the energy of films of various thicknesses and for suitably thick films gives a reasonable estimate of the free energy of the film. For thinner films however, the shape of the interfaces becomes more important and the SK approximation is not so reliable. The SK approximation for the 1D LG model assumes a density profile of the form

$$\rho_z = \begin{cases} \rho_l & \text{for } z < h, \\ \rho_g & \text{for } z > h, \\ 0 & \text{otherwise,} \end{cases} \quad (3.53)$$

where z is the number of lattice sites away from a substrate and $h\sigma$ is the thickness of the liquid film. The free energy of such a film can then readily be calculated via Eq. (3.30). Since the grand free energy can be calculated for a liquid film of any given height h then the binding potential can be analytically calculated. The binding potential for a fluid with a full ranged external potential, but fluid-fluid interactions truncated to a range L ,

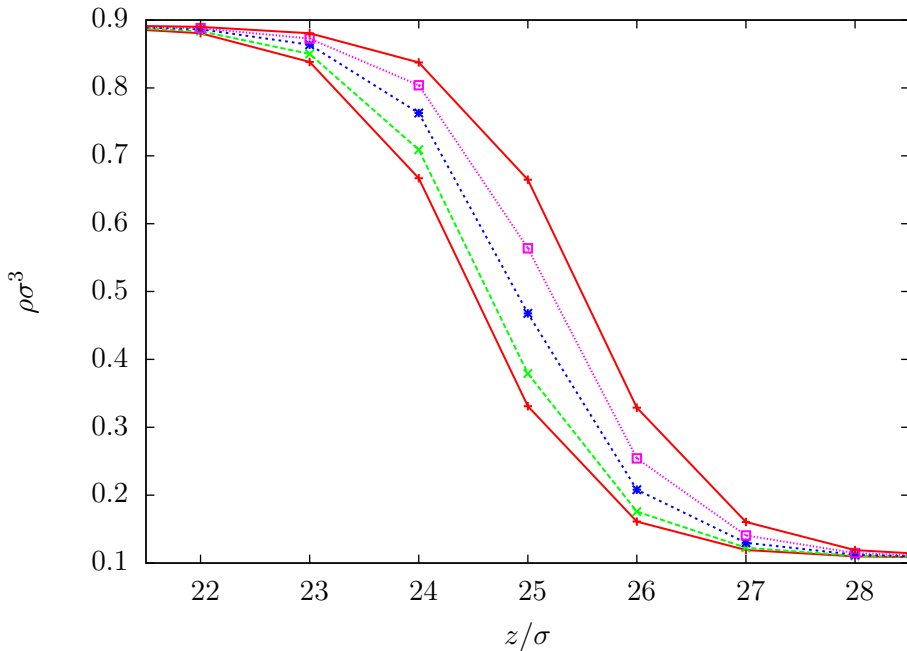


Figure 3.8: The deformation of the interface as a result of the discrete nature of the LG model. The red curves show density profiles corresponding to two local minima of the oscillations of the tails of the binding potentials. The other curves show the density profiles for non optimal points of the oscillatory tails. The deformation of the interface can be observed in the non-optimum curves compared to the two red curves which are essentially the same interface translated along by one lattice spacing.

is, for film heights $h > L$,

$$g_{sk}(h) = (\rho_l - \rho_g)\sigma^3 \sum_{i=h+1}^{\infty} V_i. \quad (3.54)$$

Making an asymptotic expansion of the summation and truncating after the first term gives

$$g_{sk}(h) \approx \frac{\epsilon_w \pi (\rho_l - \rho_g) \sigma^3}{12h^2} \approx \frac{\epsilon_w \pi (\rho_l - \rho_g)^3 \sigma^3}{12\Gamma^2}. \quad (3.55)$$

This result can then be used to find the parameter A in Eq. (3.51). This calculation has also shown that the Γ^{-2} decay is not an arbitrary choice but occurs naturally as a result of the form of the particle interactions. If the fluid-fluid interactions are also not truncated then g_{sk} contains a term in ϵ that also decays as h^{-2} . The SK results are plotted against the full LG data in Fig. 3.9 on a log scale where the equivalent decay rates are apparent. The SK results do not exhibit the oscillatory decay of the full LG results as there is no interface to be deformed. The comparison of the SK binding potential with the one from the full model show that the SK binding potential passes through the middle of the oscillations of the LG model. It does not simply pick out the minima of the oscillations as one might expect. This suggests that the SK approximation slightly overestimates the binding potential compared to the LG model but this is only noticeable on this logarithmic scale. This discrepancy is likely due to making the asymptotic expansion when calculating the SK result, this treats the system in more of a continuum manner than it is in reality. The LG is in effect just a crude numerical integration.

3.4.2 Fixing the Adsorption

In order to constrain a particular adsorption, a procedure first outlined by Archer and Evans [48] is implemented. At each step in the Picard iteration scheme the density profile must be updated as

$$\rho_i^{\text{new}} = (\rho_i^{\text{old}} - \rho_b) \frac{\Gamma_d}{\Gamma} + \rho_b, \quad (3.56)$$

where Γ is the adsorption of the density profile $\{\rho_i^{\text{old}}\}$ and Γ_d is the desired adsorption of the final profile. The algorithm for finding the equilibrium density profile is given by Algorithm 3.1. Constraining the adsorption is equivalent to adding a fictitious external potential to the system that stabilises a film of a desired height, h , (or equivalently an adsorption Γ). This fictitious potential decays to zero at distances far from the wall and although it is not known a-priori it can be calculated on the fly during the minimisation procedure. A selection of density profiles constrained to various values of Γ and the fictitious potentials required to stabilise these profiles are displayed in Fig. 3.10. This figure also shows a binding potential curve (a) marked with coloured points each of which correspond to a density profile (b) at various constrained adsorptions. The effective

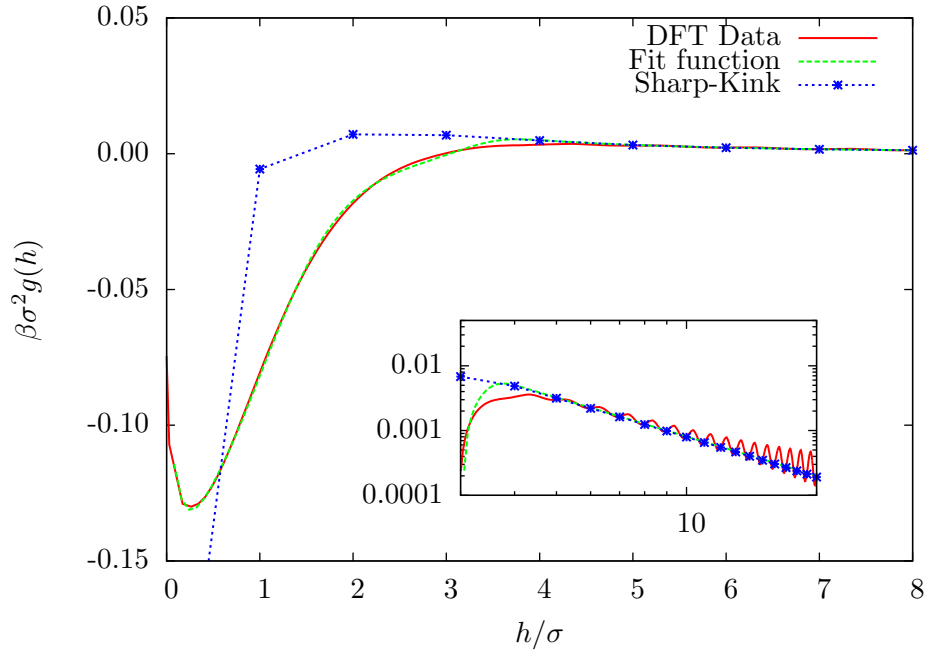


Figure 3.9: The sharp-kink results together with the full DFT results and the fit function Eq. (3.51). The sharp kink results match the decay rate of the DFT data as expected but they can not describe the small Γ behaviour of the binding potential. It is only the DFT results that exhibit the erroneous oscillations, both the fit function and sharp-kink results do not suffer from this discretisation problem.

Algorithm 3.1 The Picard iteration scheme to numerically solve the Euler-Lagrange equation to find the equilibrium density profile. A mixing step is included to ensure that the solution does not break down. Step 3 is an optional step by which the average density can be constrained.

- 1: Set initial density profile
 - 2: Compute new density profile
 - 3: Constrain the density if desired
 - 4: Mix with previous solution
 - 5: Check convergence of solutions
 - 6: **if** Solution has converged **then**
 - 7: End
 - 8: **else**
 - 9: Goto line 2
 - 10: **end if**
-

potentials (c) that arise from the density constraint can also be matched up with these profiles. For the density profile that corresponds to the point almost exactly at the minimum of the binding potential (green crosses), the fictitious potential is very small and does not deviate too far from zero. To force an adsorption below the equilibrium value (red crosses) a repulsive fictitious field is required whereas attractive fictitious fields are required to stabilise density profiles with larger than equilibrium adsorptions (violet squares, say). The tail of the binding potential is shown in (d) where the oscillatory structure of the binding potential can be observed, again, this figure is marked with a series of coloured points which relate to fictitious potentials (e). The fictitious potential required to stabilise a particular adsorption depends on where the adsorption value lies in relation to one of the local stationary points of the oscillations. The closer the adsorption is to a local minima or maxima, the smaller the magnitude of the fictitious potential and the larger the adsorption the longer the non-zero part of this fictitious potential extends for. For any constrained adsorption, only a very small fictitious potentials is required to stabilise it.

This particular method of fixing the adsorption is necessary as it forces the density profile into two distinct phases by only adjusting the density of areas not at the bulk gas density. An alternative method replaces Eq. (3.56)

$$\rho_i^{\text{new}} = \rho_i^{\text{old}} \frac{\Gamma_d}{\Gamma}, \quad (3.57)$$

which adjusts the density uniformly across the system and is equivalent to a shift in the chemical potential in the system. This second method is not suitable as for average densities that lie outside of the spinodal, the bulk density is uniformly raised instead of separating into two phases. The density profile of a uniformly raised average density is actually the lower energy configuration and therefore more a true equilibrium than the higher energy case found by forcing the fluid into two separate phases. Uniformly raising the density like this has an energetic cost as the fluid is not at the density of the energetic minimum. However, the energetic cost of raising the density is not as high as the cost of the formation of a liquid-gas interface. The further this uniform density is away from the equilibrium density, the higher the cost, when the cost of this uniform film is greater than the cost of forming the interface, the fluid phase separates. The density at which this occurs is given by the spinodal.

The binding potential is a function of the film thickness, h , and this is related to the adsorption $\Gamma \approx h(\rho_l - \rho_g)$. This relation assumes that the fluid is in two distinct phases, if the density of the fluid over the entire system is uniformly raised instead then this relation no longer holds. By raising the density uniformly, the value of the fluid density in the bulk has been changed. This is a change in the state point of the fluid. An additional problem with using Eq. (3.57) to fix a film height is that for smaller film heights this corresponds to a large shift in the chemical potential, taking the system far

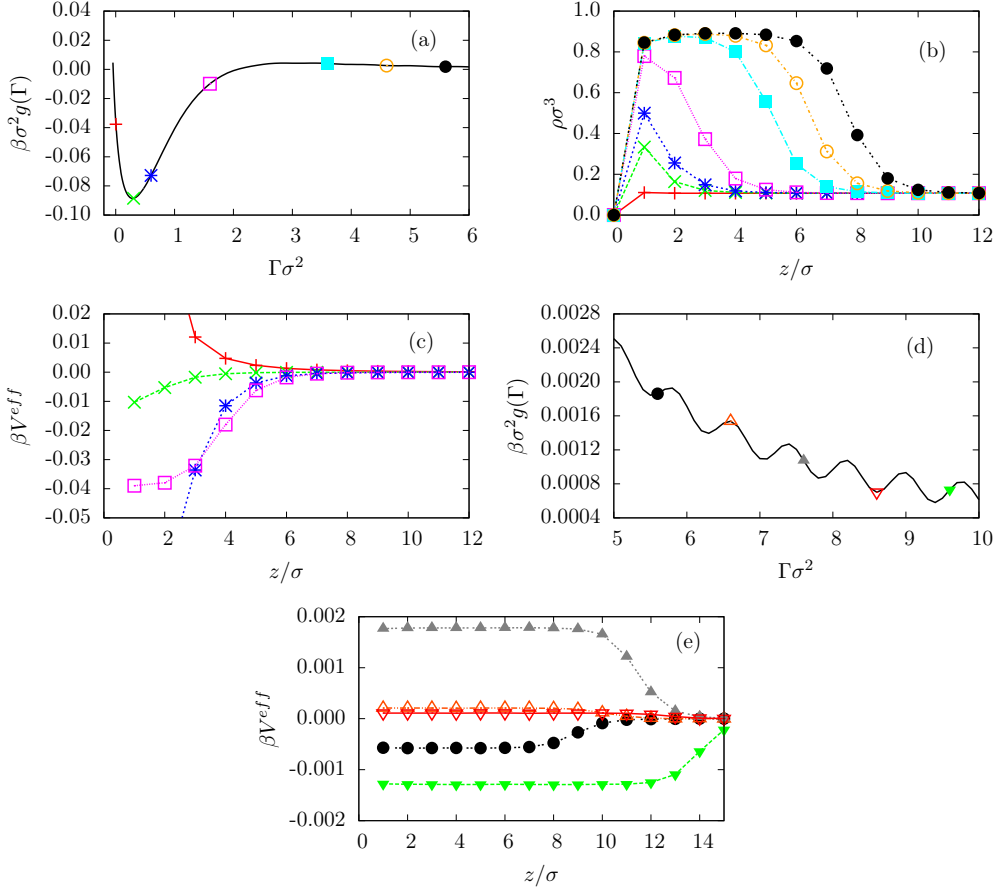


Figure 3.10: In (a) the binding potential $g(\Gamma)$ for a fluid with bulk gas density $\rho\sigma^3 = 0.107$ and temperature $\beta\epsilon = 0.9$ against a planar wall with attraction strength $\beta\epsilon_w = 0.6$ is displayed. A magnification of the tail of $g(\Gamma)$, for larger values of the adsorption Γ is shown in (d). Marked on $g(\Gamma)$ are points that correspond to the density profiles displayed in (b), and the corresponding fictitious potentials V_i^{eff} , which are displayed in (c) and (e). The marked points have adsorption values: $\Gamma\sigma^2 = 0.004, 0.304, 0.6, 1.6, 3.6, 4.6, 5.6, 6.6, 7.6, 8.6, 9.6$ (note that the density profiles for the final four values are not displayed in (a) and (b), for clarity). The fictitious potential is that which must be applied to stabilise a film of liquid with the given adsorption in an open (grand-canonical) system.

from the point of liquid gas coexistence.

3.4.3 The Range of Pair Interactions

In §3.1.2 the pair interactions were defined along with a range L beyond which pair interactions were truncated. Other models, such as molecular dynamics simulations, also frequently rely on truncated pair interactions for computational efficiency [17, 49, 50]. Even though the individual potential contribution from the interaction of a single pair of well separated particles is very small, the net contribution can be significant. Binding potentials are now used to explore these truncation effects. Recall that it is the combination of ϵ and L together that determines the position of the fluid on the phase diagram. In the following investigation into truncation effects ϵ is adjusted alongside L so that for any value of L , the fluid's position in the phase diagram does not change. All of the results presented here for different ranges of pair interaction have the same bulk liquid and gas densities. When a value of ϵ is quoted it corresponds to the value of ϵ at a reference range $L = \sigma$, i.e. interactions only with the nearest neighbour lattice sites. In §3.1.4 a parameter α was defined as the integrated range of particle interactions, for this range of $L = 1\sigma$, $\alpha = 6$ for the 3D system. The actual ϵ is then given by

$$\epsilon = \frac{\alpha_r \epsilon_r}{\alpha}, \quad (3.58)$$

where α_r and ϵ_r are the reference values.

If all interactions are truncated, including the interaction with the external field, then one observes a change in the rate at which the binding potential decays to zero as shown in Fig. 3.11. The change in decay rate can not be clearly seen from the main figure however the inset, which shows the same data on a logarithmic scale, is very clear. As the truncation range L is decreased (the interactions become shorter ranged) the decay rate switches from an algebraic decay ($g \sim \Gamma^{-2}$) to an exponential one. If only the fluid-fluid pair interactions are truncated, as in Fig. 3.12, then as can be seen from the inset of this figure, the decay rate does not change. What is particularly interesting about Fig. 3.12 is how the minima for small Γ change with L , as L is increased (longer ranged interactions) the value of the minimum decreases. In particular, between the ranges of $L = 2$ and $L = 3$ the minimum decreases sufficiently to become the global minimum whereas before it was only a local one. This decrease of the minimum is indicative of the fluid becoming less wetting. When the minimum decreases to such an extent that it becomes a global minimum then the phase behaviour of the fluid has changed from wetting to non-wetting. Obviously the particular choice of parameters here ($\beta\epsilon = 0.8$ and $\beta\epsilon_w = 0.5$) was made so as to highlight this shift in phase behaviour and there exists a great range of parameter choices for which a shift in phase behaviour would not be seen, although the fluid always becomes less wetting. The truncation range L is an important consideration, particularly for state points close to a wetting transition, the

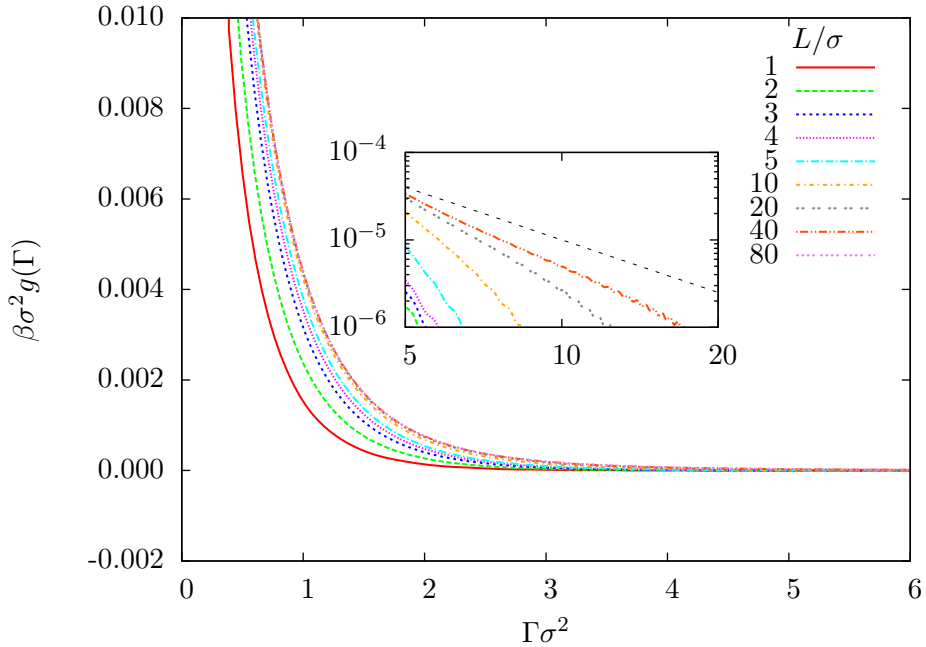


Figure 3.11: The change in the rate at which the binding potential decays to zero according to the range at which interactions are truncated. All interactions including those in the external field are truncated. As the truncation range L is decreased the decay switches from algebraic to exponential. The fluid state point is defined by $\beta\epsilon = 0.9$ with an external field with attractive strength parameter $\beta\epsilon_w = 0.7$.

particle interaction ranges must be long enough to correctly capture the phase behaviour. While it is true that a fluid with long ranged interactions would be less wetting than a short ranged fluid that is otherwise identical, the purpose of this discussion is to highlight the effects of choices made in the mathematical modelling of the fluid. The decision to truncate particle interactions is usually made to increase computational efficiency and not to better capture physical behaviour. It is not always safe to assume that the tails of the long-ranged interactions can be truncated even though they have only a small potential energy contribution, the net effect can be very significant.

3.5 Liquid Droplets and the Interface Hamiltonian Model

Constraints on the average density are not only used to calculate the binding potential but also to find droplet profiles. At first the idea of finding a droplet as an equilibrium solution may appear to contradict the previous assertion that the density profile follows the symmetry of the external field. Clearly, a droplet on a planar substrate in the 2D model (a 3D ridge) varies in two dimensions, not the one dimension predicted by considering the symmetry of the external field of the planar wall. However, averaging over all possible positions of the droplet on the substrate, all of which are energetically

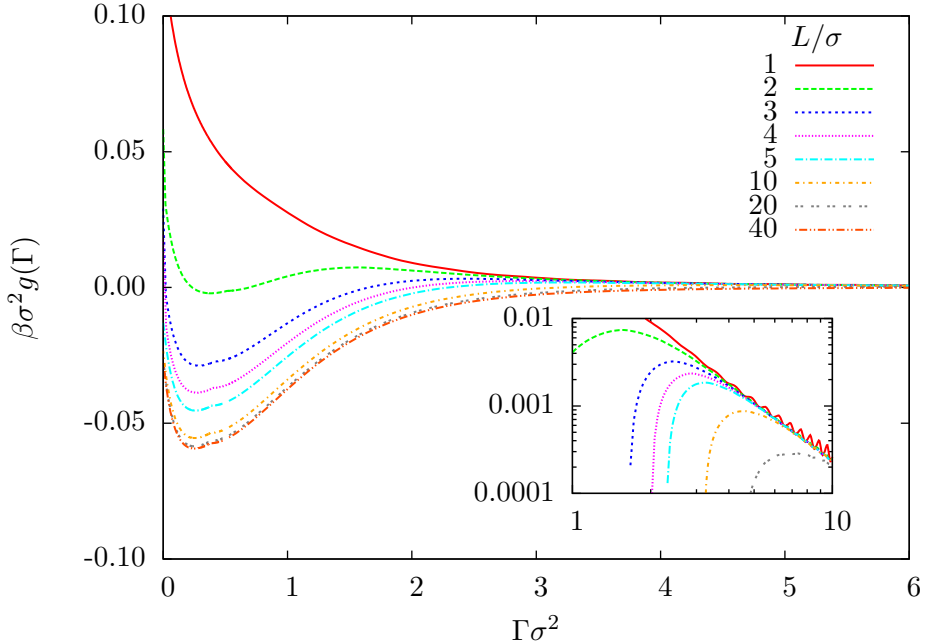


Figure 3.12: Binding potentials calculated for a variety of different pair interaction truncation ranges L . A shift in phase behaviour from wetting to non-wetting is observed as L is increased. The state point of the fluid is set by $\beta\epsilon = 0.8$ and the wall exerts an attraction governed by $\beta\epsilon_w = 0.5$.

equivalent, would result in a density profile varying only in one dimension. Thus, a droplet from the statistical mechanics point of view is a state where the centre of mass is constrained to a certain point along the surface. An example of droplet profiles on substrates of varying attractive strength are displayed in Fig. 3.13. The figure shows a series of droplet profiles on a planar wall each with the walls being increasingly attractive. The droplets spread out as ϵ_w increases and eventually form a wetting film. Looking closely at the profiles there is a very thin precursor film adhering to the substrate across the whole width of the domain. The height of this film is given by the height at which the minimum of the binding potential occurs. To call such an area of raised density a ‘film’ could be argued to be misleading as the thickness of this film is less than a single fluid particle so it is really just a few particles adsorbed ‘here and there’ to the substrate.

A liquid droplet calculated via the DFT model should coincide with the result of a liquid droplet calculated from the IH model given by Eq. (1.2). The droplet profiles found via the IH model are film height profiles, where the height of the liquid film is given as a function of its position on the interface. The density profiles that are found directly from the DFT model must be coarse-grained down to a similar form in order to make a comparison. The exact form of such a reduction depends upon how the liquid film height is defined. The height of the liquid film could be defined as the contour of the point half-way between the liquid and gas densities, $\rho = 0.5$ for the LG model, this

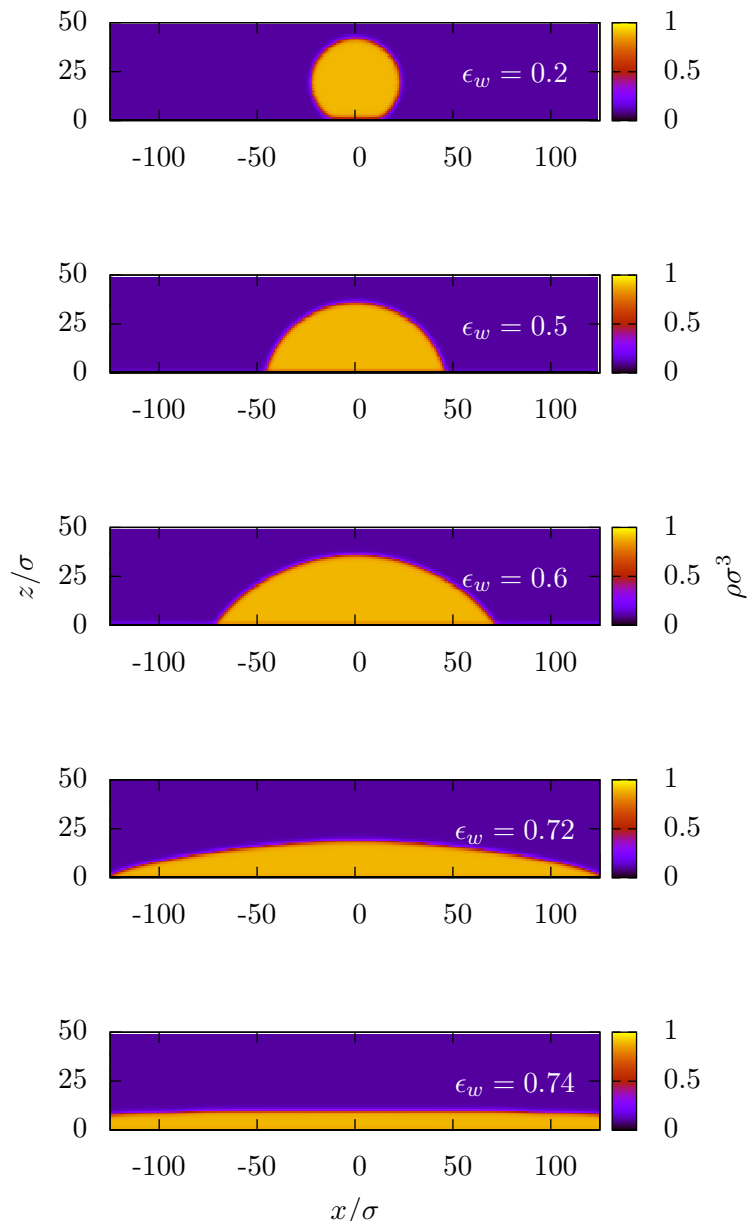


Figure 3.13: Two dimensional droplet profiles for varying choices of ϵ_w . As the attractive strength of the wall increases, the contact angle reduces and the droplet spreads out across the surface. Note that droplets with contact angles far above $\theta = 90^\circ$ can easily be found which is very difficult for other approaches such as the IH model.

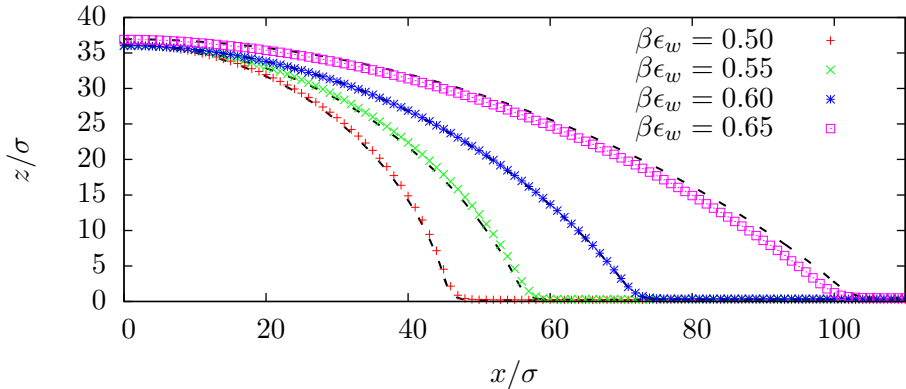


Figure 3.14: A comparison of film height profiles generated from the LG DFT (symbols) with those from the IH (dashes) model with the appropriate binding potential found using the DFT method described in §3.4. The droplet height profiles are calculated for a fluid state point defined by $\beta\epsilon = 0.9$ with a interactions range of $L = 5$ at various wall strengths $\beta\epsilon_w$.

contour can then be used as the film height profile. Alternatively one could define the height of the liquid film via Eq. (2.72) by relating it to the local adsorption at that point on the surface. The comparison displayed in Fig. 3.14 follows this second method of coarse-graining the DFT results, by following this method, rather than picking out the $\rho = 0.5$ contour, the precursor film can be seen. Very good agreement between the two methods is found with the IH results nicely following the DFT data for a wide range of contact angles. Comparisons are only made for contact angles up to $\theta = 90^\circ$ as it is very difficult to find droplet profiles beyond this with the IH model. This is because the film height profile, $h(\mathbf{x})$, becomes multivalued when $\theta > 90^\circ$. The DFT model has no such restriction and easily generates liquid droplets with contact angles up to $\theta = 180^\circ$ as is demonstrated in Fig. 3.13. For droplets where $\theta > 90^\circ$, extracting a film height profile via the adsorption would give misleading results as it is only possible to find a height profile that is single valued.

To give a slightly more quantitative comparison than in Fig. 3.14, the contact angles of the droplets can be directly compared. It is not straightforward to extract a contact angle from the height profiles since they contain a precursor film which the droplet smoothly transitions into. Such a droplet can be considered as having three distinct regimes: the precursor film, a spherical cap, and some transition region between these

two [51]. Using this spherical cap is one way to find a contact angle. By fitting a circle to the apex of the droplet, the contact angle that this circle makes with the substrate can be considered as the contact angle of the droplet itself. Since the top of the droplet is a stationary point the radius of curvature at this point is just the second derivative of the film height profile

$$r_c = \frac{1}{h''(x_{\max})}. \quad (3.59)$$

This can then be used to find the contact angle

$$\theta_c = \frac{\pi}{2} - \cos\left(\frac{a}{r_c}\right), \quad (3.60)$$

where a is half the distance between the two points where the circle meets the substrate. This could also be identified as the radius of the droplet. A second method to extract a contact angle is to find the steepest gradient in the height profile and take this to be the contact angle. This again relies on the idea that the droplet has a spherical shape in which case the steepest gradient is indeed the contact angle. A comparison of the contact angles is displayed in Fig. 3.15, both options for finding the contact angle from a film height profile are compared with the DFT contact angles found via Eq. (1.1). The two methods of finding the contact angle agree well for larger contact angles, but the circle fitting method is much more accurate for smaller contact angles. Fitting by the largest gradient overestimates the contact angle close to the wetting transition. Overall the matching of contact angles shows very good agreement between the DFT and IH models although as noted already, the IH model is only able to find contact angles up to $\theta = 90^\circ$ whereas the contact angles found via DFT are given up to $\theta = 180^\circ$.

A comparison between the DFT results and Eq. (1.5), which is the IH model under the long wavelength approximation, is also made in Fig. 3.15. This comparison is included as making the long wavelength approximation is a necessary step in deriving the thin film equation, Eq. (1.6) which describes the dynamics of liquid films and sliding droplets. It is possible to study the time evolution of fluids using DDFT [52, 53, 54, 55] but dynamics of larger droplets are much more easily studied via Eq. (1.6). Making the long wavelength approximation assumes that the contact angles are small and Fig. 3.15 verifies that the agreement between the two methods rapidly breaks down for larger contact angles. Using a binding potential as input to the thin film evolution equation could only be expected to yield accurate results for $\theta < 30^\circ$.

3.6 Conclusions

This chapter has focussed on a discrete DFT model, the lattice-gas model. The LG is fully derived here with long ranged interactions between fluid particles, the full 3D model is then reduced down to effective 1D and 2D versions which give a large computational

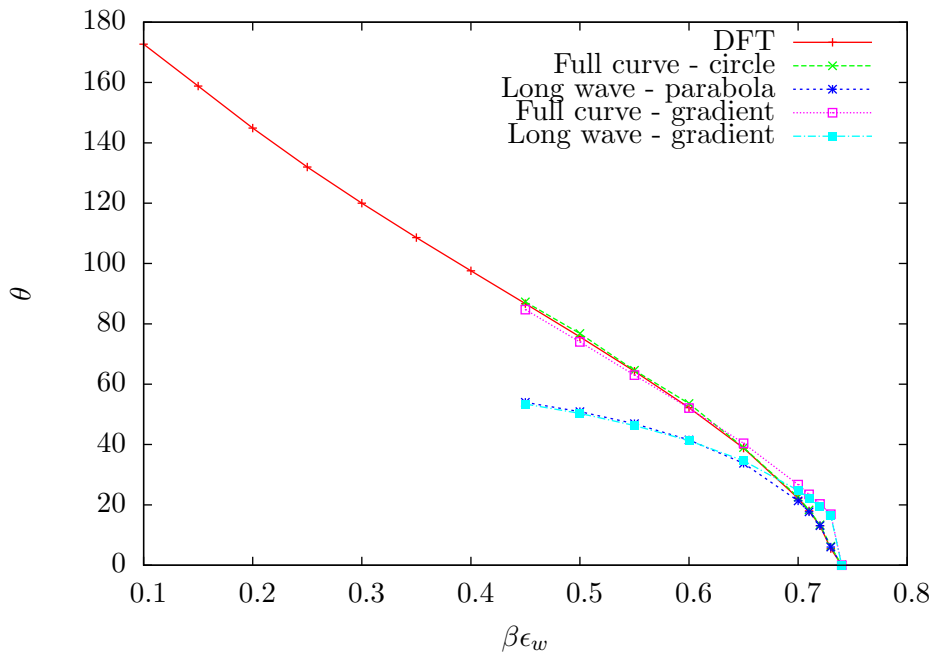


Figure 3.15: A comparison of contact angles calculated for liquid droplets calculated via DFT and the IH model. Contact angles for the IH model under the long wavelength approximation are also displayed. The long wavelength contact angles only agree for $\theta < 30^\circ$. Good agreement is found for the full IH model right up to $\theta = 90^\circ$ beyond which only the DFT model is able to find droplet profiles.

saving whilst still giving an exact match with the full 3D model under the same confining geometry. This model is then principally put to use in demonstrating a procedure for calculating a binding potential. This procedure allows a binding potential to be fully calculated even for a very small film thickness (or adsorption). Traditionally asymptotic forms of the binding potentials are used as input to larger scale models. This full calculation gives a form for the binding potential applicable at much smaller scales. The method of calculating the binding potential is essentially to find a constrained equilibrium free energy for incrementally increasing film heights where the particular form of the constraint, which effectively introduces a small fictitious external field to stabilise a film, not only fixes the average density of the system but also forces it to sit in two distinct phases.

The binding potential calculated from the LG model can be fitted to an algebraic form and then used as an input to mesoscopic models such as the IH model. In order to verify this method of calculating the binding potential, the output from the IH model, when using the binding potentials calculated using DFT as an input, was compared with raw output from the DFT model alone. In particular, the film height profiles of liquid droplets and their contact angles were compared from each of the models and very good agreement was found between them. The calculated binding potentials were also used to demonstrate the effects of truncating particle interactions, it was shown that the macroscopic phase behaviour of a fluid could change if the particle interactions were truncated at too short a range, this was indicated by a shift of the minima of the binding potentials at low adsorption from a local to a global minimum as the truncation range was increased.

The LG model is very simple and computationally quick to work with. However, being a discrete model means it can not capture certain physics. The structure of density profiles at a solid interface is not well described and layering transitions, seen in the adsorption isotherms, are too strongly emphasised due to particles being constrained to lattice sites. The biggest problem with this model as a demonstration of the method by which binding potentials can be calculated is that the discrete structure forces oscillations to occur in the tails of the binding potentials. To correct these artefacts the following chapter describes a continuum model based on the hard-sphere DFT of Chapter 2. The calculations performed here are repeated and reconfirmed before exploring some interesting structuring that occurs at state points below the ‘Fisher-Widom’ line. Below this line one expects to find oscillatory, rather than monotonic, decay of density profiles and binding potentials and highly structured 2D droplets can be found.

Chapter 4

A Continuum DFT Model

This chapter introduces a continuum DFT model, modelling the fluid as a hard-sphere reference state with the additional attractive pairwise interactions between fluid particles treated using a simple mean-field approximation. These attractive interactions take the form of a truncated and shifted LJ potential. This model is used to calculate binding potentials in the manner described in the previous chapter, correcting some of the errors arising from the discrete nature of the LG model and giving a better description of the contact line region. Towards the end of this chapter, a second, short ranged attractive pair potential, the Asakura-Oosawa (AO) potential is used instead of the LJ potential. With this short ranged pair potential and at lower temperatures, the fluid has density profiles and binding potentials that are strongly oscillatory for fluids at state points below the Fisher Widom (FW) line [56, 57, 58]. Interesting droplet structures can be found that arise from the oscillatory nature of these binding potentials.

4.1 The DFT Model

The perturbative approximation for the free energy introduced in Eq. (2.46) is used to calculate binding potentials in this chapter. The excess Helmholtz free energy of a fluid is expressed as a perturbation about some reference state:

$$F_{\text{ex}}[\rho(\mathbf{r})] = F_r[\rho(\mathbf{r})] + \frac{1}{2} \iint \rho(\mathbf{r}_1)\rho(\mathbf{r}_2)v(|\mathbf{r}_1 - \mathbf{r}_2|) d\mathbf{r}_1 d\mathbf{r}_2. \quad (4.1)$$

The reference fluid is the hard-sphere fluid described by the White Bear FMT model discussed in Chapter 2. The perturbation is a pairwise interaction v which accounts for the attractive interactions between fluid particles and the factor of 1/2 in Eq. (4.1) is included to prevent double counting of the particle interactions. The grand free energy

of such a fluid system is then given by

$$\begin{aligned}\Omega[\rho(\mathbf{r})] = & k_B T \int \rho(\mathbf{r}) (\ln(\Lambda^3 \rho(\mathbf{r})) - 1) d\mathbf{r} + \int \Phi(\{n_\alpha\}) d\mathbf{r} \\ & + \frac{1}{2} \iint \rho(\mathbf{r}_1) \rho(\mathbf{r}_2) v(|\mathbf{r}_1 - \mathbf{r}_2|) d\mathbf{r}_1 d\mathbf{r}_2 + \int \rho(\mathbf{r}) (V(\mathbf{r}) - \mu),\end{aligned}\quad (4.2)$$

where $\Phi(\{n_\alpha\})$ is given by Eq. (2.55). The attractive pair interaction is defined as a truncated and shifted Lennard-Jones (LJ) potential

$$v(r) = v_{\text{LJ}}(r) - v_{\text{LJ}}(r_c), \quad (4.3)$$

where r_c is a cut off range and

$$v_{\text{LJ}}(r) = \begin{cases} 4\epsilon \left((\sigma/r)^{12} - (\sigma/r)^6 \right) & \text{if } \sigma < r \leq r_c \\ 0 & \text{otherwise.} \end{cases} \quad (4.4)$$

The cut off range r_c is analogous to the truncation range L in the previous chapters. The effect of varying this range is discussed below. The density profile that minimises Eq. (4.2) is also the solution to the Euler-Lagrange equation

$$\frac{\delta \Omega}{\delta \rho} = 0. \quad (4.5)$$

The presence of attractive interactions means that phase separation can occur to the liquid and gas phases. All of the results in this chapter are calculated at the point of liquid-gas coexistence. The bulk fluid phase diagram in Fig. 4.1 shows the coexisting liquid and gas densities and is found by solving the simultaneous equations

$$\begin{aligned}p(\rho_g) &= p(\rho_l), \\ \mu(\rho_g) &= \mu(\rho_l),\end{aligned}\quad (4.6)$$

at a fixed temperature T . This gives the points where the pressure, chemical potential and temperature are equal for each phase. In the bulk fluid, the FMT weighted densities become much simpler, the vector weighted contributions vanish and the scalar weighted densities are simply the bulk density multiplied by the integrated weight function. The Helmholtz free energy per unit volume in the bulk fluid is

$$f(\rho) = k_B T \rho (\ln(\Lambda \rho) - 1) + \frac{4\pi R^3 \rho^2}{1 - \frac{4}{3}\pi R^3 \rho} + \frac{\frac{4}{3}\pi R^3 \rho^2}{(1 - \frac{4}{3}\pi R^3 \rho)^2} + \frac{1}{2} \rho^2 \int v(\mathbf{r}) d\mathbf{r}, \quad (4.7)$$

and the pressure and chemical potential can be found via Eqs. (3.36) and (3.37). The solution of Eq. (4.6) for various values of T gives the phase diagram plotted in Fig. (4.1). The spinodal is also plotted in this figure which is found identically as in Chapter 3.

Note that in Eq. (4.7) the form of the potential, $v(r)$, is not important, it is only the integrated value of this function which determines the free energy per unit volume. As such, the phase diagram of a fluid where the Helmholtz free energy is given by the form of Eq. (4.1) with any choice of $v(r)$ would just be a rescaling of the one given in Fig. 4.1. To ensure that varying the cut off ranges, r_c , does not alter the bulk fluid phase behaviour and phase diagram, the interaction strength ϵ is renormalised so that the integrated strength of the pair potential remains equal to the value when $r_c \rightarrow \infty$. When an interaction strength, ϵ , is quoted in this Thesis, this is the equivalent value for $r_c \rightarrow \infty$ and the true interaction strength is

$$\epsilon_{\text{true}} = \epsilon / \left(1 + 2 \left(\frac{\sigma}{r_c} \right)^9 - 3 \left(\frac{\sigma}{r_c} \right)^3 \right). \quad (4.8)$$

In Chapter 2 a method to numerically minimise the grand free energy was presented which used the Picard iteration scheme

$$\rho(\mathbf{r}) = \rho_b \exp(c^{(1)}(\mathbf{r}) - \beta V(\mathbf{r}) - c^\infty). \quad (4.9)$$

With the additional contribution from the pair potential v , the one body direct correlation function is now $c^{(1)}(\mathbf{r}) = c_{\text{hs}}^{(1)}(\mathbf{r}) + c_p^{(1)}(\mathbf{r})$, where

$$\begin{aligned} c_p^{(1)}(\mathbf{r}) &= -\beta \frac{\delta}{\delta \rho(\mathbf{r})} \frac{1}{2} \iint \rho(\mathbf{r}) \rho(\mathbf{r}') v(|\mathbf{r} - \mathbf{r}'|) d\mathbf{r} d\mathbf{r}', \\ &= -\beta \int \rho(\mathbf{r}') v(|\mathbf{r} - \mathbf{r}'|) d\mathbf{r}'. \end{aligned} \quad (4.10)$$

As with the LG discussed in Chapter 3, the iterative scheme is continued until a convergence criterion is satisfied. The difference in the density profiles between two successive iterations must become less than a specified value, again this criterion is set to be $\delta < 10^{-7}$. The continuous density profile is discretised and the difference between the two successive density profiles is calculated as Eq. (3.47). In this instance the sum is over all discrete calculation points rather than the lattice sites. The solution space is discretised with a step size of $\delta x = 0.01\sigma$ for 1D calculations. The effect of the grid spacing on the accuracy of calculations is demonstrated in Fig. 4.9. A coarser grid space is used for 2D models but this is shown to give results consistent with the finer 1D model. The system size is again made large enough so that the density profile is fully reduced to the bulk density and so the size of the system does not affect the results.

In Chapter 2 the FMT reference fluid was reduced to describe a fluid in a 1D or 2D geometry. This reduction in complexity leads to a faster calculation. An expression for the pair potential in lower dimensions is required to reduce the dimensionality of the full model. This is found by integrating over the invariant dimensions, as in Eqs. (2.63) and

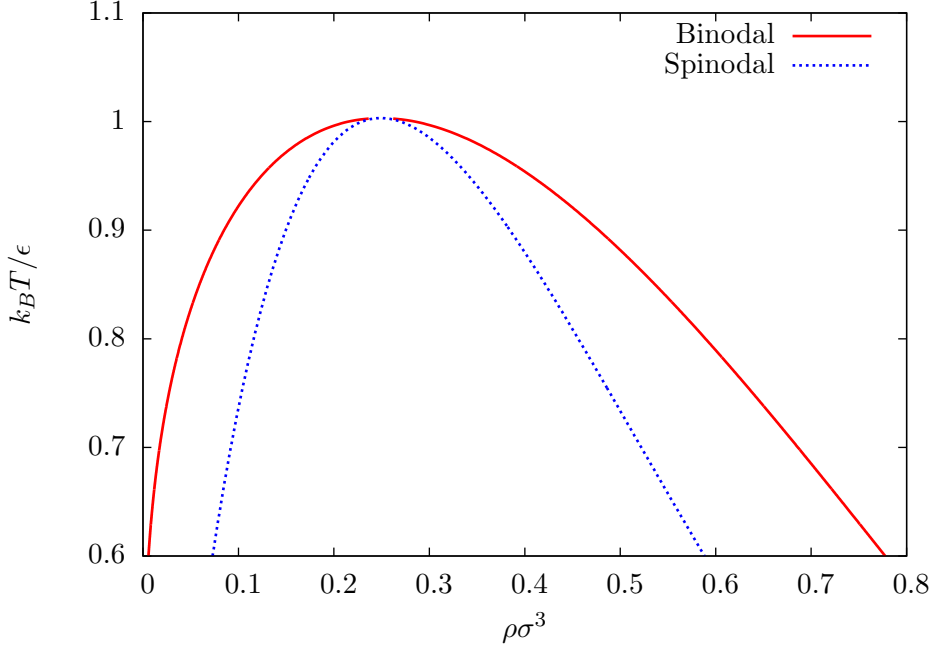


Figure 4.1: Phase diagram for the continuum model. The parameter ϵ is the integrated strength of the pair potential $v(r)$. The red solid curve shows the binodal, which are the coexisting liquid-gas densities. The blue curve is the spinodal which is linear instability threshold of the fluid.

(2.64). The resulting 1D pair potential is

$$v_{LJ}^{1D}(z) = \begin{cases} v_{LJ}^{1D}(z) - \pi(r_c^2 - z^2)v_{LJ}(r_c) & \text{if } \sigma < r < r_c \\ 0 & \text{otherwise,} \end{cases} \quad (4.11)$$

where

$$v_{LJ}^{1D}(z) = \begin{cases} 2\epsilon\pi(2\sigma^{12}z^{-10} - 2\sigma^{12}r_c^{-10} + 5\sigma^6r_c^{-4} - 5\sigma^6z^{-4})/5 & \text{for } \sigma < z \leq r_c \\ 2\epsilon\pi(-2\sigma^{12}r_c^{-10} + 5\sigma^6r_c^{-4} - 3\sigma^2)/5 & \text{for } z \leq \sigma. \end{cases} \quad (4.12)$$

A similar expression can be calculated for the effective 2D model, this 2D expression can easily be found but is quite lengthy and so is omitted here.

It is assumed that the fluid particles interact with the particles in an external boundary via the pair potential Eq. (4.3) and an additional hard-core repulsion term. The net integrated interaction of a single fluid particle with all of the particles in the external boundary is given by the external field

$$V(\mathbf{r}) = \frac{2\pi\sigma^3 f \epsilon}{3} \left(\frac{2}{15} \left(\frac{\sigma}{z + \sigma/2} \right)^9 - \left(\frac{\sigma}{z + \sigma/2} \right)^3 \right) \text{ if } z \geq \sigma/2, \quad (4.13)$$

where z is the perpendicular distance of a fluid particle at \mathbf{r} from the wall and $V(z) \rightarrow \infty$

f	Model	$\beta\gamma_{lg}\sigma^2$	$\beta\gamma_{wl}\sigma^2$	$\beta\gamma_{wg}\sigma^2$	θ
0.3	MD	0.489	0.375	-0.014	137°
	DFT	0.373	0.290	-0.002	142°
0.6	MD	0.489	0.028	-0.014	99°
	DFT	0.373	0.053	-0.028	103°
1.0	MD	0.489	-0.548	-0.062	39°
	DFT	0.373	-0.419	-0.102	32°

Table 4.1: A comparison of contact angles and surface tensions for molecular dynamics simulations with the present DFT model for the temperature $T = 0.75T_c$.

if $z < \sigma/2$. The parameter f gives the density of the particles that make up the container wall and ϵ is the same interaction strength parameter from Eq. (4.4). The product $f\epsilon$ determines the attractive strength of the external field and can be replaced by the single parameter $\epsilon_w = f\epsilon$. Using the product notation $f\epsilon$ allows for easier comparison with existing simulation data [59] and shows the relative attractive strength of the external field compared to the fluid-fluid interaction strength. The absolute parameter ϵ_w allows an easier comparison of fluids defined by various choices of ϵ on the same substrate.

One motivation for selecting Eq. (4.3) as the pair potential in this model is its frequent use as a model potential in numerical simulations [17, 49, 59]. Here, a comparison is made with the simulation results presented in Ref. [59]. The surface tensions and contact angles for a fluid within different external fields for both the present DFT model and the simulation results of [59] are shown in Table 4.1. The agreement of the contact angles between the two models is surprisingly good. DFT is a mean field theory and so does not capture all of the interfacial fluctuations that the molecular dynamics (MD) simulations do and so some discrepancy should be expected. The MD results were found for a fixed temperature of $T = 0.75T_c$ and the DFT results were found equivalently for $\epsilon = 4/3\epsilon_c$ where ϵ_c is the critical value of ϵ for a fixed $\beta = 1$. This gives coexisting densities of $\rho_g\sigma^3 = 0.0127$ and $\rho_l\sigma^3 = 0.7606$ for the simulation results and $\rho_g\sigma^3 = 0.0277$ and $\rho_l\sigma^3 = 0.6367$ for the DFT results. There are differences between the surface tensions but interestingly, the calculated contact angles are in very good agreement.

4.1.1 Density Profiles and Adsorption Constraints

The equilibrium density profiles of this model fluid within the external field Eq. (4.13) can be found by minimising the free energy following the procedure laid out in Chapter 2 and using Algorithm 3.1. A selection of such profiles are displayed in Fig. 4.2. Comparing these continuum density profiles to the results found from the LG model shows that a lot more fluid structure is resolved in the continuum model. In particular, strong density peaks relating to packing of fluid particles can be observed for strongly attracting substrates. A wetting film is observed for the curves corresponding to $f = 1.4$ and

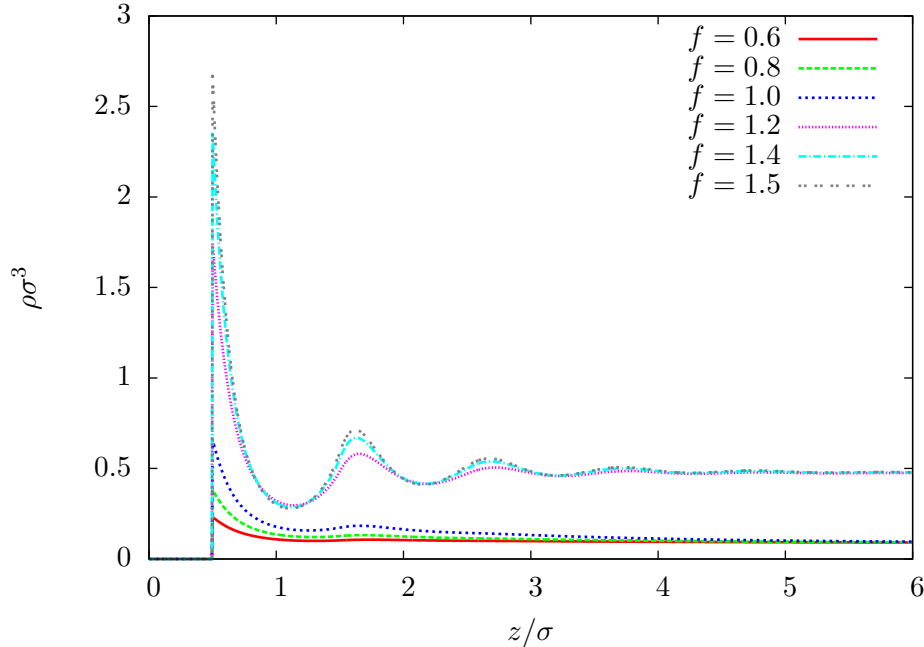


Figure 4.2: Density profiles for the continuum fluid with $\beta\epsilon = 1.1$ and $\mu = \mu_c$ against a substrate of varying attractive strength. There is more fluid structure for greater attractive strengths f , particularly for $f \geq 1.2$, when the fluid wets the wall and so there is a thick (macroscopic) film of the liquid adsorbed on the wall.

$f = 1.5$. In these cases there is a thick film of the higher density liquid adsorbed on the wall.

A constrained equilibrium can be found by applying Eq. (3.56) during the minimisation procedure. This gives a liquid film having a particular value for the adsorption that is effectively stabilised by a fictitious external field. A fluid constrained to have various values for the adsorption is displayed in Fig. 4.3 along with the fictitious potentials required to stabilise them. In the figure the plain lines show the constrained density profiles for various Γ and the lines of the same colour marked with points show the corresponding fictitious potentials, which are plotted against the opposite vertical axis. Density profiles with lower adsorptions are shown in 4.3a and higher adsorptions are shown in 4.3b where the quantity of liquid adsorbed at the wall is approaching what may be called a macroscopic value. In these higher adsorption density profiles the fluid, moving away from the wall, first has the coexistence bulk liquid density value before then decaying to the bulk gas density. The data in 4.3a also corresponds to the coloured points on the binding potential in 4.3c which gives insight into why the fictitious potentials have a negative or positive sign. The fictitious fields have a negative sign for positive gradients of the binding potential and a positive sign for negative gradients. To illustrate this consider a density profile with $\Gamma\sigma^2 = 1$ under the true external field without the fictitious stabilising field. The gradient of the binding potential at this point

is negative. In this situation the system would relax to the equilibrium density profile at $\Gamma\sigma^2 = 0.5$, decreasing the adsorption. More strongly attractive external fields lead to equilibrium density profiles with a higher adsorption value and so, to stabilise this film with $\Gamma\sigma^2 = 1$, an additional attractive field must be added to the true external potential. Conversely, to stabilise a density profile with an adsorption value that lies outside of the potential well of this local minimum, an additional repulsive external field is required. The unconstrained behaviour in this case would increase the film thickness towards the minimum at infinite adsorption. The repulsive fictitious field forces a lower adsorption. The density profile that sits exactly at the local minimum, for $\Gamma\sigma^2 = 0.5$, has a fictitious external field that is uniformly zero, this is the unconstrained solution. Note that this is only a local minimum of the free energy and the true equilibrium solution is actually found as $\Gamma \rightarrow \infty$. The density profile corresponding to $\Gamma\sigma^2 = 0.2$ (red curve) is plotted in 4.3a but the corresponding fictitious field is not plotted. This is because it is very large, approximately two orders of magnitude greater than the fictitious fields for the other adsorption values displayed in Fig. 4.3. For the larger adsorption values shown in 4.3b, the fictitious field extends only as far as the liquid layer and the magnitude of this field decreases for larger adsorptions as the energetic minimum is approached. The fictitious field is only very large when the adsorption is very small. Such a large fictitious field is not surprising since to enforce $\Gamma \rightarrow 0$, one has to remove all of the liquid from the surface thereby cancelling the effect of the true external field that is attracting the fluid to the wall. Therefore, one must expect the fictitious potential to be of the same magnitude as the true potential as $\Gamma \rightarrow 0$.

With the same adsorption constraint applied to the 2D model, droplet profiles (3D ridges) can be found as constrained equilibrium solutions to the model. A selection of droplet profiles are shown in Fig. 4.4 for contact angles of $\theta = 151^\circ$, 20° and 87° . A lot more structure at the wall can be observed in these results from the continuum model than could be observed in the LG model results in Chapter 3. The contact region where the edge of the droplet meets the substrate is quite diffuse with substantial density oscillations, as seen in 4.4e. Packing of particles in the body of the droplet can also be seen from the density peaks close to the substrate. The thin precursor film is also present which shows just one or two density peaks. A zoom of this precursor region is shown in Fig. 4.4b for all three droplets.

4.1.2 Binding Potentials

The continuum DFT model is now used to calculate binding potentials using the same method as described in Chapter 3 with the LG model. To briefly recap: this method calculates the binding potential by finding the constrained equilibrium density profiles for a range of Γ . For each Γ the value of the binding potential at that point is calculated

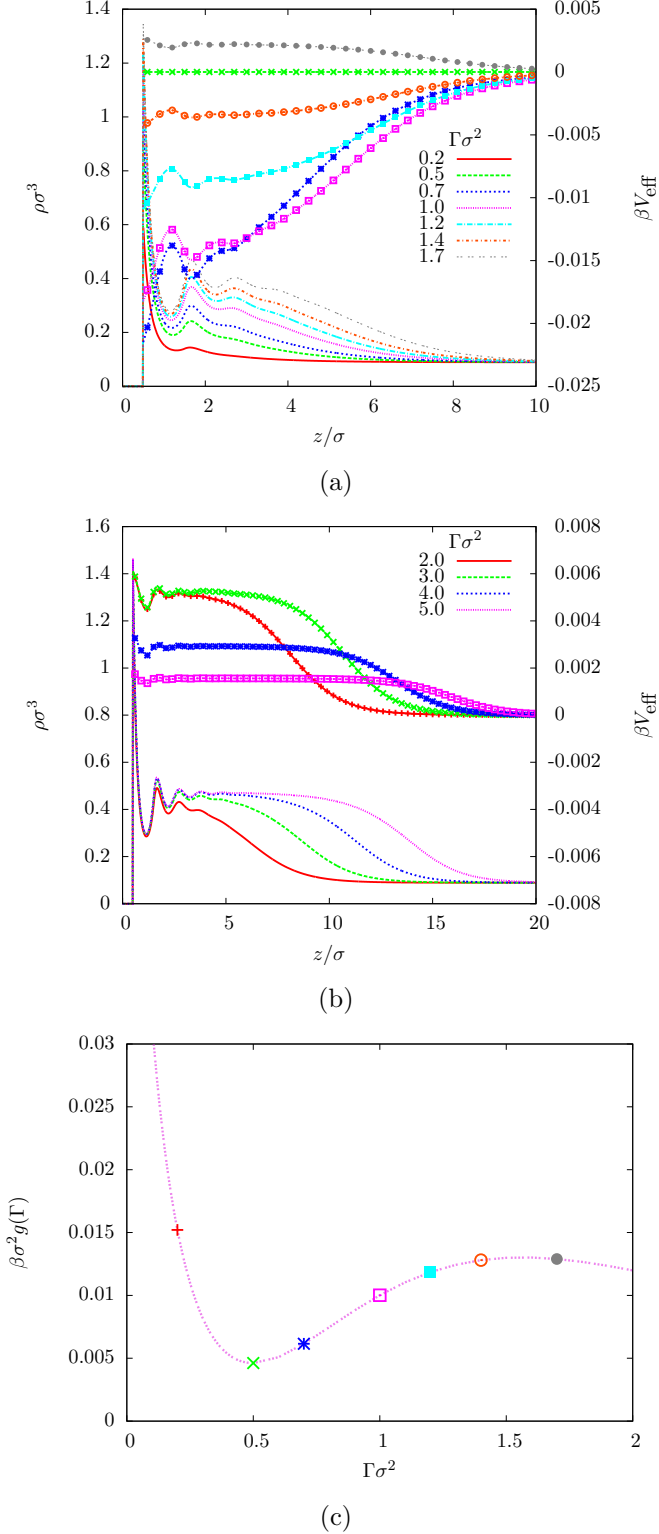


Figure 4.3: Density profiles for a fluid with $\beta\epsilon = 1.1$ and $\mu = \mu_c$ with specified values of the adsorption displayed together with the fictitious external potentials that are needed to stabilise them. In (a) and (b) the plain lines are the density profiles (left axis) and the lines with points are the fictitious potentials (right axis). The fictitious potential for $\Gamma\sigma^2 = 0.2$ is not displayed as its magnitude is greater than the scale displayed, it is approximately 100 times larger than the other potentials. Smaller adsorption values are shown in (a) which also correspond to the coloured points of the binding potential shown in (c).

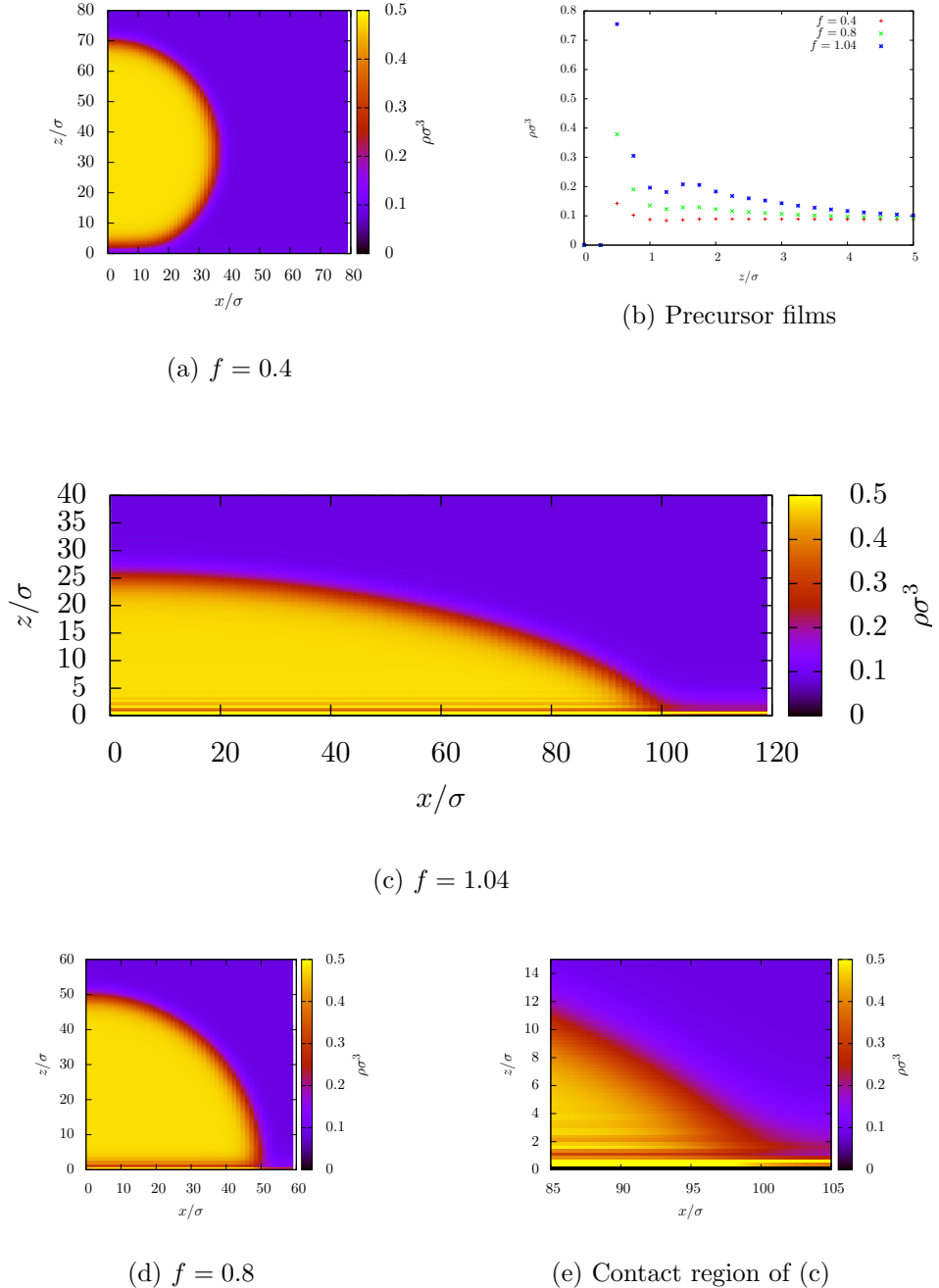


Figure 4.4: Droplet profiles for a fluid of fixed volume with $\beta\epsilon = 1.1$ and $r_c/\sigma = 5$ against substrates of varying attraction strength f . The contact angles for the droplets in (a), (c) and (d) are $\theta = 151^\circ$, 20° and 87° respectively. A plot of the density profiles at the wall in regions away from the droplets (i.e. the precursor film) is shown in (b) and a zoom of the contact region of the droplet in (c) is shown in (e).

from

$$g(\Gamma) = \frac{\Omega(\Gamma) - \Omega_b}{A} - \gamma_{wl} - \gamma_{lg}. \quad (4.14)$$

This series of points gives the binding potential which can also be fitted to an algebraic form where Γ gives a measure of the film thickness. An example of these binding potentials for a fluid with $\beta\epsilon = 1.1$ and $r_c = 5\sigma$ for various substrate attractive strengths is shown in Fig. 4.5. The inset of this figure shows that the binding potentials still exhibit the expected $\sim \Gamma^{-2}$ decay but no longer have oscillatory tails as the liquid film is able to grow smoothly unlike the previous discrete model where the growth was constrained by the lattice. It is shown below in §4.2 that oscillations can still occur in the continuum model but these oscillations stem from the physics of the system rather than as an artefact of the lattice modelling. Aside from the absence of oscillations, the binding potentials found via the continuum model exhibit the same qualitative behaviours as found in those from the LG model. One slight difference is that the low adsorption minimum of the binding potentials occur at lower adsorption values than with the LG model. For instance, the minimum for the $f = 0.3$ case in Fig. 4.5 occurs at a very small negative value of the adsorption. Negative adsorptions are much easier to resolve with the continuum model due to the finer resolution of the structure of the density profile in the contact region. The adsorption values at which minima occur are lower than for the LG model because the coexisting liquid and gas densities are much closer together in value in the continuum model. A liquid film of a given thickness in the continuum model has a much lower adsorption than a film of the same thickness described by the lattice model.

These binding potentials should be related to the density profiles that are displayed in Fig. 4.2. Note that for $f < 1.2$ the global minimum occurs at a low value of the adsorption which corresponds to a non-wetting fluid. This is reflected in the density profiles of Fig. 4.2 where the corresponding density profiles all have only a small amount of fluid adsorbed to the wall. The global energetic minimum occurs at infinite adsorption in Fig. 4.5 for the external fields $f = 1.2$ and $f = 1.4$ and then density profiles for these cases in Fig. 4.2 show a macroscopic liquid layer adsorbed to the wall. When calculating the density profiles some care should be taken to ensure that the density profile corresponding to the true equilibrium is found. The numerical solution to Eq. (4.5) depends on the initial condition used in the minimisation procedure. If, for instance, for the external field with $f = 1.0$, the initial condition is given as a profile with density near that of the bulk liquid, then the minimisation procedure generates the density profile that is the local minimum with infinite adsorption. To find the global minimum an initial condition with a low adsorption must be supplied.

The depth of the potential well of the low adsorption minimum is strongly dependent on the fluid-fluid interaction strength ϵ , or equivalently, the temperature. As the temperature is decreased (or ϵ is increased) the point on the phase diagram at which

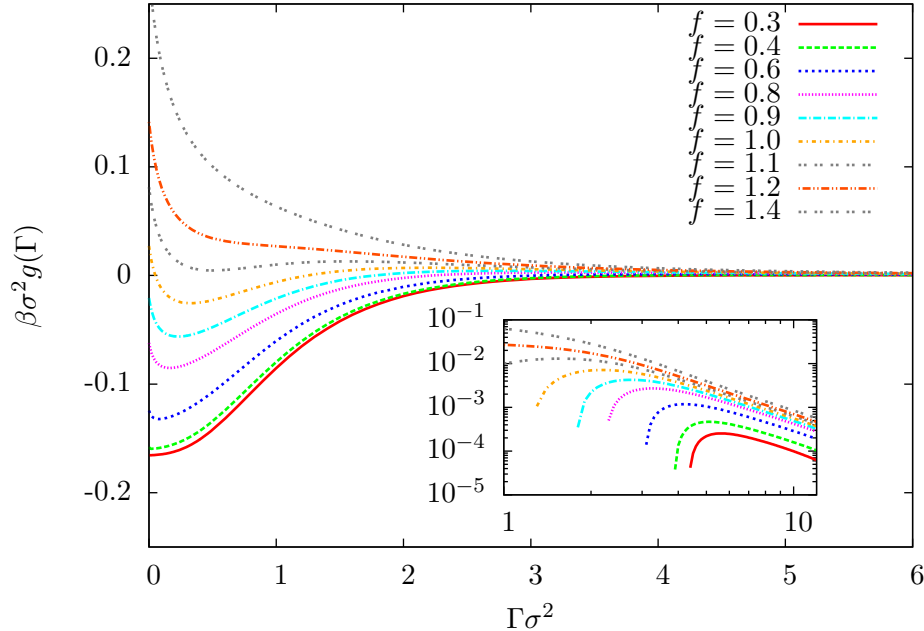


Figure 4.5: A range of binding potentials found using the continuum DFT model. The fluid-fluid interactions have an attractive strength of $\beta\epsilon = 1.1$ and are truncated beyond a range of $r_c = 5\sigma$. The inset shows the same data on a logarithmic scale. The binding potentials have the same $\sim \Gamma^{-2}$ decay, due to the external field that is not truncated.

liquid-gas coexistence occurs moves further away from the critical point. The densities of the coexisting liquid and gas phases move further apart and the depth of the well in the binding potential increases. This behaviour is illustrated in Fig. 4.6 where the binding potentials for two different external fields are shown. The first case, (a), is for a fixed attractive strength of the external field, $\beta\epsilon_w = 0.7$. The external field does not change as the value of ϵ is varied. The attractive strength of the second external field in case (b) is defined relative to the fluid-fluid interactions, i.e. $\epsilon_w = f\epsilon$. Here the attractive strength of the substrate is increased with increasing ϵ , but this still leads to a raising of the minimum value at low adsorption, as the fluid becomes more wetting. Whichever external field is chosen, the depth of the potential well for small Γ decreases as the critical temperature is approached.

For the LG model, it was shown that truncating the particle interactions can have a significant effect on the wetting behaviour. The continuum DFT results show that this is generally true and is not just an artefact of the lattice model. In Fig. 4.7, interaction ranges are truncated at a range of values from $r_c = 2.5\sigma$ to $r_c = 20\sigma$. In computer simulations it is common to truncate the Lennard-Jones potential at a range of $r_c = 2.5\sigma$. However, the results in Fig. 4.7 show that there is a change in the interfacial phase behaviour when increasing the range of fluid-fluid pair interactions from 5σ to 10σ . This shows that for this temperature, making the usual $r_c = 2.5\sigma$ truncation would lead to an

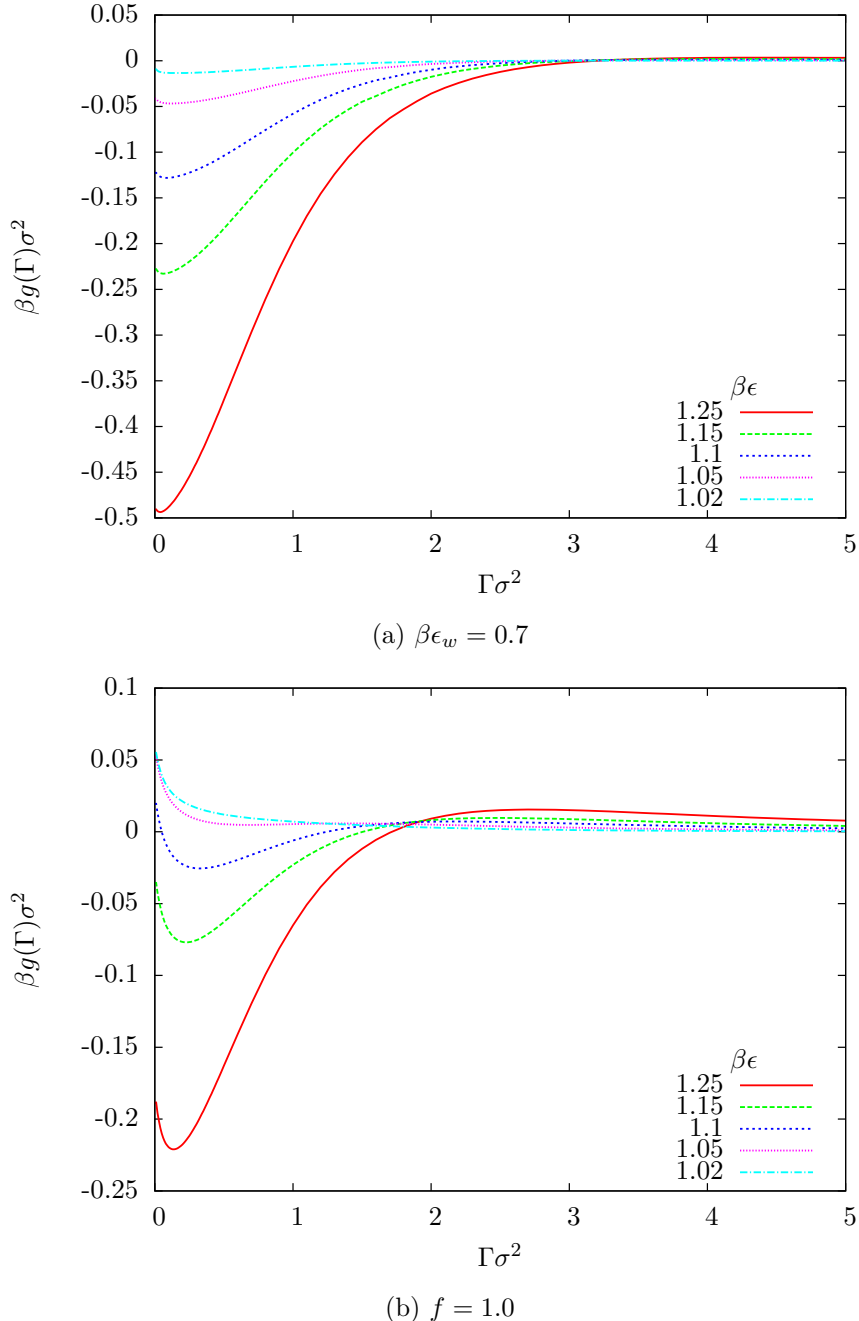


Figure 4.6: As the strength of fluid-fluid interactions is increased (or temperature is decreased) the fluid becomes less wetting and the depth of the low adsorption minima increases. Results are shown for (a) a substrate of fixed attractive strength ϵ_w and (b) a substrate with an attractive strength relative to that of the fluid-fluid interactions f .

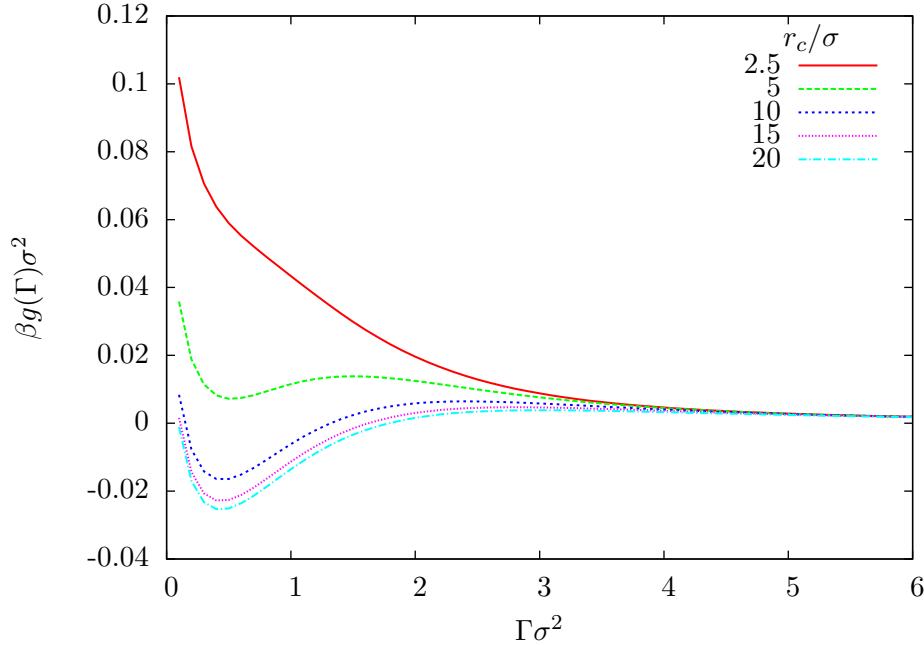


Figure 4.7: The binding potential for $\beta\epsilon = 1.1$ and $\beta\epsilon_w = 1.25$ calculated for a range of different values of the cut-off range r_c . Computer simulations often truncate the particle interactions at a range of $r_c = 2.5\sigma$. Here, there is a shift in the interfacial phase behaviour as the range of the interactions is varied. Going from $r_c = 5\sigma$ to $r_c = 10\sigma$ changes the system from non-wetting to wetting.

incorrect prediction of the wetting behaviour. The five binding potentials displayed in Fig. 4.7 are all for the case when the external potential has a fixed strength of $\beta\epsilon_w = 1.25$ and the range is not truncated. Each calculation is made at the same point on the bulk fluid phase diagram by renormalising ϵ according to the truncation range, c.f. Eq. (4.8). This observation is particularly pertinent in light of the good agreement with computer simulation results shown in Table 4.1. That the LG model also shows this phenomenon, illustrates the fact that even though it is a very simplistic model, it does in fact predict the same behaviour as the more accurate continuum model which is in fair agreement with the computer simulation results.

The binding potentials calculated from the continuum model can be fitted with the same algebraic form as used for the lattice model, the one given in Eq. (3.51). Some examples of the fitting parameters are given in Appendix B. A good fit is achieved with this function as is demonstrated in Fig. 4.8. This fit function can be used as input to the IH model to find droplet film height profiles and these can be compared directly with film height profiles extracted from the 2D droplet density profiles calculated using DFT. The above binding potential results have all been found from the effective 1D version of the model where a finer value of the grid spacing for the numerics can be used ($\Delta x = 0.01\sigma$). However, in order to make comparisons of droplet profiles between the DFT and the IH models, the binding potentials that are to be used as input to

the IH model are calculated from the effective 2D model which requires a coarser grid ($\Delta x = 0.25\sigma$). The effect of the coarser grid is that there can be small errors, particularly within the integration of the LJ perturbation, compared to the 1D model. These small errors can lead to sizeable deviations in the comparisons between the contact angles of the two models. These errors are particularly prevalent at state points close to the wetting transition where small shifts in the minimum of the binding potential, $g(h_0)$, lead to appreciable changes in the calculated contact angle. Therefore, for a consistent comparison, it is better to calculate both the binding potentials and the droplet profiles from the same effective 2D model. However, the 2D model is far more computationally expensive. This is particularly so for larger r_c , i.e. truncating the LJ tail at greater ranges. The total system must be at least twice as wide as the range r_c which means large computational domains must be used and therefore slow calculations with large memory requirements. Using the 1D version of the DFT model means that calculations can be made with greater accuracy, at longer truncation ranges and in a shorter space of time. A comparison of density profiles calculated from the 1D and 2D versions of the model are displayed in Fig.4.9. Various grid spacings in both one and two dimensions are displayed and there is good agreement between all of the results. Discrepancies enter in numerical integration. Numerical integration is necessary for calculating free energies, etc, and small variations here between the 1D and 2D versions of the DFT can cause significant variation in the calculation of contact angles and droplet profiles. Even though the 1D DFT is more accurate than the coarser 2D DFT, it is not an important consideration. The less accurate 2D model is sufficient to demonstrate the applicability of the method of calculating the binding potential for use as an input in larger scale models.

Using the binding potential, calculated with the 2D DFT, as input to the IH model, liquid droplet profiles are found and directly compared with those calculated using DFT. This comparison is shown in Fig. 4.10, the parameters used to fit the binding potentials to Eq. (3.51) are given in Appendix B. Excellent agreement is found between the two models over a wide range of contact angles. A very small discrepancy exists in the contact line region where the IH model slightly underestimates the film height. To make this comparison a film height profile is extracted from the 2D density profile by first calculating the local adsorption at each point along the surface and then converting this a film height via Eq. (2.72) to give the height of the droplet at each point. The two droplets are both constrained to have the same average film height, which is identical to fixing the volume of the two droplets. No constraint is made upon the maximum height of the droplets but the agreement of this maximum height between the two methods is very good.

An alternative method of finding a film height profile from the density profile of a liquid droplet is to use the contour of a specific density value, such as the density value $(\rho_l + \rho_g)/2$ which is the value half way between the two coexisting densities. Finding

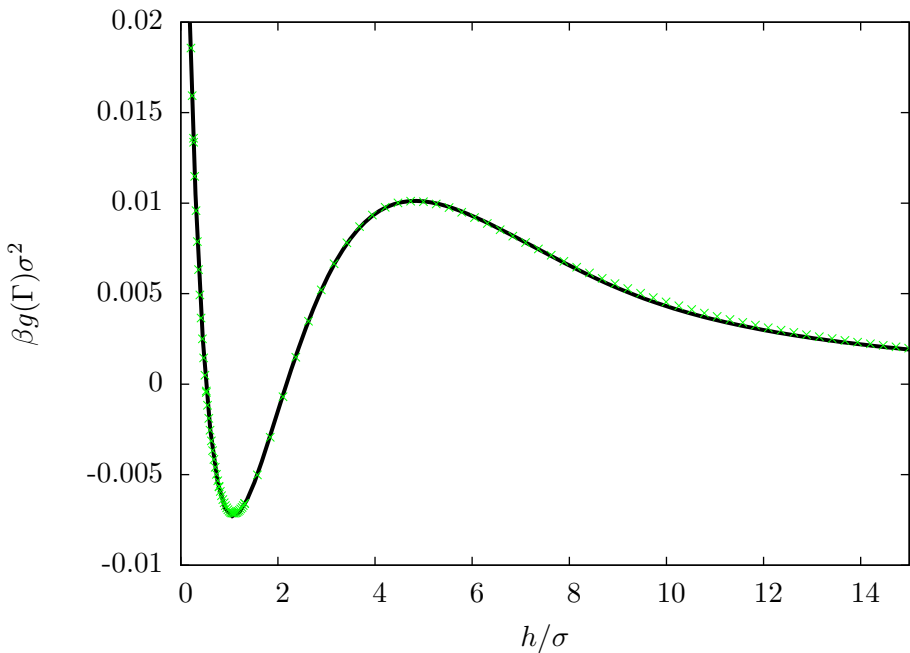


Figure 4.8: A demonstration of the quality of fit achieved with the fit function given by Eq. (3.51) with a binding potential calculated from the continuum DFT model. The binding potential displayed here is for a fluid with $\beta\epsilon = 1.1$, $\beta\epsilon_w = 1.06$ and $r_c = 5$. The black line is the fit function and the green symbols are the data points from the DFT calculation.

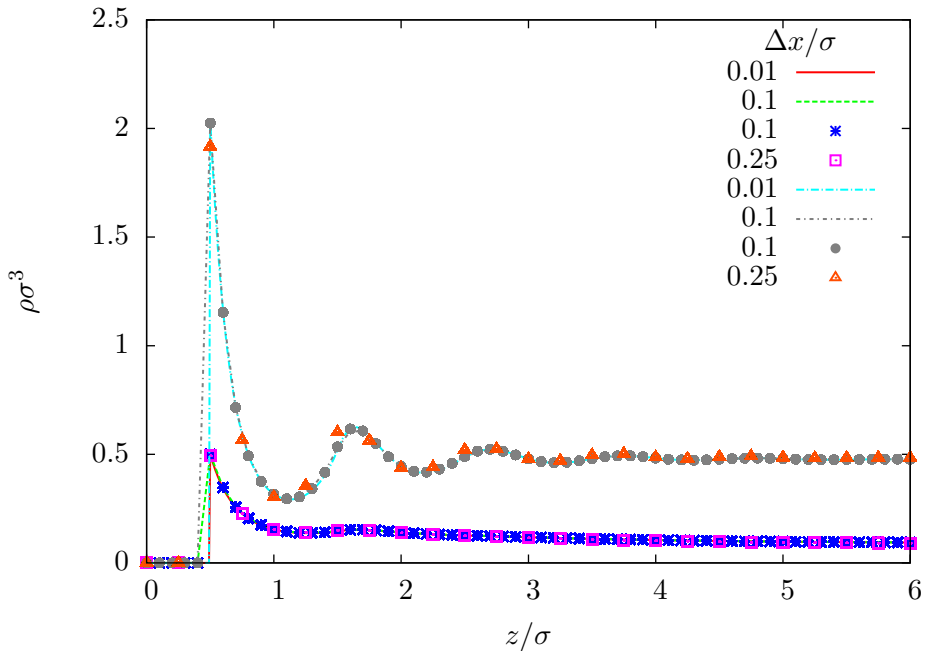


Figure 4.9: A comparison is made between results from the 1D version of the continuum DFT and the 2D version. The equilibrium density profile for a fluid with $\beta\epsilon = 1.1$ and $\mu = \mu_c$ against a wall with $f = 0.9$ and $f = 1.3$ is calculated from the 1D DFT for grid spacings of $\Delta x = 0.01\sigma$ and $\Delta x = 0.1\sigma$, and from the 2D DFT for grid spacings of $\Delta x = 0.1\sigma$ and $\Delta x = 0.25\sigma$. A wetting film is observed for $f = 1.3$ and a non-wetting film for $f = 0.9$. The lines represent results from the 1D DFT and the points are from the 2D DFT. Even a very coarse grid spacing of $\Delta x = 0.25\sigma$ is in good agreement with the finer grid spacings of the 1D DFT. Errors between the different dimensionality and grid spacings of the models enter during numerical integration.

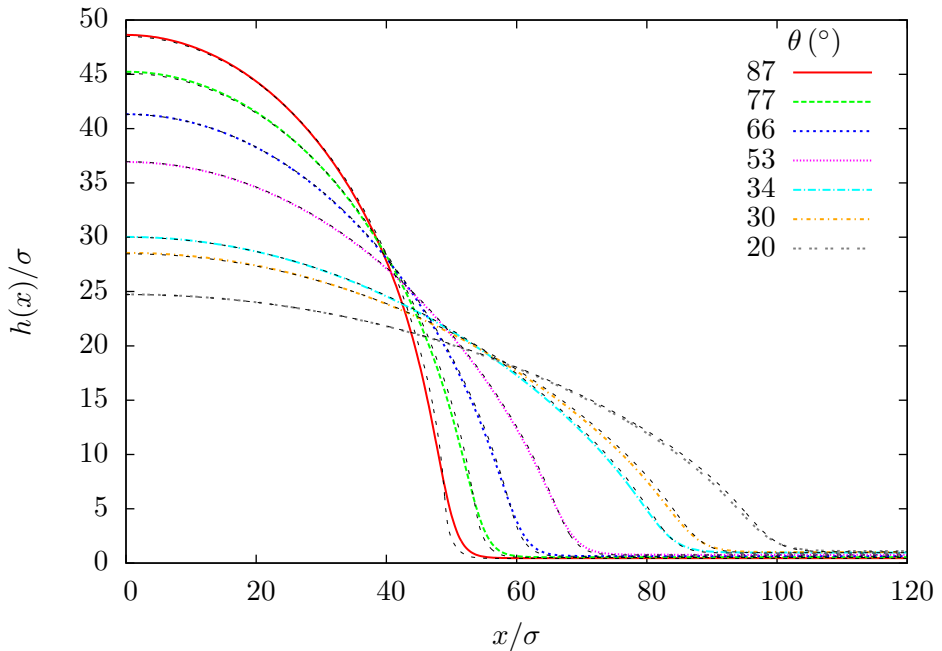


Figure 4.10: A comparison of droplet profiles for the fluid with $\beta\epsilon = 1.1$, $r_c = 5\sigma$ and $\mu = \mu_c$ with various wall strengths, $f = 0.8, 0.85, 0.9, 0.95, 1.01, 1.02, 1.04$. The coloured lines show film height profiles calculated from the DFT model and the black lines show the corresponding droplet profile found from the IH model using the binding potential obtained from the DFT model as input. Excellent agreement is found for the whole range of contact angles.

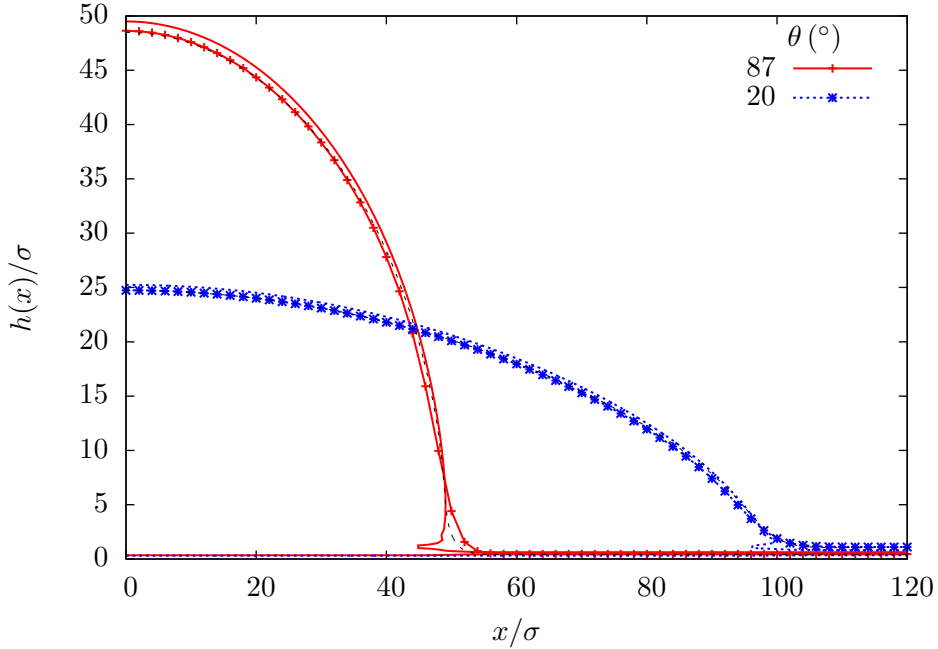


Figure 4.11: An alternative method for extracting a film height profile, namely, the density contour half way between the bulk coexistence liquid and gas densities is used to find the droplet profile. More structure can be seen with this method. The plain lines are the density contour and the lines with points are the profiles found by calculating the local adsorption. The black lines show the IH results. The droplet profiles are the same as those from Fig. 4.10, a fluid with $\beta\epsilon = 1.1$ and $f = 0.8$ (red curve) and $f = 1.04$ (blue curve).

a height profile in such a way better shows the structure of the droplets in the contact region as illustrated in Fig. 4.11. However, this does not give as much insight into the nature of the adsorption on the surface away from the droplet, i.e. in the precursor film. The method of calculating a local adsorption, used in Fig. 4.10, clearly allows for better comparison with the IH model and accurately fits the height of the droplet compared to the IH output. For droplets with a contact angle of $\theta > 90^\circ$ the local adsorption becomes somewhat misleading and the contour method is a much more meaningful measure of the droplet profile. In such a case only the density contour can accurately describe the droplet, since the adsorption method can not describe the multivalued nature of the droplet profile.

The contact angles from the two models can be directly compared. A contact angle is found using the DFT results by calculating the three interfacial surface tensions and then applying Young's equation, Eq. (1.1). A contact angle is extracted from the IH model results by fitting a circle to the apex of the droplet and finding the contact angle of this circle. Excellent agreement between the two methods is found as shown in Fig. 4.12. Note that only the DFT results are able to extend far beyond $\theta = 90^\circ$. Note too that these

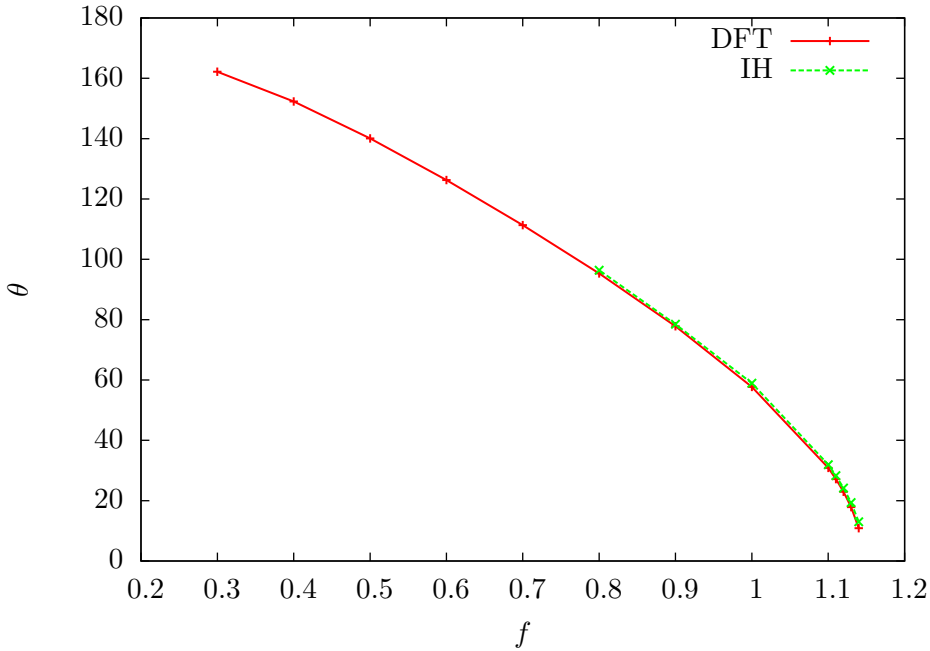


Figure 4.12: A comparison between contact angles, θ , found using DFT together with Young’s equation and with those found from the IH model with a binding potential calculated from DFT as input. These results are for varying wall attractive strength f and for fixed $\beta\epsilon = 1.1$.

results are for the macroscopic contact angle which is only attained by larger droplets. Indeed the comparison is not even made directly between the DFT droplet and the IH droplet profiles. Instead, the DFT contact angle is found from Young’s equation and does not require calculating a droplet profile. However, regardless of whether or not this macroscopic contact angle is a good approximation of the true contact angle of the droplets, a direct comparison of the droplet profiles obtained from the two models agree down to very small volumes, as shown in Fig. 4.13. As the volume of a droplet increases the contact angle obtained from the profile approaches the macroscopic contact angle. The coloured lines in Fig. 4.13 show the results from the DFT, the black lines are the IH droplet profiles. Good agreement is found for all droplet volumes, but getting slightly worse for very small droplets. It is possible to find solutions to the IH model that are droplets with a macroscopic contact angle slightly beyond $\theta = 90^\circ$. However, for such a case, the agreement with the DFT is not good and fitting the droplet with a circle is a very bad approximation of the film height profile, even though it accurately predicts the macroscopic contact angle. This poor fit stems from the inability of the film height profile to display the multivalued character of the droplet profile.

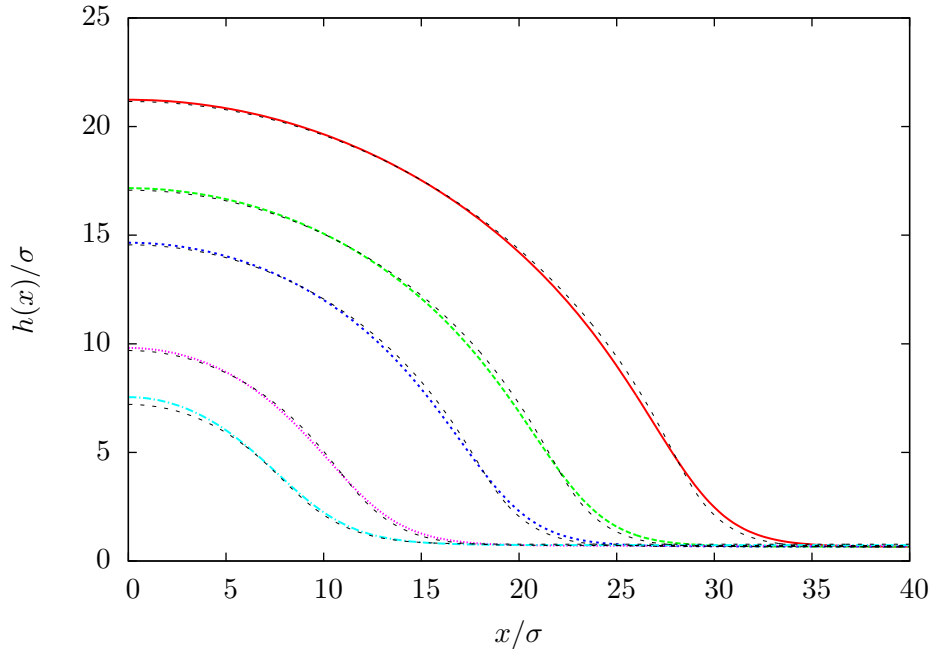


Figure 4.13: A droplet with a macroscopic contact angle of $\theta = 87^\circ$ at various volumes. Good agreement is found between the DFT and IH results down to very small droplet sizes. The agreement gets slightly worse for very small droplet sizes. These droplets are for $\beta\epsilon = 1.1$ and $f = 0.8$.

4.2 A Model Fluid with Oscillatory Binding Potentials

In the work above for the LJ fluid all of the binding potentials displayed have a monotonic decay. One can observe oscillatory binding potentials, but these occur for states where the liquid phase wetting the wall is metastable with respect to the solid. The occurrence of oscillatory binding potentials is connected to the location in the phase diagram of the so-called Fisher Widom (FW) line [56]. This line denotes the locus in the phase diagram at which the asymptotic decay of the correlations crosses over from monotonic to damped oscillatory. This form of decay can be seen in both the radial distribution function of the bulk fluid $g(r)$ ¹ and also in the inhomogeneous fluid density profiles. In colloid-polymer mixtures the location of the FW line is closely related to the size ratio $q = \sigma_p/\sigma$ of the polymer diameter, σ_p to the colloid diameter, σ . Moreover, in colloid-polymer mixtures one finds the FW line is located well away from freezing which means that in such systems one can observe oscillatory liquid-gas interfacial profiles and multiple layering transitions [47, 60]. Note that in the colloid-polymer context the “liquid” is a colloid rich phase and the “gas” is a colloid poor phase. The layering transitions observed in the Asakura-Oosawa (AO) model of colloid-polymer mixtures is

¹The radial distribution function is given by the Ornstein-Zernike equation. Monotonic or damped oscillatory decay is determined by the smallest complex pole in the integrand, i.e. the complex solutions of $1 - \rho_b \hat{c}(k) = 0$ where $\hat{c}(k)$ is the Fourier transform of $c^{(2)}(r)$. Find further details in Refs. [57] and [14].

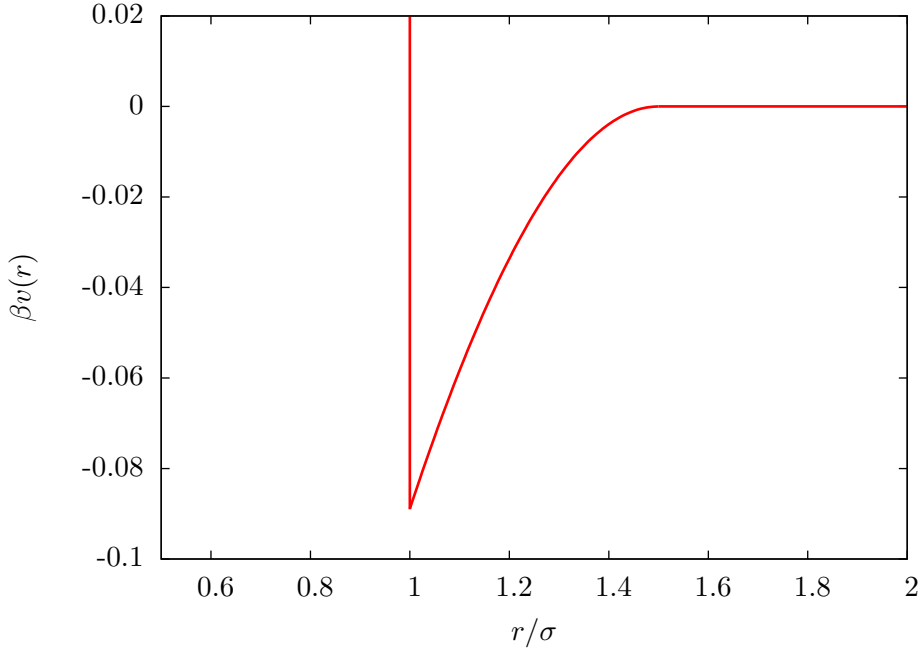


Figure 4.14: The potential $v = v_{hc} + v_{ao}$ where v_{ao} is the AO potential parametrised by $\beta\epsilon = 0.64$ and $q = 0.5$. The hard core repulsion is given by v_{hc} .

indicative that the binding potential for this system is oscillatory, since each new ‘‘layer’’ corresponds to a different minimum in $g(\Gamma)$. Indeed, the presence of layering transitions in any system is indicative of oscillatory binding potentials. In this section results are presented for a fluid of particles interacting via the AO potential:

$$v_{AO}(r) = -\epsilon \left(1 - \frac{3r}{2\sigma(1+q)} + \frac{r^3}{2\sigma^3(1+q)^3} \right) \text{ for } \sigma \leq r \leq \sigma(1+q), \quad (4.15)$$

and $v_{AO} = 0$ otherwise. The depth of the attractive well is governed by the parameter

$$\epsilon = \frac{1}{6}\pi\sigma_p^3 z_p \left(\frac{1+q}{q} \right)^3, \quad (4.16)$$

where z_p is the polymer fugacity. In this thesis the value of ϵ is simply quoted, the fugacity could be found from this if desired. The origin of this attractive potential arises from an entropic gain when colloids are close together. Around each colloid is a region of excluded volume stemming from the hard-core interactions of the colloids and polymers. As two colloids approach, the net excluded volume decreases, increasing the accessible volume within the system and leading to a rise in entropy [61]. The size ratio of the colloids to the polymers, q , defines the range of interaction for the potential, $R = (1+q)\sigma$. A plot of this potential is displayed in Fig. 4.14.

4.2.1 Density Profiles with Oscillations at the Liquid-Gas Interface

Whatever the interaction potential between the fluid particles, there is normally some oscillatory structure at a wall-liquid interface (see for example, the curve for $f = 1.5$ in Fig. 4.2), although the ultimate (asymptotic) decay of the density profile into the bulk liquid can be either monotonic or oscillatory, depending on which side of the FW line the bulk state lies. The decay from the liquid phase to the gas phase at the liquid-gas interface is almost always monotonic (see Fig. 4.3b). However, for smaller values of q and large values of the interaction strength, ϵ (equivalently low temperature), oscillations can be found on the liquid side of the liquid-gas interface, as seen in Fig. 4.15. The inset of the figure shows a zoom of part of the liquid-gas interface where oscillations are observed. The amplitude of these oscillations increases as ϵ increases. The interaction of the fluid particles with the container wall is also assumed to be via the AO potential, Eq. (4.15), where, as with the external potential used previously, the net interaction of a single fluid particle with the entire wall is found by integrating the interaction of a single fluid particle over a uniform density wall. The parameter governing the strength of this external field is ϵ_w .

The oscillations occur as a result of competition between the attractive and repulsive components of the interactions [23], where the repulsion originates from the hard core interactions of the reference fluid. The position of the state point on the bulk fluid phase diagram depends on both the size ratio, q (i.e. the interaction range), and the depth of the potential well ϵ . It is illustrated in Fig. 4.16 that it is the range of the pair potential that is the more important parameter in determining the onset of oscillations in the binding potential. The two curves in Fig. 4.16 are both at the same state point in the phase diagram, since the integrated strength of the pair potential in Eq. (4.15) for each of the two sets of parameter values gives the same result for each fluid. Only the binding potential for the fluid with the shorter ranged interaction ($q = 0.5$), but the deeper potential well, exhibits oscillations. The binding potential for the fluid with longer ranged interactions ($q = 1.0$) decays monotonically as $\Gamma \rightarrow \infty$. The location on the bulk fluid phase diagram of the FW line is not uniquely determined. It is the shape and depth of the potential well, ϵ , rather than the total integrated interaction strength (which determines the position on the phase diagram), that is important.

4.2.2 Oscillatory Binding Potentials and Highly Structured Droplets

Oscillatory density profiles lead to the occurrence of oscillatory binding potentials. For each interface in the density profile there is a decaying envelope of oscillations to the bulk density. For a wall-liquid and liquid-gas interface that are well separated, the oscillations from each interface decay to the bulk value and the two interfaces do not interact. As the two interfaces approach each other the envelopes of the oscillations from each interface overlap. In effect, the liquid-gas interface constrains the shape of the

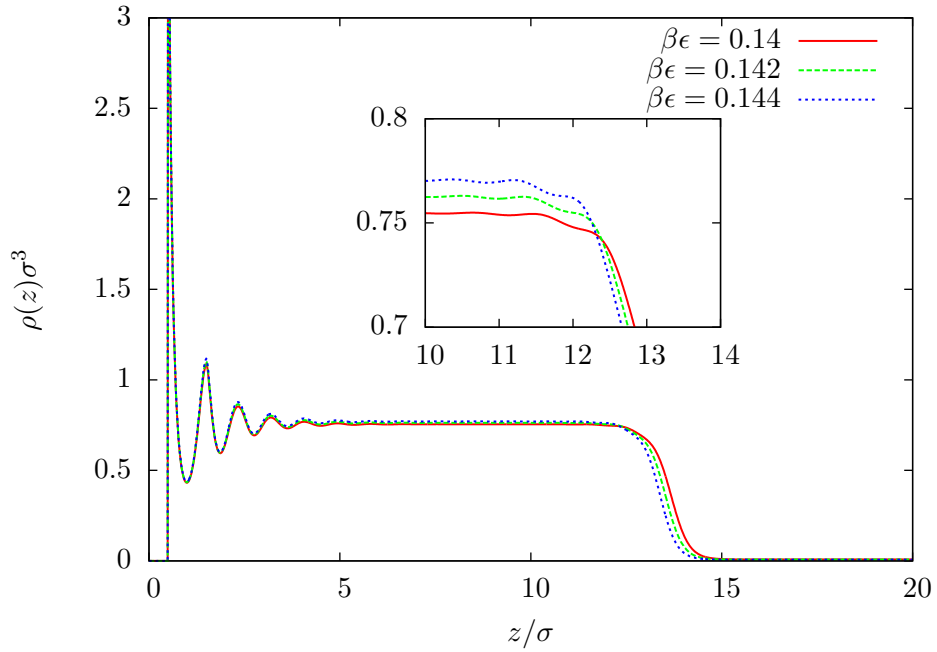


Figure 4.15: Constrained density profiles for the AO fluid for state points below the FW line. Strong oscillations occur at the wall-liquid interface and weaker oscillations occur at the liquid-gas interface. The amplitude of the oscillations increases with increasing ϵ or decreasing temperature. The external field is constant with attraction strength $\beta\epsilon_w = 0.7$ and the size ratio parameter which determines the range of interactions is $q = 0.5$.

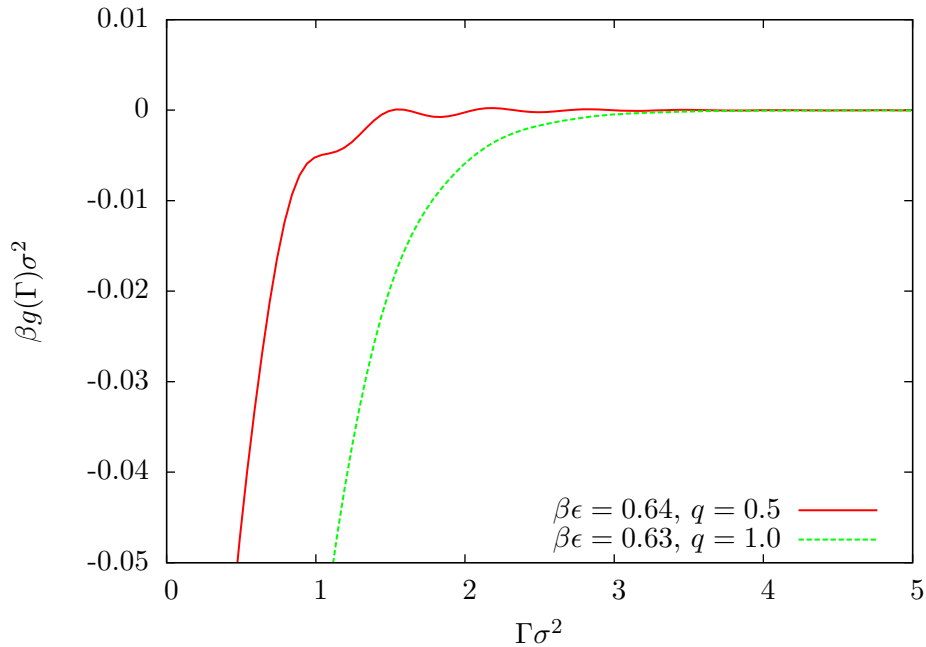


Figure 4.16: As the range of the interactions $R = (1 + q)\sigma$ is decreased, oscillations appear in the binding potential. These two states are at the same point on the bulk fluid phase diagram.

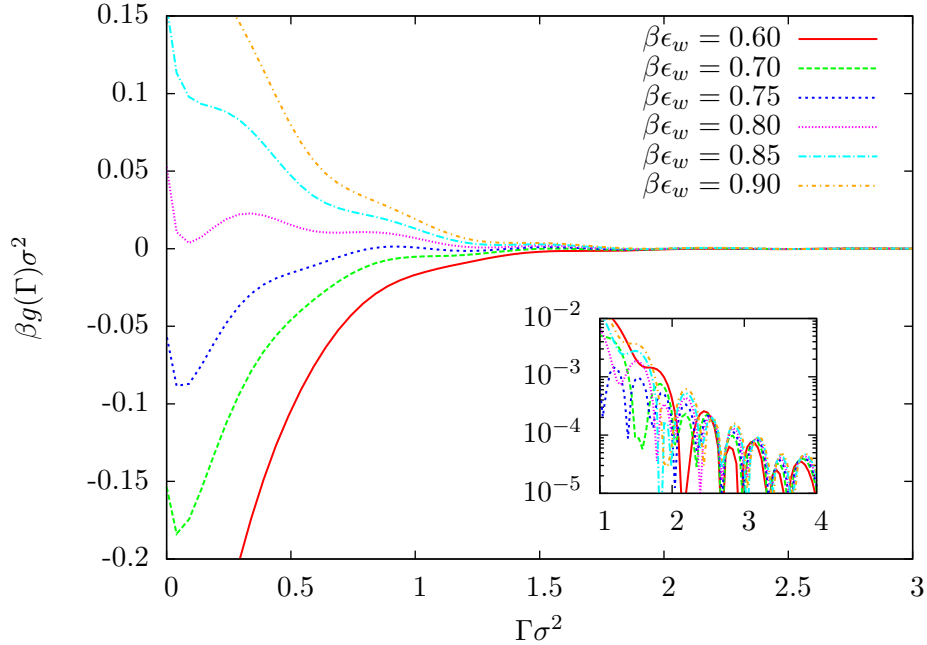


Figure 4.17: Binding potentials for the AO fluid with $\beta\epsilon = 0.64$ and $q = 0.5$. Oscillations occur in the tails of the binding potentials as a result of the oscillatory structure of the density profiles. The oscillatory structure from the wall-liquid interface can not smoothly transition into the oscillations of the liquid-gas interface at all film heights. The inset shows $|\beta g(\Gamma)|$ which highlights the oscillatory decay as $\Gamma \rightarrow \infty$.

density oscillations from the wall-liquid interface and similarly, the wall-liquid interface constrains the liquid-gas interface. Any constraint must raise the free energy of the system. Some configurations, determined by the film thickness (or Γ), raise the energy more than others because the oscillations from one interface can not smoothly transition into the oscillations of the other. This causes oscillations in the free energy of the system and can be seen in the binding potentials plotted in Fig. 4.17. Note that these oscillations decay with increasing Γ whereas the erroneous oscillations that occurred in the discrete DFT model had a constant amplitude as they were determined by the lattice spacing.

The presence of these oscillations means that the previously proposed fit function, Eq. (3.51), is no longer appropriate. The fit function proposed for these oscillatory binding potentials is

$$g_f(h) = a_3 \cos(a_1 h + a_2) \exp(-h/a_0) + a_4 \exp(-h/a_0) + a_5 \exp(-2h/a_0) + \dots, \quad (4.17)$$

where a_0, a_1, \dots are parameters to be fitted. The first term in this fit function accounts for the oscillatory behaviour and the remaining terms are inspired by the asymptotic form given in Eq. (1.3). The form of Eq. (1.3) arises when all of the particle interactions are short ranged. This fit function gives an excellent representation of the calculation results as can be seen in Fig. 4.18. Using this fit function as an input to the IH model,

droplet profiles such as those shown in Fig. 4.18 are obtained. The figure shows three droplets of increasing volume. The droplets are very low and long with a step like structure in the contact region. The binding potential used to generate this droplet is also shown in the figure. It is given here as a function of the film height $h \approx \Gamma/(\rho_l - \rho_g)$ and the minima correspond to the observed steps in the droplet profiles.

The droplet profiles can also be found directly using DFT as shown in Fig. 4.19, although, of course, the DFT gives a much more detailed description of the structure on the surface. This figure shows two different droplet profiles (a) and (c), both droplets show a lot more structuring than the regular droplets observed near the wetting transition when it is above the FW line (Fig. 4.4). In particular, in the contact region a terrace-like structure is found. This is most clearly observed in the $\rho\sigma^3 = 0.375$ contour displayed in Fig. 4.19b. Above this stepped region the droplet takes on the form of a spherical cap. On approaching the wetting transition the droplet spreads out a lot more, becoming very wide and flat as shown in Fig. 4.19c. Here there is no spherical cap component to the droplet and instead it is very flat, dominated by the local minima of the oscillations of the binding potential. Each minimum corresponds to having an additional layer of particles at the wall. The global minimum in $g(h)$, displayed in Fig. 4.18, is at $h \approx 0.1\sigma$, which corresponds to a low, sub-monolayer, number of particles absorbed on the wall. This can also be seen from the density profiles outside the droplets in Fig. 4.19. For an increased film thickness, there is a local minimum in $g(h)$ in Fig. 4.18, at $h \approx \sigma$, corresponding to an almost complete monolayer adsorbed on the wall. However, the free energy for this configuration is much higher than for the two minima either side, corresponding to a near empty surface ($h \approx 0.1\sigma$) or two adsorbed layers ($h \approx 1.7\sigma$). The minimum in $g(h)$ at $h \approx 2.5\sigma$, corresponding to three layers of particles, is an even lower free energy state. The fact that two or three almost complete layers is a lower energy state than a single layer is reflected in the density profiles in Fig. 4.19, where a single layer of particles adsorbed at the wall can not be observed. Finally, Fig. 4.19d shows an intermediary, non-equilibrium, density profile found during the minimisation to the droplet shown in (c), the initial condition was a half circle of the liquid density surrounded by the gas. It must be stressed that this minimisation procedure is not representative of the true spreading dynamics of the system. However, intermediary forms such as that in (d) suggest that there may be very interesting dynamics as these droplets evolve towards equilibrium. It should be mentioned however, that in some other systems [62] the fictitious dynamics generated by the Picard iteration is actually very similar to the true dynamics from DDFT. This thesis does not make any dynamical study but it would be an interesting avenue of research in the future.

The droplet profiles observed in Figs. 4.18 and 4.19 are remarkably similar to droplet profiles observed in the experiments reported in Ref. [63]. See also the discussions in Refs. [1, 64]. These experiments were for PDMS on a silicon wafer surface and terraced droplet profiles were observed, pointing to an underlying oscillatory binding potential.

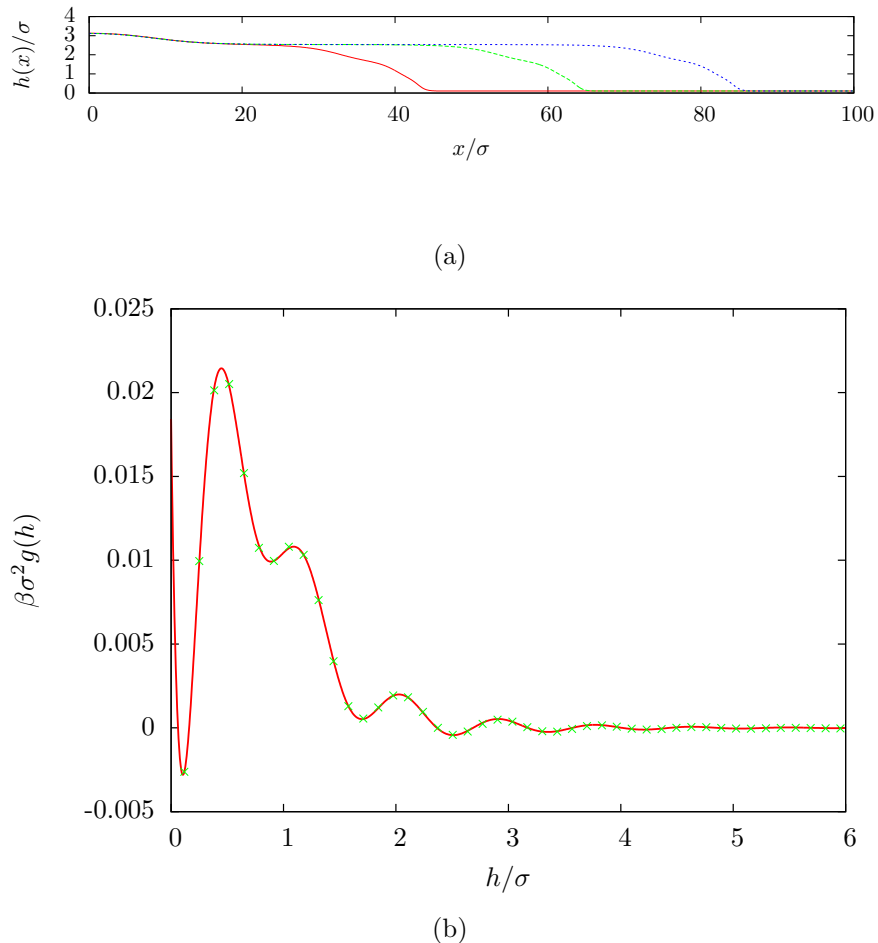


Figure 4.18: Film height profiles calculated from the IH model where oscillatory binding potentials are used as input. The droplet forms distinct layers and spreads out as the volume is increased with no increase in the maximum height. These results are for the AO fluid with $\beta\epsilon = 0.65$ and $\beta\epsilon_w = 0.81$. The parameters to fit this binding potential to Eq. (4.17) are: $a_0 = 0.908$, $a_1 = -7.352$, $a_2 = 5.901$, $a_3 = -0.011$, $a_4 = -0.00015$, $a_5 = 0.045$, $a_6 = 0.423$, $a_7 = -0.77$, $a_8 = -0.231$, $a_9 = 0.559$. The symbols show the fit with the data directly from the DFT calculation.

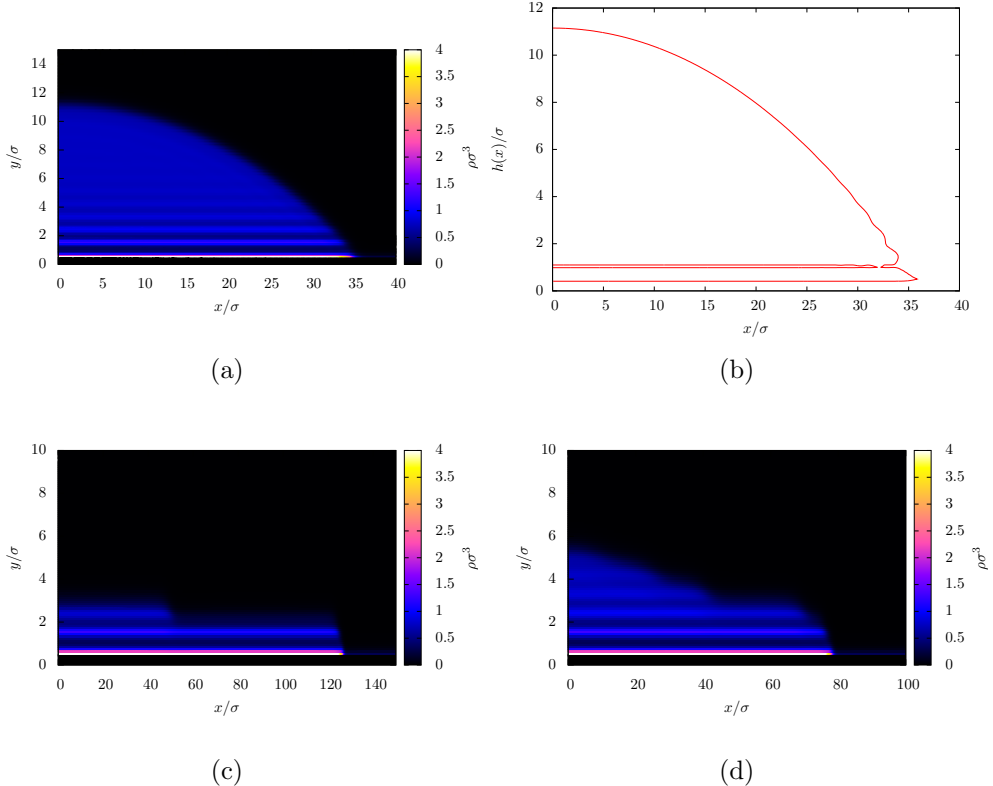


Figure 4.19: Two droplet density profiles, (a) and (c), for state points below the FW line. A lot of structure is observed in the drops, particularly in the contact region which is more clearly seen from the $\rho\sigma^3 = 0.375$ contour (b). An intermediary state (d) suggests the possibility of some interesting dynamics.

Layered droplets have also been observed in atomistic MD simulations of small droplets on surfaces [65].

4.3 Conclusions

This chapter investigated the calculation of binding potentials using continuum DFT. The specific model implemented took a hard sphere fluid as a reference state and treated the pairwise attractive interactions between fluid particles as a perturbation about the hard sphere fluid. The hard sphere fluid is modelled by the accurate White Bear version of FMT. Initially, the pair interactions are modelled by a truncated and shifted Lennard-Jones potential. This model was compared with numerical studies in Table 4.1 where it performed favourably. Density profiles varying in both one and two dimensions are displayed where more of the details of the structure of the density profile are described than in the discrete DFT. This is still a mean field model however so some interfacial fluctuation effects that may be present are not captured with DFT. By using an adsorption constraint, the binding potentials are calculated for the continuum fluid and these

are used to demonstrate that truncating fluid-fluid pair interactions can have profound effects on the predicted wetting behaviour. Specifically, it was shown that, for a certain choice of parameters, changing the truncation range from $r_c = 5\sigma$ to $r_c = 10\sigma$, leads to a shift in phase behaviour, from wetting to non-wetting as the truncation range is increased. This change in phase behaviour occurs far beyond the usual truncation range of $r_c = 2.5\sigma$ that is used in computer simulations.

The calculated binding potentials are fitted to an algebraic form and then used as input in the IH model to generate droplet profiles. These droplet profiles can then be compared to droplet profiles that are calculated directly using DFT by first generating a 2D droplet density profile and then integrating over this to obtain the film height profile. Excellent agreement is found between the two methods when comparing the droplet profiles. This good agreement also extends down to small droplet volumes. A comparison of macroscopic contact angles from each model is also made where, again, excellent agreement is found for all contact angles $0^\circ < \theta < 90^\circ$. Only the DFT model is able to find droplet profiles for $\theta > 90^\circ$. The good overall agreement validates the coarse-graining approach demonstrated throughout this thesis; using DFT to obtain accurate approximations for the binding potential $g(\Gamma)$ and then inputting this in the IH model, Eq. (1.2).

The Asakura-Oosawa (AO) model pair potential is considered as a typical model fluid having a short ranged pair interaction potential. Such potentials arise as the effective interaction potentials between colloids in suspension, say. For this short ranged potential, at lower effective temperatures (higher ϵ), density profiles with oscillatory decay are observed. These occur when the bulk fluid state is to the right of the FW line in the phase diagram. At such state points, there can also be oscillations in the density profile of the liquid-gas interface. In this regime, the oscillations that occur at the wall-liquid interface also have a large amplitude. These oscillatory density profiles give rise to oscillations in the tails of the binding potentials. By fitting the new algebraic form in Eq. (4.17), suitable for short ranged interactions, to these binding potentials, droplet height profiles can be found from the IH model. These droplet profiles which occur close to the wetting transition have a very pronounced terraced structure, are very thin and lose their spherical cap shape. Such droplet profiles can also be found directly using the DFT model in two dimensions which show the same stepped structure. A spherical cap is still found for larger droplets but there remains a high degree of structuring at the contact regions for these cases. Intermediary density profiles found during the minimisation procedure suggest some interesting dynamics that would be worth further study with DDFT or by performing time simulations with the thin-film equation.

Chapter 5

Final Remarks

This thesis has presented a method for calculating the binding potential for a fluid that is valid for all film thicknesses. The binding potential, or the related disjoining pressure, is important not just because of the physical properties of the fluid that they reveal, but because they act as inputs into mathematical models to study liquids at larger, mesoscopic scales. Despite the importance of the binding potential it is often only represented by an asymptotic form that can not accurately describe the shape of the binding potential for liquid films of very small film thicknesses. This thesis addresses this problem by presenting a method that can be used to calculate the binding potential which takes into account the microscopic particle interactions.

The calculation is performed with density functional theory (DFT), together with a method of finding the constrained equilibrium density profile for a liquid film of any given thickness. The local film thickness is related to the adsorption and so a liquid film of a particular thickness is fixed by constraining the adsorption of the system. The method of fixing the adsorption effectively forces an additional fictitious external field on the system which decays to zero beyond the desired film thickness. Not only does this method fix the adsorption to a particular value, but it also ensures that the system phase separates into a liquid and gas phase even for average densities that lie outside of the spinodal curve. A series of points of a binding potential are found through this method and these are then fitted to an algebraic form so that they may be used in the larger scale models. A particular form of the fit function is proposed here that exhibits the observed behaviour of the binding potentials.

In order to give some verification of this method, droplet profiles are calculated from two different models and compared. The first model is the mesoscopic interface Hamiltonian (IH) model which takes the binding potential as input. The binding potential used as input is calculated using the above, DFT based, method. The second model calculates a droplet profile using DFT two dimensions, constraining the total number of particles in the system to be equal to some specified value. This DFT model takes as input the same microscopic parameters that are used to calculate the binding potential which is

the input for the first model. Remarkably good agreement was observed between the two models.

In order to illustrate the approach this method was applied using a simple DFT, the discrete lattice-gas (LG) model. The droplet profiles calculated directly from the LG model fit excellently with the droplet profiles from the IH model across a wide range of contact angles. Good agreement was also found in the comparison of the contact angles calculated from each method. However, one weakness of this model is due to the presence of oscillations that occur in the tails of the binding potentials as a result of the discrete nature of the model. The origin of this is that it is not possible to have a liquid film at any possible film thickness and still maintain the equilibrium shape of the liquid-gas interface and the correct bulk liquid density. The free energy of the liquid film oscillates as a result.

A continuum DFT model is formulated by using the White Bear version of fundamental measure theory (FMT) to calculate a hard-sphere reference fluid and then adding a truncated and shifted Lennard-Jones (LJ) potential as a perturbation. By using this continuum model the oscillations in the tails of the binding potentials are eliminated. The particles in the continuum model are not restricted to specific grid points and so the thickness of the film can smoothly increase while maintaining the equilibrium shape of the liquid-gas interface. Comparisons between the droplet profiles found from this continuum DFT and the IH model are in excellent agreement across the whole range of accessible contact angles. The comparison of the contact angles themselves is also very good. The contact angles which are calculated from these models are the macroscopic contact angles. There is good agreement between these contact angles from the two models but they are not always a true representation of the actual contact angle that might be estimated from the droplet profile itself when the droplets have a small volume.

Systems interacting via a short ranged pair potential, the Asakura-Oosawa (AO) potential, were also investigated. This model potential is more applicable to colloidal suspensions than atomistic systems. For this system the density profiles that are highly oscillatory and this in turn leads to binding potentials with oscillatory decaying tails. This oscillatory form also manifests itself in the 2D droplet profiles which show highly structured liquid droplets. Results from both the DFT and the IH model for a state near the wetting transition both predict very flat terraced droplets that also hint at interesting dynamical behaviour.

As well as its use as an input to larger scale models, the binding potential also gives important information about the wetting behaviour of the fluid. The location of the global minimum indicates if the fluid wets a substrate or not and the value of the binding potential at this minimum can be used to calculate the contact angle of a liquid droplet. From this a study into the effects of truncating particle interactions was made. Interactions between fluid particles are often truncated in computer simulations in order to speed up calculations. This is purely a choice made in the modelling of

the fluid and does not represent the real physics of the system. The binding potentials calculated in this Thesis show that truncating the particle interactions can result in the true phase behaviour of the system to sometimes be lost. Truncating the fluid-fluid particle interactions to shorter ranges leads to a model fluid that is more wetting and this can sometimes occur to the extent that a non-wetting fluid appears to be a wetting fluid purely because the interactions have been truncated. It is hoped that the fully microscopic binding potential calculated in this Thesis will prove to be of use in future studies of droplets spreading and other such fluid interfacial phenomena. To this end, tables of parametrised binding potentials are included in Appendix B.

Appendix A

A Simpler Lattice Pair Interaction

In §3.3 a simpler pair potential was mentioned that only extended to next-nearest neighbour lattice sites. This is the same potential that was used in Ref. [18] and is now defined here. This potential was defined for a 2D system although it can be reduced down to an effective 1D system if desired. The ‘nearest neighbour’ lattice sites to a particular site are defined as those lattice sites either horizontally or vertically adjacent to it. The ‘next nearest neighbours’ are those lattice sites which are diagonally adjacent, this is illustrated in Fig. A.1. The nearest neighbour lattice sites interact more strongly than the next nearest neighbours where there is some freedom to choose the extent to which the next nearest neighbour interactions are weaker than the nearest neighbour interactions. The pair potential described in Eq. (3.31) would give that for a nearest neighbour interaction of strength ϵ , the next nearest neighbour interactions would have a strength of $\epsilon/8$. In his PhD thesis Robbins showed that the taking interaction weights of ϵ and $\epsilon/4$ for the nearest and next nearest interactions is the optimum choice to find circular droplets. These interaction weights are given in Fig. A.2 for both the 2D system and the equivalent 1D reduction.

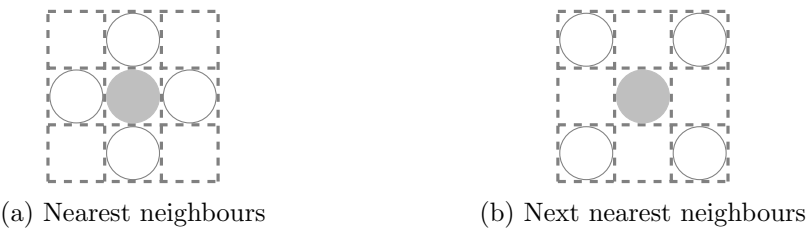


Figure A.1: The nearest and next nearest neighbour lattice sites.



Figure A.2: (a) The optimal interaction weights to give circular droplets with this short ranged potential. (b) The reduction of this potential for an effective 1D system.

Using this potential the lattice free energy becomes

$$\begin{aligned} \hat{\Omega} = k_B T \sum_{\mathbf{i}=1}^M & [\rho_{\mathbf{i}} \ln \rho_{\mathbf{i}} + (1 - \rho_{\mathbf{i}}) \ln(1 - \rho_{\mathbf{i}})] \\ & - \frac{1}{2} \sum_{\mathbf{jnni}} \epsilon \rho_{\mathbf{i}} \rho_{\mathbf{j}} - \frac{1}{2} \sum_{\mathbf{jnnni}} \frac{\epsilon}{4} \rho_{\mathbf{i}} \rho_{\mathbf{j}} + \sum_{\mathbf{i}=1}^M (V_{\mathbf{i}} - \mu) \rho_{\mathbf{i}}, \end{aligned} \quad (\text{A.1})$$

where the summation index \mathbf{jnni} indicates the sum over all lattice sites \mathbf{j} which are the nearest neighbours of \mathbf{i} , and similarly \mathbf{jnnni} denotes the sum over the next nearest neighbours.

Appendix B

Parameters for the binding potential fit functions

This appendix lists the parameter values used to fit the binding potential to an algebraic form for many of the results presented in this Thesis. For monotonically decaying binding potentials the fit function is

$$g(\Gamma) = \frac{A(\exp(-P(\Gamma)) - 1)}{\Gamma^2}, \quad (\text{B.1})$$

where

$$P(\Gamma) = a_0 e^{-a_1 \Gamma^2} + a_2 \Gamma^2 + a_3 \Gamma^3 + a_4 \Gamma^4 + a_5 \Gamma^5. \quad (\text{B.2})$$

The parameters associated with a selection of binding potentials calculated from the discrete LG model are given in Table B.1 and the parameters for the continuum DFT are given in Table B.2.

Figure	$\beta\epsilon$	$\beta\epsilon_w$	L	A	a_0	a_1	a_2	a_3	a_4	a_5
3.7 & 3.14	0.9	0.5	5	-0.073	1.313	8	-3.072	3.253	-1.248	0.168
3.7 & 3.14	0.9	0.55	5	-0.081	1.199	8	-2.205	2.173	-0.762	0.094
3.7 & 3.14	0.9	0.6	5	-0.088	1.100	8	-1.443	1.291	-0.393	0.042
3.7 & 3.14	0.9	0.65	5	-0.095	1.014	8	-0.786	0.609	-0.139	0.011
3.7	0.9	0.7	5	-0.123	0.809	8	-0.203	0.128	-0.010	0.0002
3.12	0.8	0.5	3	-0.057	0.920	8	-0.699	0.437	-0.072	0.004
3.12	0.8	0.5	4	-0.057	0.922	8	-0.920	0.599	-0.123	0.009
3.12	0.8	0.5	5	-0.057	0.924	8	-1.063	0.707	-0.158	0.012
3.12	0.8	0.5	10	-0.056	0.944	8	-1.285	0.863	-0.204	0.017
3.12	0.8	0.5	20	-0.036	1.520	8	-1.985	1.464	-0.389	0.036

Table B.1: This table lists the parameters used in the fitting function to fit the binding potentials, calculated from the LG model, to an algebraic form. The parameters are identified by the figure in which the binding potential is used, the title of that curve in the figure and some additional identification where applicable. Values are rounded to three decimal places and the value of a_1 is enforced.

Figure	$\beta\epsilon$	f	r_c	A	a_0	a_1	a_2	a_3	a_4	a_5
4.10	1.1	0.8	5	-0.310	0.147	3.621	-0.378	0.174	-0.028	0.002
4.10	1.1	0.85	5	-0.336	0.151	3.237	-0.302	0.139	-0.021	0.001
4.10	1.1	0.9	5	-0.362	0.155	2.962	-0.233	0.109	-0.016	0.0008
4.10	1.1	0.95	5	-0.388	0.158	2.774	-0.168	0.081	-0.012	0.0006
4.10	1.1	1.01	5	-0.420	0.160	2.663	-0.093	0.051	-0.007	0.0004
4.10	1.1	1.02	5	-0.426	0.160	2.658	-0.081	0.043	-0.006	0.0003
4.10	1.1	1.04	5	-0.437	0.160	2.659	-0.056	0.036	-0.005	0.0002

Table B.2: This table gives the parameters from fitting the binding potentials calculated using the continuum DFT to an algebraic form for a selection of the results shown in Chapter 4.

Bibliography

- [1] P. G. de Gennes. Wetting: statics and dynamics. *Rev. Mod. Phys.*, 57(3):827 – 863, 1985.
- [2] D. Bonn, J. Eggers, J. Indekeu, J. Meunier, and E. Rolley. Wetting and spreading. *Reviews of Modern Physics*, 81:739, 2009.
- [3] A. Marchand, J. H. Weijs, J. H. Snoeijer, and B. Andreotti. Why is surface tension a force parallel to the interface. *Am. J. Phys.*, 79:999, 2011.
- [4] M. Schick. An introduction to wetting phenomena. In *Liquids at Interfaces, Proceedings of the Les Houches 1988 Session XLVIII*. Elsevier, 1988.
- [5] S. Dietrich. Wetting phenomena. In C. Domb and J.L. Lebowitz, editors, *Phase Transitions and Critical Phenomena*, volume 12. 1988.
- [6] L.G. MacDowell, J. Benet, N.A. Katcho, and J.M.G. Palanco. Disjoining pressure and the film-height-dependent surface tension of thin liquid films: New insight from capillary wave fluctuations. *Adv. Colloid Interface Sci.*, 206:150–171, 2014.
- [7] J. R. Henderson. Statistical mechanics of the disjoining pressure of a planar film. *Phys. Rev. E*, 23:051602, 2005.
- [8] B. V. Derjaguin. Modern state of the investigation of long-range surface forces. *Langmuir*, 3(5):601 – 696, 1987.
- [9] B. V. Derjaguin and N. Churaev. The current state of the theory of long-range surface forces. *Progress in Surface Science*, 40:272 – 285, 1992.
- [10] Uwe Thiele. Structure formation in thin liquid films. In S. Kalliadasis and Uwe Thiele, editors, *Thin films of soft matter*, pages 25–94. Springer Wien New York, 2007.
- [11] Alexander Oron, Stephen H. Davis, and S. George Bankoff. Long-scale evolution of thin liquid films. *Rev. Mod. Phys.*, 69(3):931 – 980, 1997.
- [12] U. Thiele. Thin film evolution equation from (evaporating) dewetting liquid layers to epitacial growth. *J. Phys.: Condens. Matter*, 22:084019, 2010.

- [13] J. N. Israelachvili. *Intermolecular and surface forces*. Waltham, MA : Academic Press, 2011.
- [14] J.-P. Hansen and I R McDonald. *Theory of Simple Liquids*. Elsevier, Warsaw, 4th edition, 2013.
- [15] V. A Parsegian. *Van der Waals forces: A handbook for biologists, chemists, engineers, and physicists*. Cambridge: Cambridge University Press, 2006.
- [16] L. MacDowell. Computer simulation of interface potentials: Towards a first principle description of complex interfaces? *Eur. Phys. J. Special Topics*, 197:131–145, 2011.
- [17] N. Tretyakov, M. Müller, D. Todorova, and U. Thiele. Parameter passing between molecular dynamics and continuum models for droplets on solid substrates: The static case. *Journal of Chemical Physics*, 138:064905, 2013.
- [18] A. P. Hughes, U. Thiele, and A. J. Archer. An introductino to inhomogeneous liquids, density functional theory, and the wetting transition. *Am. J. Phys.*, 82(12):1119, December 2014.
- [19] A. P. Hughes, A. J. Archer, and U. Thiele. Liquid drops on a surface: using density functional theory to calculate the binding potential and drop profiles and comparing with results from mesoscopic modelling. *J. Chem. Phys.*, 142:074702, 2015.
- [20] A. P. Hughes, U. Thiele, and A. J. Archer. The structure of liquid droplets. In preparation.
- [21] K. Stowe. *An Introduction to Thermodynamics and Statistical Mechanics*. Cambridge University Press, New York, 2nd edition, 2007.
- [22] R. Evans. The nature of the liquid-vapour interface and other topics in the statistical mechanics of non-uniform, classical fluids. *Advances in Physics*, 28(2):143–200, 1979.
- [23] R. Evans. Density functionals in the theory of nonuniform fluids. In D. Henderson, editor, *Fundamentals of Inhomogeneous Fluids*, chapter 3, pages 85–175. Taylor & Francis, 1992.
- [24] M. Le Bellac, F. Mortessagne, and Batrouni G. *Equilibrium and non-equilibrium statistical thermodynamics*. Cambridge University Press, New York, 2004.
- [25] N. M. Laurendeau. *Statistical thermodynamics: fundamentals and applications*. Cambridge University Press, New York, 2005.
- [26] T. K. Vanderlick, H. T. Davis, and J. K. Percus. The statistical mechanics of hard rod mixtures. *J. Chem. Phys.*, 91:7136, 1989.

- [27] P. Hohenberg and W. Kohn. Inhomogeneous electron gas. *Physical Review*, 136:B864, 1964.
- [28] C. Ebner, W. F. Saam, and D. Stroud. Density-functional theory of simple classical fluids I. Surfaces. *Physical Review A*, 14(6):2264, 1976.
- [29] S. Toxvaerd. Perturbation theory for nonuniform fluids: Surface tension. *J. Chem. Phys.*, 55:3116, 1971.
- [30] M. Johnson and S. Nordholm. Generalized van der Waals theory. VI. Application to adsorption. *J. Chem. Phys.*, 75:1953, 1981.
- [31] F. van Swol and J. Henderson. Wetting and drying transitions at a fluid-wall interface: Density-functional theory versus computer simulation. *Phys. Rev. A*, 40(5):2567, 1989.
- [32] Y. Rosenfeld. Free-energy model for the inhomogeneous hard-sphere fluid mixture and density-functional theory of freezing. *Phys. Rev. Lett.*, 63(9):980, 1989.
- [33] R. Roth, R. Evans, A. Lang, and G. Kahl. Fundamental measure theory for hard-sphere mixtures revisited: the White Bear version. *J. Phys.: Condens. Matter*, 14:12063–12078, 2002.
- [34] Roland Roth. Fundamental measure theory for hard-sphere mixtures: a review. *J. Phys.: Condens. Matter*, 22:063102, 2010.
- [35] P. Tarazona, J.A. Cuesta, and Y. Martínez-Ratón. Density functional theories of hard particle systems. In Ángel Mulero, editor, *Lect. Notes Phys.*, volume 753, chapter 7, pages 247–341. Springer Berlin Heidelberg, 2008.
- [36] E. Kierlik and M. L. Rosinberg. Free-energy density functional for the inhomogeneous hard-sphere fluid: Application to interfacial adsorption. *Phys. Rev. A*, 42(6):3382, 1990.
- [37] H. Hansen-Goos and R. Roth. Density functional theory for hard-sphere mixtures: the White Bear version mark II. *J. Phys.: Condens. Matter*, 18:8413 – 8425, 2006.
- [38] P. Tarazona. Density functional for hard sphere crystals: A fundamental measurere approach. *Phys. Rev. Lett.*, 84(4):694, 2000.
- [39] M Marechal and H. Löwen. Density functional theory for hard polyhedra. *Phys. Rev. Lett.*, 110:137801, 2013.
- [40] Y.-X. Yu and J. Wu. Density functional theory for inhomogeneous mixtures of polymeric fluids. *J. Chem. Phys.*, 117:2368, 2002.

- [41] Y. Rosenfeld, M. Schmidt, H. Löwen, and P. Tarazona. Dimensional crossover and the freezing transition in density functional theory. *J.Phys.: Condens. Matter*, 8:L577 – L581, 1996.
- [42] Y. Rosenfeld, M. Schmidt, H. Löwen, and P. Tarazona. Fundamental-measure free-energy density functional for hard spheres: Dimensional crossover and freezing. *Phys. Rev. E*, 55(4):4245, 1997.
- [43] A Malijevský and A. O. Parry. Critical point wedge filling. *Phys. Rev. Lett.*, 110:166101, 2014.
- [44] M. C. Stewart and Robert Evans. Wetting and drying at a curved substrate: Long ranged forces. *Phys. Rev. E*, 71:011602, 2005.
- [45] M. C. Stewart and Robert Evans. Critical drying at a spherical substrate. *J. Phys.: Condens. Matter*, 17:S3499, 2005.
- [46] J. R. Edison, N. Tasios, S. Belli, R. Evans, R. van Roij, and M. Dijkstra. Critical Casimir forces and colloidal phase transitions in a near-critical solvent: A simple model reveals a rich phase diagram. *Phys. Rev. Lett.*, 114:038301, 2015.
- [47] J. M. Brader, R. Evans, and M. Schmidt. Statistical mechanics of inhomogeneous model colloid-polymer mixtures. *Mol. Phys.*, 101(23–24):3349–3384, 2003.
- [48] A.J. Archer and R. Evans. Nucleation of liquid droplets in a fluid with competing interactions. *Mol. Phys.*, 109:2711–2722, 2011.
- [49] L. G. MacDowell and M. Müller. Adsorption of polymer on a brush: Tuning the order of the wetting phase transition. *J. Chem. Phys.*, 124:084907, 2006.
- [50] V. Kumar and J. R. Errington. Understanding the wetting of immiscible liquids near a solid surface using molecular simulation. *J. Chem. Phys.*, 139:064110, 2013.
- [51] V. M. Starov and M. G. Velarde. Surface forces and wetting phenomena. *J.Phys.: Condens. Matter*, 21:464121, 2009.
- [52] U. M. B. Marconi and P. Tarazona. Dynamical density functional theory of fluids. *J. Chem. Phys.*, 110(16):8032–8044, 1999.
- [53] U. M. B. Marconi and P. Tarazona. Dynamic density functional theory of fluids. *J. Phys.: Condens. Matter*, 12:A413–A418, 2000.
- [54] A.J. Archer and R. Evans. Dynamical density functional theory and its application to spinodal decomposition. *J. Chem. Phys.*, 121(9):4246–4254, 2004.

- [55] A.J. Archer and M. Rauscher. Dynamical density functional theory for interacting Brownian particles: stochastic or deterministic? *J. Phys. A.: Math. Gen.*, 37:9325–9333, 2004.
- [56] M. E. Fisher and B. Widom. Decay of correlations in linear systems. *J. Chem. Phys.*, 50(9):3756, May 1969.
- [57] R. Evans, J. R. Henderson, D. C. Hoyle, A. O. Parry, and Z. A. Sabeur. Asymptotic decay of liquid structure: oscillatory liquid-vapour density profiles and the Fisher-Widom line. *Mol. Phys.*, 80:755–775, 1993.
- [58] R. Evans, R. J. F. Leote de Carvalho, J. Henderson, and D. C. Hoyle. Asymptotic decay of correlations in liquids and their mixtures. *J. Chem. Phys.*, 100:594, 1994.
- [59] T. Ingebrigtsen and S. Toxvaerd. Contact angles of Lennard-Jones liquids and droplets on planar surfaces. *J. Phys. Chem. C*, 111:8518 – 8523, 2007.
- [60] M. Schmidt, H. Löwen, J. M. Brader, and R. Evans. Density functional theory for a model colloid-polymer mixture: bulk fluid phases. *J. Phys.: Condens. Matter*, 14:9353–9382, 2002.
- [61] S. Asakura and F. Oosawa. On interaction between two bodies immersed in a solution of macromolecules. *J. Chem. Phys.*, 22:1255, 1954.
- [62] A. J. Archer, A. M. Rucklidge, and E. Knobloch. Soft-core particles freezing to form a quasicrystal and a crystal-liquid phase. *Phys. Rev. E*, 92:012324, 2015.
- [63] F. Heslot, N. Fraysse, and A. M. Cazabat. Molecular layering in the spreading of wetting liquid drops. *Nature*, 338:640, 1989.
- [64] M. N. Popescu, G. Oshanin, S. Dietrich, and A. M. Cazabat. Precursor films in wetting phenomena. *J. Phys.: Condens. Matter*, 24:243102, 2012.
- [65] S. Bekink, S. Karaborni, G. Verbist, and K. Esselink. Simulating the spreading of a drop in the terraced wetting regime. *Phys. Rev. Lett.*, 76(20):3766, 1996.